Dissertation
submitted to the
Combined Faculties for the Natural Sciences and for Mathematics
of the Ruperto-Carola University of Heidelberg, Germany
for the degree of
Doctor of Natural Sciences

Put forward by:
M. Sc. Robert Felix Reischke
born in
Rostock

Oral examination: 18.04.2018

Cosmology as a probe of gravity with future surveys

Referees:
Prof. Dr. Björn Malte Schäfer
Prof. Dr. Luca Amendola

Cosmology as a probe of gravity with future surveys
The subject of this thesis are different aspects of cosmology as a probe of the underlying gravitational theory with future surveys.

In the first part of this work we discuss the parameter dependence of covariance matrices of the power spectrum estimator of the large-scale structure. Its variation across parameter space is calculated analytically by constructing a suitable basis and is then compared with numerical simulations. The method presented is applicable to any matrix-valued function which is everywhere positive-definite.

The second part investigates the influence of tidal gravitational fields on the formation of dark matter halos at peaks in the density field of the large-scale structure. We extend the spherical collapse model to incorporate the influence of shear and rotation by treating them as inhomogeneities in the non-linear evolution equation. We investigate the statistics of the tidal field and how it is inherited to the statistics of the critical over-density δ_c. It is shown that the collapse in a tidal field will always proceed faster than the collapse in a homogeneous background.

The last part investigates the combination of observations of weak gravitational lensing, galaxy clustering and the cosmic microwave background and the cross-correlations between the probes to investigate scalar-tensor theories of gravity. We carry out a Fisher analysis as well as a Monte-Carlo-Markov-chain to estimate the expected statistical errors. The analysis shows that gravitational theories can be constrained very well with future surveys.

Kosmologische Tests der Gravitationstheorie
Die hier vorliegende Arbeit beschäftigt sich mit verschiedenen Aspekten kosmologischer Tests von Gravitationstheorien mit zukünftigen Himmelsdurchmusterungen.

Im ersten Teil wird die Abhängigkeit der Kovarianzmatrix des Leistungsspektrumestimators der großskaligen Strukturen vom zugrundeliegenden kosmologischen Modells untersucht. Wir berechnen die Abhängigkeit mit analytischen Methoden für ausgewählte kosmologische Parameter und vergleichen die Resultate mit numerischen Simulationen. Die präsentierte Methode ist neben dem hier beschriebenen Fall auch auf jede positiv-definite matrix-wertige Funktion anwendbar.

Der zweite Teil beschäftigt sich mit der Entstehung von Dunkle Materie Halos an Dichte-Extrema in der großskaligen Struktur. Das sphärische Kollaps-Modell wird untersucht und die Effekte von Scherung und Rotation werden in die Dynamik mit einbezogen. Beide Effekte werden durch Inhomogenitäten in der nicht-linearen Entwicklungsgleichung beschrieben. Die Statistik des Gezeitenfeldes, welches durch die umgebenden Strukturen auf den entstehenden Halo wirkt, wird untersucht. Scherung und Rotation werden pertubativ aus der Statistik des Dichtefeldes abgeleitet und ihr Einfluss auf die kritische Überdichte, δ_c, untersucht. Wir konnten zusätzlich zeigen, dass ein Halo aus Dunkler Materie an einem Extremum im Dichtefeld immer schneller kollabiert als ein isolierten Halo in einem homogenen Dichtefeld.

Im letzten Teil dieser Arbeit beschäftige wir uns mit kombinierten Beobachtungen des schwachen Gravitationslinseneffektes, Galaxienkorrelationen und des kosmischen Mikrowellhintergrunds und wie sich damit die zugrunde liegende Gravitationstheorie einschränken lässt. Es wird eine Fisher Analyse durchgeführt, um die zu erwartenen statistischen Fehler abzuschätzen. Zusätzlich werden Monte-Carlo-Markov-Ketten berechnet um die Nichtgaussianitäten in dem hoch-dimensionalen Parameterraum besser darzustellen. Die Analyse zeigt, dass man Änderung in der Gravitationstheorie mit der Kombination von verschiedenen Observablen und insbesondere ihrer Kreuzkorrelation sehr gut einschränken kann.

CONTENTS

LIST OF FIGURES

LIST OF TABLES

ACRONYMS

CMB	Cosmic Microwave Background
SNIa	Type Ia Supernova
CDM	Cold Dark Matter
SPT	standard perturbation theory
DM	Dark Matter
KFT	kinetic field theory
LPT	Lagrangian perturbation theory
ZA	Zel'dovich approximation
LSS	large-scale structure
ΛCDM	cosmological standard model
MCMC	Monte-Carlo Markov chain
MLE	maximum likelihood estimator
BAO	baryonic acoustic oscillation
SW	Sachs-Wolfe
iSW	integrated Sachs-Wolfe
GR	General Relativity
EFT	effective field theory
FLRW	Friedmann-Lemaître-Robertson-Walker
SPC	spherical collapse
DE	Dark Energy
MG	Modified Gravity
LSST	Large Synoptic Survey Telescope
SKA	Square Kilometre Array
WFIRST	Wide-Field Infrared Survey Telescope
WMAP	Wilkinson Microwave Anisotropy Probe

PRELIMINARIES

NOTATION

Throughout this thesis we will use the following signature for the metric $(-,+,+,+)$, such that the Minkowski metric becomes

$$\boldsymbol{\eta} = \mathrm{diag}(-1,1,1,1)\ .$$

Furthermore we will write tensorial quantities in boldface, while its components are written normally, for example the metric tensor is

$$\mathbf{g}, \quad \text{with components} \quad g_{\mu\nu}\ .$$

If we consider vectors related to the space-time, e.g. the position vector $\mathbf{x}$, Greek indices run from zero to three while Latin run from one to three and label the position only, e.g.:

$$\mathbf{x}^T = (x_0, x_i)\ .$$

Other Latin indices may run over any number given.

UNITS

In this thesis we will usually use cgs-units and keep track all important constants. Only in Chapter 6 we will switch gears slightly when discussing the Lagrangian and use natural units. In cgs units the numerical values of constants of nature, units and parameters used here are:

$G = 6.67384 \times 10^{-8} \frac{cm^3}{s^2 g}$	Gravitational constant
$c = 29979245800\ \frac{cm}{s}$	Speed of light in vacuum
$1\ pc = 3.0857 \times 10^{18} cm$	One parsec
$1\ M_\odot \approx 2 \times 10^{33} g$	One solar mass
$\Omega_{m0} = 0.314$	dark and visible matter density parameter
$\sigma_8 = 0.834$	fluctuation amplitude
$H_0 = 2.184 \times 10^{-18} \frac{1}{s}$	Hubble constant
$\Omega_K \approx 0$	Spatial curvature parameter
$n_s = 0.962$	Slope of initial power spectrum

The values for the cosmological parameters are taken from the Planck Collaboration et al. (2016).

1 INTRODUCTION

Over the last century, cosmology has turned from a purely astronomical science into a discipline of modern physics and has developed physical models of our Universe that can be tested quantitatively. Hundred years ago we thought that the Milky Way itself makes up the entire Universe and it was not clear whether so-called *Nebulae* were actually part of our own Galaxy or not. Instead, the next generation of cosmological surveys, to be launched within the next decade, will deliver data of over a billion galaxies and will probe structures down to very small cosmological scales (e.g. Laureijs et al., 2011; LSST Dark Energy Science Collaboration, 2012; Maartens et al., 2015; Camera et al., 2015; Thornton et al., 2016). In fact, those experiments will probe a large fraction of the observable volume of our Universe.

The observational picture (see e.g. Weinberg et al., 2013, for a detailed review) of our Universe today is that it consists only to roughly 5% of ordinary matter (baryons) which is part of the standard model of particle physics. The rest of the matter consists of Dark Matter (DM), a species which does not interact with photons and is hence called dark matter. In particular one finds that the dark matter particles, which itself have not been detected yet, have a vanishing temperature or no internal energy due to their own random motion. Therefore this particular type of DM is usually called Cold Dark Matter (CDM). Even more mysterious is the accelerated expansion of our Universe which is confirmed by all observations. This leads to the conclusion that the energy budget of the Universe is made up of two thirds by an energy which may be due to the cosmological constant, Λ in Einstein's field equations. The standard model of cosmology, a statistically isotropic and homogeneous solution to the field equations of General Relativity (GR) with a cosmological constant, radiation, baryons and CDM, is hence called the cosmological standard model (ΛCDM).

This leaves us with a model which is as simple as possible but tells us that our Universe is basically made up of stuff we do not know thus implying a long list of questions. What is the nature of CDM, indirectly detected through rotation curves, gravitational lensing, and the Cosmic Microwave Background (CMB)? Can the early accelerated epoch of the Universe be better understood? What is the origin of the late-time accelerated expansion? Is it possibly due to the cosmological constant and if so why is the value of Λ so much different from the vacuum energy from quantum field theoretical estimates? For this last question one also needs to keep in mind our poor understanding of a quantum theory of gravity. Furthermore, there could be some unknown symmetry pushing the vacuum energy to the value we observe. Ultimately the accelerated expansion could also be due to some additional field which enters in the energy-momentum tensor in the field equations, a scenario which is called Dark Energy (DE). With DE at hand one should, however, also ask the question whether the theory of gravity we are using, namely GR, is correct? Even though it is tested on a lot of scales and different environments it has not been tested on cosmological scales so far.

As an astrophysical driven science, cosmology obviously suffers from the problem that we cannot repeat measurements with slightly different settings. It is therefore

not possible to design an experiment which only measures for example a few cosmological parameters. It is thus necessary to answer those questions simultaneously. Furthermore, there is a high degree of degeneracy between different questions or, equivalently, parameters. Hence one needs a lot of data to reduce statistical errors and to constrain for example the cosmological model together with the underlying theory of gravity. With future surveys a vast amount of exquisite data will be available with new CMB experiments, weak gravitational lensing surveys or intensity mapping. Given the data it is the task of statistical inference to find the model that best explains the data by maximum likelihood methods. This procedure requires sound theoretical predictions of the model and even though the theoretical predictions have been good enough for previous surveys, they are not necessarily accurate enough for the next generation. The last points are of particular importance since future surveys rely a lot on the observations of the evolved large-scale structure (LSS) to unrivalled scales, where non-linear effects due to late time structure formation become dominant.

Since there is a limit on the amount of cosmological data, the question arises how well future surveys will be able to constrain different models in general. Additionally one needs to find those observables, which are most sensitive on the parameters one is interested in. In cosmology there is typically a parameter hierarchy, which is again due to its astrophysical nature. There are very well known parameters, for example the matter density, which are basically set since e.g. the Planck Collaboration et al. (2016) in a way that the measured values are nearly as precise as the constant of nature they are related to, the Newton constant. Thus there is no gain in increasing the precision of these parameters way further. On the other hand there are parameter which are constrained only very purely, like the time variation of DE, MG parameters, or even parameters from particle physics such as the sum of the neutrino masses. In order to measure them precisely high signal strengths of cosmological measurements are needed which in turn can only be achieved when fully exploiting also cosmologically small scales.

From the arguments made so far it should be clear that it is necessary to revise the assumptions entering in the calculation of observables derived from the theoretical model. Non-linear structure formation frequently uses N-body simulations to make accurate theoretical predictions. However, being numerical expensive they can only be used for inference processes in a limited way, hence analytical or semi-analytical methods need to be investigated. Another key aspect is the interaction of galaxies or galaxy clusters with the ambient LSS which is naturally crucial for all LSS observations, but in particular for weak gravitational lensing as well as the formation of dark matter halos. Lastly one needs to find optimal survey strategies and models which can be tested with those surveys by carrying out forecasts for the inference process. In this thesis we will touch on different aspects of these issues.

First, we will investigate the structure of the parameter space of cosmological parameters by constructing a Lie basis for different objects which live in the space. Of particular importance are covariance matrices, for example the covariance of the weak lensing power spectrum estimator. This matrix needs to be known at each point of the parameter space, or at least at each step of a Monte-Carlo Markov chain (MCMC). Usually the covariance is only given by a suite of N-body simulations. However, we show its variation across parameter space to be captured already

with low order perturbation theory. We also provide a method to identify degeneracy directions of the covariance, thus reducing the amount of numerical simulations needed dramatically.

We then proceed and investigate the interaction of spherical dark matter halos with the ambient LSS within the spherical collapse (SPC) model. This model is itself a key quantity for analytically describing peak counts in the cosmic density field. In this approach we use analytical methods to describe the statistics of the gravitational tidal field in which a test particle, representing the dark matter halo, is embedded in. This leads to rotation and shearing effects. The effect of the tidal interactions on the collapse dynamics is incorporated as a source term in the differential equation which allows us to find the statistics of the critical collapse density δ_c. Being a second order effect, the influence on δ_c enters only in the initial conditions for the linear equation. However, we find differences at the percent level to the standard SPC model.

Lastly, we perform forecasts for next generation cosmological experiments, combining observations of the LSS as well as the CMB and the corresponding cross-correlations to constrain both, the cosmological model and the theory of gravity. In particular we work with general scalar-tensor theories of gravity, called Horndeski theories. Usually forecasting is done using the Fisher matrix but we also run a MCMC to investigate the full shape of the likelihood and compare it with the Gaussian approximation used in the Fisher analysis, giving conservative estimates of the expected statistical errors. We then close with a general discussion on the general structure of parameter spaces in cosmology.

The structure of this thesis is as follows: In Chapter 2 we will review the ΛCDM model discussing its basis at the background and perturbative level as well as possible extensions to this standard paradigm. Chapter 3 discusses observational tests of cosmology with a focus on tests of the LSS and the CMB. In Chapter 4 we describe the Lie basis of covariance matrices, which is followed by the discussion of the SPC model in tidal gravitational field in Chapter 5. Chapter 6 discusses the forecast of future LSS and CMB observations. We summarize in Chapter 7.

Parts of this thesis have already been published in the following papers:

- Describing variations of the Fisher-matrix across parameter space
  B.M. Schäfer, **R. Reischke**
  Published in MNRAS, DOI: 10.1093/mnras/stw1221

- Variations of cosmic large-scale structure covariance matrices across parameter space
  R. Reischke, B.M. Schäfer, A. Kiessling
  Published in MNRAS, DOI: 10.1093/mnras/stw2976

- Spherical collapse of dark matter haloes in tidal gravitational fields
  R. Reischke, F. Pace, S. Meyer, B.M. Schäfer
  Published in MNRAS, DOI: 10.1093/mnras/stw1989

- Effects of tidal gravitational fields in clustering dark energy models
  F. Pace, **R. Reischke**, S. Meyer, B.M. Schäfer
  Published in MNRAS, DOI: 10.1093/mnras/stw3244

- Shear and vorticity in the spherical collapse of dark matter haloes
  R. Reischke, F. Pace, S. Meyer, B.M. Schäfer
  Published in MNRAS, DOI: 10.1093/mnras/stx2610

- Testing (modified) gravity with 3D and tomographic cosmic shear
  A. Spurio Mancini, **R. Reischke**, V. Pettorino, B.M. Schäfer, M. Zumalacáregui
  Submitted to MNRAS, arXiv: 1801.04251

2

PHYSICAL MODELS OF THE UNIVERSE

This chapter will briefly recap the physical basics of the ΛCDM model and how the background evolution of isotropic and homogeneous universes behaves starting from the field equations of GR. Afterwards inhomogeneities on top of the unperturbed background are discussed. We present different perturbation techniques which will be used later in this work. In this context we also introduce statistical concepts to describe structures in the Universe. The chapter is closed with a discussion of possible extensions to the ΛCDM model including fundamental and observational considerations.

2.1 BACKGROUND EVOLUTION

Einstein's field equations connect the geometry of space and time with the matter content in it. Matter influences the structure of space-time and space-time tells matter how to move. Consequently, the equations are highly non-linear and are given by (Einstein, 1915):

$$\mathbf{G} + \Lambda \mathbf{g} = \frac{8\pi G}{c^4}\mathbf{T} \,. \tag{2.1}$$

Here G is Newtons constant, Λ is the cosmological constant and c is the speed of light. $\mathbf{G}$ is the Einstein tensor which is constructed from the Ricci tensor, $\mathbf{R}$, which itself is the trace-full part of the Riemann curvature tensor. Furthermore, $\mathbf{g}$ is the metric and $\mathbf{T}$ is the energy-momentum tensor. The field equations are coupled, hyperbolic and non-linear partial differential equations for the metric. In the general case, solving Eq. (2.1) analytically is an impossible task, one thus has to make symmetry assumptions on the space-time itself and solve Eq. (2.1) for the remaining degrees of freedom. The three major analytic solutions of GR are the Schwarzschild solution, the weak field solution and the cosmological solution. All of them are limiting cases of the theory in the sense that further constraints would yield a trivial solution. Of particular importance for this work are the cosmological solutions.

2.1.1 *Homogeneous and isotropic universes*

Modern cosmology relies on two assumptions, usually dubbed the cosmological principle: the Universe is isotropic and homogeneous when averaged over sufficiently large scales. The scale above which the Universe seems to be both isotropic and homogeneous is roughly 100 Mpc. Both assumptions have be tested against observations and albeit isotropy can be tested easily (e.g with the CMB, Hinshaw et al., 2013; Planck Collaboration XIII, 2015), homogeneity is very hard to test since we only have access to information on our own backward light-cone. Nonetheless, with isotropy being established on an experimental footing homogeneity can be established assuming that our position in the Universe is by no means special. This is

known as the Copernican principle. The most general metric satisfying both assumptions is:

$$ds^2 = -c^2dt^2 + a^2(t)\left[\frac{dr^2}{1-kr^2} + r^2d\Omega^2\right] . \tag{2.2}$$

Likewise, the most general energy-momentum tensor compatible with the cosmological principle is the one of an ideal fluid:

$$\mathbf{T} = (\rho c^2 + P)\mathbf{u}\otimes\mathbf{u} + \mathbf{g}P , \tag{2.3}$$

with pressure $P = P(t)$ and density $\rho = \rho(t)$, which can both only depend on cosmic time t due to homogeneity. Einstein's equations, (2.1), then yield the Friedmann equations which describe the background dynamics of the Universe via two differential equations for the scale factor $a(t)$:

$$\begin{aligned}\left(\frac{\dot{a}}{a}\right)^2 &= \frac{8\pi G}{3}\rho + \frac{\Lambda}{3c^2} - \frac{k}{c^2a^2} ,\\ \frac{\ddot{a}}{a} &= -\frac{4\pi G}{3}\left(\rho + \frac{P}{c^2}\right) + \frac{\Lambda}{3c^2} ,\end{aligned} \tag{2.4}$$

with a dot denoting a derivative with respect to t. Eqs. (2.4) can be reduced to a single equation by providing an equation of state w_i, which relates the pressure of the species i with their density, $P_i = w_i\rho_i c^2$. One distinguishes the following cases: non-relativistic matter $w_m = 0$, relativistic matter $w_r = 1/3$ and the cosmological constant $w_0 = -1$. Furthermore, we introduce the critical density $\rho_{crit} = 3H_0^2/(8\pi G)$ to express all densities in dimensionless density parameters:

$$\Omega_i(a) \coloneqq \frac{\rho_i(a)}{\rho_{crit}(a)}, \quad \Omega_{i0} \coloneqq \left.\frac{\rho_i(a)}{\rho_{crit}(a)}\right|_{a=1} . \tag{2.5}$$

The value $a = 1$ is chosen to correspond to the Universe today. Using those definitions a Friedmann universe filled with relativistic, non-relativistic matter and a cosmological constant obeys the following dynamical law:

$$H^2 = H_0^2\left[\Omega_{mo}a^3 + \Omega_{ro}a^4 + \Omega_\Lambda + \Omega_k a^2\right] = H_0^2E(a)^2 . \tag{2.6}$$

Here we defined the Hubble function and its value today

$$H(a) \coloneqq \frac{\dot{a}}{a}, \quad H_0 = H(a)|_{a=1} = 100h\frac{km}{sMpc} . \tag{2.7}$$

H_0 is called the Hubble constant and $E(a)$ is the expansion function. It is worth noting that the density parameters are not independent, but obey the closure relation:

$$\Omega_k = 1 - \sum_i \Omega_i . \tag{2.8}$$

Furthermore, the scaling with a of the different terms in Eq. (2.6) reflects the dependence on a of the densities of the different species. Since the Universe is expanding a increases with time, thus in the past we find $a < 1$. The structure of Eq. (2.6) shows that there have been different epochs in the Universe during which different species dominated the evolution. Specifying the density parameters and the Hubble constant, the background evolution of the Universe is completely determined.

2.1.2 *Redshift and distance measures*

The wavelength of photons changes in the same way as the scale factor of the Universe is evolving with time because their spatial momentum is changed proportionally to the scale factor. Consequently, they will be redshifted or blueshifted. As our Universe is expanding, we define the redshift in the following way:

$$1 + z = \frac{\lambda_{\text{observed}}}{\lambda_{\text{emitted}}} = \frac{1}{a} \,, \tag{2.9}$$

where we assume that the observations take place at the current epoch, $a = 1$. The redshift serves as a distance proxy in cosmology. However, distances are not uniquely defined in an expanding spacetime. Of particular importance is the comoving distance, χ, which defines distances on rescaled spatial hyper-surfaces and can be calculated as

$$\chi(z) = \chi_H \int_0^z \frac{dz}{E[a(z)]} \,. \tag{2.10}$$

The constant $\chi_H = c/H_0$ is the Hubble radius and gives an estimate of the size of the visible Universe. It relates the redshift measured today to the distance of a source with redshift z measured on a spatial hyper-surface. Another important distance is the proper distance, which measures the distance passed by light in a certain time interval. These two distances are not directly measurable, but one can use them to construct the observable angular diameter distance and the luminosity distance, defined as

$$D_{\text{ang}}(z) = a(z)\chi(z), \quad D_{\text{lum}} = \frac{D_{\text{ang}}(z)}{a^2(z)} \,, \tag{2.11}$$

respectively, for universes with $k = 0$. For curved universes the dependence on χ would change to $\sin(\chi)$ and $\sinh(\chi)$ for $k > 0$ and $k < 0$, respectively. If we are thus given a standard ruler, that is an object with known physical size, we can deduce cosmological parameter and for example find out whether the Universe is spatially flat. This was for example done using the position of the first acoustic peak in the CMB temperature power spectrum (e.g. Hinshaw et al., 2013; Collaboration et al., 2016). Similarly objects of known absolute luminosity can be used as standard candles, as it is done with Type Ia Supernova (SNIa) measurements (e.g. Riess et al., 1998; Perlmutter et al., 1998; 1999; Tonry et al., 2003). More precisely, SNIa are standardizable by using correlations of the width and the peak hight of the light-curves. Most recently, Abbott et al. (2017) used gravitational waves as standard sirens, which work in principle in the same way as standard candles.

2.2 STRUCTURE FORMATION

If the Universe were perfectly homogeneous, no structures such as galaxies, galaxy clusters and ultimately the Earth would exist. More fundamentally, also an arrow of time would not exist in such a universe, provided Eq. (2.4) would hold. The question arises where the structures we see today originated from. Clearly, if small inhomogeneities in the density distribution of the Universe exist, they will grow due to

gravitational interaction. This, however, poses the question where these primordial fluctuations stem from. Currently, the most accepted mechanism is inflation (Guth, 1981) by which the primordial fluctuations are seeded by quantum fluctuations of the inflaton field in an era of rapid accelerated expansion. At the same time this mechanism also solves two problems of CMB observations:

- *Flatness problem*: Any deviation of Ω_k from zero at early times would evolve to a very large curvature parameter today. In order to obtain $\Omega_k \approx 0$ today, it must have been fine tuned to be of the order of 10^{-27} at early times if the other density parameters satisfy $\Omega_\Lambda \approx \Omega_{mo} \gg \Omega_{ro}$. Accelerated expansion automatically pushes Ω_k to zero since the comoving Hubble radius shrinks.
- *Horizon problem*: The CMB is measured to be a perfect black body (Mather et al., 1990) and must thus have been in a state of thermal equilibrium prior to recombination. However, the horizon size at time of recombination is only of the order of a few degrees on the sky. An epoch of accelerated expansion makes the comoving horizon shrink and, if lasting long enough, can account for causal disconnected patches at recombination to have been in causal contact before.

Accelerated expansion is, in the simplest model, realized by a single scalar field ϕ, the inflaton, with a self-interaction potential $V(\phi)$ minimally coupled to gravity. Eqs. (2.4) require $p < -\rho c^2/3$ for $\ddot{a} > 0$, which can be realized if $\dot{\phi}^2 \ll V(\phi)$, i.e. when the field rolls down its potential very slowly. The inflaton field, ϕ, is, as any field theoretical object, a quantum field which will undergo quantum fluctuations due the uncertainty principle. These quantum fluctuations have a characteristic comoving length scale L. Due to the accelerated expansion, the comoving Hubble radius, $c/(Ha) = \chi_{H,com}$ shrinks and eventually we find $L > \chi_{H,com}$. Since the fluctuations now lack of causal contact, they are frozen in and become real macroscopic objects. Once the inflaton field gained enough kinetic energy, inflation ends and the equation of state approaches $p = \rho c^2$ if $V(\phi) \ll \dot{\phi}^2$. The kinetic energy then decays into ordinary energy forms by a process called reheating, starting the radiation dominated phase of the classical Friedmann universe. As the resulting perturbations are superpositions of statistically independent fluctuations of ϕ, they will obey Gaussian statistics due to the central limit theorem. There are, however, more complicated models which yield primordial non-Gaussianities (see e.g. Chen, 2010, for a review). Given those initial perturbations in the density we will now briefly review how the statistical properties of random fields can be described and what the power spectrum of the initial perturbations looks like. Next, we will describe their growth over cosmic time.

2.2.1 *Statistical properties of random fields*

Before we discuss tools to describe the statistical properties of cosmic fields, let us briefly discuss why a statistical approach is necessary in the first place. Cosmological evolution occurs on time-scales much longer than that of possible observations. It is thus impossible to observe the evolution in individual systems. Also, we have no direct observation of the initial conditions of the primordial seeds produced by inflation. Therefore the description of structures in the Universe can only be built

in a statistical framework. The procedure is therefore to derive the statistics of the initial perturbations and to propagate the evolution equations of the perturbations forward in time.

For simplicity we consider a scalar random field, which could for example be the *density contrast*:

$$\delta(\mathbf{x}, t) \coloneqq \frac{\rho(\mathbf{x}, t) - \rho_0(t)}{\rho_0(t)} \,, \tag{2.12}$$

where $\rho_0(t(a)) = \Omega_m(a)\rho_{crit}(a)$ is the mean cosmic background density and $\rho(\mathbf{x}, t) \ll 1$ the perturbation on this background. δ is called *statistically homogeneous* if all its moments are invariant under spatial translations. It is furthermore *statistically isotropic* if all its moments are invariant under spatial rotations. The two-point correlation function is defined as

$$\xi(r) = \langle \delta(\mathbf{x})\delta(\mathbf{x}+\mathbf{r}) \rangle \,, \tag{2.13}$$

where $\langle . \rangle$ denotes an ensemble average. Due to statistical isotropy and homogeneity it only depends on the norm, r, of $\mathbf{r}$. We define the following Fourier convention in n dimensions:

$$\delta(\mathbf{x}, t) = \int \frac{d^n k}{(2\pi)^n} \delta(\mathbf{k}, t) \exp\left[-i\mathbf{x}\cdot\mathbf{k}\right] \,, \quad \delta(\mathbf{k}, t) = \int d^n x \delta(\mathbf{x}, t) \exp\left[i\mathbf{x}\cdot\mathbf{k}\right] \,. \tag{2.14}$$

With this we define the power spectrum of the density contrast:

$$(2\pi)^3 P(k) \delta_D^{(3)}(\mathbf{k} - \mathbf{k'}) \coloneqq \langle \delta(\mathbf{k}, t) \delta^*(\mathbf{k'}, t) \rangle \,, \tag{2.15}$$

which is itself the Fourier transform of the correlation function:

$$P(k) = 2\pi \int_0^\infty r^2 dr \; \xi(r) j_0(kr) \,, \tag{2.16}$$

where $j_0(x)$ is a spherical Bessel function of the first kind of order zero. The moments of the power spectrum are defined as

$$\sigma_j^2 \coloneqq \int_0^\infty \frac{dk}{2\pi^2} P(k) k^{2j+2} \,, \tag{2.17}$$

such that σ_0^2 corresponds to the variance. Information about objects of a certain size can be accessed by smoothing the density field with below a certain scale R, which amounts to a multiplication in Fourier space with a suitable normalized weight function $W_R(k)$. For the variance one thus finds

$$\sigma_R^2 = \int_0^\infty \frac{k^2 dk}{2\pi^2} P(k) W_R^2(k) \,. \tag{2.18}$$

Common filter functions are a Gaussian or a top-hat in real space. All the above definitions can be extended to higher order correlators:

$$(2\pi)^3 P_n(\mathbf{k}_1, \mathbf{k}_2, ..., \mathbf{k}_n) \delta_D^{(3)}(\mathbf{k}_1 + ... + \mathbf{k}_n) \coloneqq \langle \delta(\mathbf{k}_1, t) ... \delta(\mathbf{k}_n, t) \rangle_C \,. \tag{2.19}$$

Here again the Dirac distribution ensures statistical homogeneity. The index C denotes the connected part, corresponding to the cumulants and not the moments of the distribution. The $n = 2$ correlator corresponds to the power spectrum, while the $n = 3$ correlator is called the bispectrum.

2.2.2 *Gaussian random fields*

A special case of a random field is a *Gaussian random field*, which is fully described by its two-point correlation function, or its Fourier transform, the power spectrum. Its joint probability function in d dimensions can be written as:

$$p(\delta_1, ..., \delta_d)d\delta_1...d\delta_d = \frac{1}{\sqrt{(2\pi)^n \det \mathbf{C}}} \exp\left[-\frac{1}{2}\boldsymbol{\delta}^T \mathbf{C}^{-1} \boldsymbol{\delta}\right] , \tag{2.20}$$

where we abbreviated $\delta(\mathbf{x}_i) = \delta_i$ and $\boldsymbol{\delta}^T = (\delta_1, ..., \delta_d)$ and $\mathbf{C} = \langle \boldsymbol{\delta}\boldsymbol{\delta}^T \rangle$. Furthermore, we used $\langle \delta \rangle = 0$. Gaussian random fields have the useful property that all cumulants of higher order than two vanish. In Eq. (2.19) all spectra with $n > 2$ will vanish. This also has some important consequences for higher order moments of the distribution:

$$\langle \delta(\mathbf{k})...\delta(\mathbf{k}_{2n+1}) \rangle = 0 , \quad \langle \delta(\mathbf{k}_1...\delta(\mathbf{k}_{2n}) \rangle = \sum_{\text{all pairs}} \left[\prod_{\text{pair } i,j} \langle \delta(\mathbf{k}_i)\delta(\mathbf{k}_j) \rangle \right] . \tag{2.21}$$

This is Wick's theorem for Gaussian random fields and shows that the correlation function will always decay into products of the power spectrum or completely vanish (Bernardeau et al., 2002).

2.2.3 *Linear growth*

Structure formation can be studied in a Newtonian framework if structures are small compared to the curvature scale of the Universe, which is the Hubble radius, if velocities involved are small, $v \ll c$, and the potentials are weak $|\Phi| \ll c^2$. All three conditions are very well satisfied at late times in the Universe. The field equation is thus given by the Poisson equation:

$$\Delta\Phi = 4\pi G\rho , \tag{2.22}$$

where Φ is the Newtonian potential, G is Newton's constant and ρ the density. Furthermore the cosmic fluid obeys an energy-conservation equation:

$$\partial_t \rho + \boldsymbol{\nabla}(\rho \boldsymbol{v}) = 0 , \tag{2.23}$$

and the Euler equation

$$\partial_t \boldsymbol{v} + (\boldsymbol{v} \cdot \boldsymbol{\nabla})\boldsymbol{v} = -\frac{\boldsymbol{\nabla} P}{\rho} - \boldsymbol{\nabla}\Phi , \tag{2.24}$$

which describes momentum conservation. Here we omitted the dependence on comoving coordinates $\mathbf{x} = \mathbf{r}/a$ and time t for shorthand notation. The equations can be perturbed with respect to their background values ρ_0, $\boldsymbol{v}_0$, P_0 and Φ_0, which leads to the following set of linear perturbation equations in comoving coordinates:

$$\begin{aligned} &\Delta\delta\Phi = 4\pi G\rho_0 a^2 \delta , \\ &\dot{\delta} + \boldsymbol{\nabla} \cdot \delta\mathbf{u} = 0 , \\ &\delta\dot{\mathbf{u}} + H\delta\mathbf{u} = -\frac{\boldsymbol{\nabla}\delta P}{a^2\rho_0} + \frac{\boldsymbol{\nabla}\delta\Phi}{a^2} . \end{aligned} \tag{2.25}$$

Here $\delta\Phi$, $\delta\mathbf{u}$ and δP denote perturbed quantities and δ is the density contrast defined in Eq. (2.12). The system of equations can be closed by introducing the sound speed, which relates pressure to density perturbations

$$\delta p = c_s^2 \rho_0 \delta \, . \tag{2.26}$$

Combining the divergence of the Euler equation with the time derivative of the continuity equation and plugging in Eq. (2.22) yields a single differential equation for the density contrast:

$$\ddot{\delta}(\mathbf{x}, t) + 2H(t)\dot{\delta}(\mathbf{x}, t) - 4\pi G \rho_0 \delta(\mathbf{x}, t) - \frac{c_s^2}{a^2}\Delta\delta(\mathbf{x}, t) = 0 \, . \tag{2.27}$$

For the modes $\delta(\mathbf{k}, t)$ in Fourier space, this differential equation attains the following simple form

$$\ddot{\delta}(\mathbf{k}, t) + 2H\dot{\delta}(\mathbf{k}, t) + \left(\frac{c_s^2 k^2}{a^2} - 4\pi G \rho_0\right) \delta(\mathbf{k}, t) = 0 \, . \tag{2.28}$$

We now introduce the linear growth factor:

$$\delta(t) = D_+(t)\delta_0 \, , \tag{2.29}$$

which is normalized in such a way that $D_+(t_{\text{today}}) = 1$. CDM has $c_s = 0$ and therefore $D_+(t)$ obeys the following equation:

$$\frac{d^2}{da^2} D_+(a) + \left(3 + \frac{d\ln H}{d\ln a}\right) \frac{d}{a da} D_+(a) = \frac{3}{2a^2} \Omega_m(a) D_+(a) \, . \tag{2.30}$$

If $c_s \neq 0$ structures will only grow above a certain scale $\lambda_J \equiv c_s \sqrt{\pi/(G\rho_0)}$, which is called the *Jeans length*.

2.2.4 *Initial power spectrum*

The initial power spectrum predicted by inflation is a power-law with an exponent n_s called *spectral index*:

$$P_{\text{ini}} \propto k^{n_s} \, . \tag{2.31}$$

A dependence of n_s on k is in principle possible and is called running spectral index. However, most inflationary models predict a constant nearly scale-free initial power spectrum. After it shrank, the comoving Hubble radius will start to grow again after inflation ends and perturbations, formerly being of super-horizon size, will enter the horizon. Modes entering the horizon before radiation domination ends will oscillate as shown by Eq. (2.28). Modes that enter the horizon after matter-radiation equality can continue growing as $\delta \propto a^2$ during this epoch. After matter radiation- equality all modes grow as $\delta \propto a$. This leads to a suppression of small scale modes and to the following asymptotic behaviour of the initial power spectrum:

$$P(k) = \begin{cases} k^{n_s} & \text{if } k \leqslant k_{\text{eq}} \\ k^{n_s - 4} & \text{if } k > k_{\text{eq}} \, , \end{cases} \tag{2.32}$$

where k_{eq} is the comoving wave-number of the horizon at matter-radiation equality. The exact transition between the two asymptotic branches is done by a transfer function, which needs to be taken from Boltzmann codes (e.g. Lewis et al., 2000; Lesgourgues, 2011), which solve the Boltzmann equation for the different species. The usual form of the linearly evolved power spectrum is then

$$P_{lin}(k,a) = D_+^2(a)T^2(k,a)P_{ini}(k)\,, \tag{2.33}$$

where $T^2(k,a)$ is the *transfer function* and $D_+(a)$ the normalized linear growth factor. A common choice for $T(k,a)$ for a universe filled with CDM and adiabatic initial conditions is the fitting function (Bardeen et al., 1986)

$$T(k) = \frac{\ln(1+2.34q)}{2.34q}\left[1+3.89q+(16.1q)^2+(5.46q)^3+(6.71q)^4\right]^{-1/4}\,, \tag{2.34}$$

here $q = k\sqrt{\theta}/(\Omega_{mo}h^2\mathrm{Mpc}^{-1})$ and $\theta = \rho_r/(1.68\rho_\nu)$ with the density of neutrinos ρ_ν.

2.2.5 *Non-linear growth*

The description so far is only valid as long as the density contrast is small compared to unity. This assumption will certainly break down at late times during cosmological evolution. Thus the linear description will break down as well and one needs to go to higher order in perturbation theory using the following expansion

$$\delta(\mathbf{x},t) = \sum_{n=1}^{\infty}\delta^{(n)}(\mathbf{x},t)\,, \tag{2.35}$$

and similarly for the velocity divergence, such that $\delta^{(1)}$ corresponds to the linear solution. Plugging this into Eqs. (2.23,2.24) and (2.22) leads to equations for the different orders in perturbation theory. The non-linear terms involve terms which couple different Fourier modes of the density field to each other. This ansatz is referred to as standard perturbation theory (SPT) (see Bernardeau et al., 2002, for a review). For an Einstein-de Sitter cosmology, i.e. $\Omega_{mo}=1$ and $\Omega_k=0$, a general solution can be given (Makino et al., 1992; Kauffmann and White, 1993; Bertschinger and Jain, 1994)

$$\delta(\mathbf{k},t) = \sum_{n=1}^{\infty} a^n(t)\delta_n(\mathbf{k})\,. \tag{2.36}$$

If $a(t)$ is small, i.e. at early times, the linear mode $\delta_1(\mathbf{k})$ dominates. At later times the equations of motion imply the following structure for $\delta_n(\mathbf{k})$:

$$\delta_n(\mathbf{k}) = \int d^3q_1 ... \int d^3q_n \delta_D(\mathbf{k}-\mathbf{q}_{1...n})F_n(\mathbf{q}_1,...,\mathbf{q}_n)\delta_1(\mathbf{q}_1)...\delta_n(\mathbf{q}_1)\,, \tag{2.37}$$

where we introduced $\mathbf{q}_{1...n} = \mathbf{q}_1+...+\mathbf{q}_n$. The functions F_n are homogeneous functions of $\{\mathbf{q}_1,...,\mathbf{q}_n\}$ of zero degree, which can be constructed recursively. For $n=1$ one finds $F_1=1$ and for $n=2$ it is given by (Kauffmann and White, 1993; Bertschinger and Jain, 1994; Bernardeau et al., 2002)

$$F_2(\mathbf{q}_1,\mathbf{q}_2) = \frac{5}{7}+\frac{1}{2}\frac{\mathbf{q}_1\cdot\mathbf{q}_2}{q_1q_2}\left(\frac{q_1}{q_2}+\frac{q_2}{q_1}\right)+\frac{2}{7}\frac{(\mathbf{q}_1\cdot\mathbf{q}_2)^2}{q_1^2q_2^2}\,. \tag{2.38}$$

For more general cosmologies approximate solutions exist (Bernardeau, 1994).

SPT works in a fluid picture by assuming the hydrodynamic equations (2.23,2.24). DM is, however, collisionless as demonstrated impressively by the *Bullet cluster* (Tucker et al., 1998). Therefore SPT must break down when fluid streams cross each other and the velocity field $\mathbf{u}$ is no longer uniquely defined. Quite recently (Bartelmann et al., 2017, kinetic field theory (KFT)) developed a non-equilibrium statistical field theory for classical particles, which describes the dark matter particles as an ensemble occupying phase space subject to Hamiltonian dynamics. This theory does not suffer from the fundamental limitations of SPT. However, as long as multiple streams do not form, i.e. for $k < 0.5\ \mathrm{Mpc}\ h^{-1}$, SPT is applicable.

Another possibility is to rely on numerical N-body simulations (e.g. Jenkins et al., 1997; Couchman, 1997; Springel, 2005; Klypin et al., 2011; Vogelsberger et al., 2014). These simulations use effective particles with different properties, for example dark matter particles interact only gravitationally and have typical masses of $10^9\ M_\odot$. A usual number of particles in such a simulation is $N \sim 10^{9-10}$. The position and momenta of the particles are initially correlated subject to the power spectrum obtained from the CMB and the continuity equation. They are then evolved with analytic methods up to a redshift of roughly 100. For smaller redshifts the simulation solves the full Newtonian dynamical equations numerically on an expanding background. DM only simulation resembles the correlation function of the LSS very well (Eke et al., 1996). Modern simulations also contain baryonic physics and sophisticated subgrid models to describe all kinds of feedback mechanism (Vogelsberger et al., 2014). Although numerical simulations can in principle describe non-linearities correctly to very small scales and also include all kinds of astrophysical processes, they are not practicable in certain situations as they are computationally very expensive. Especially since future cosmological surveys span an enormous amount of different scales, the simulations must cover a large volume, but also provide sufficient resolution. Furthermore, the observable properties of the LSS are of statistical nature, therefore one needs an ensemble of simulations for each individual set of cosmological parameters. On the other hand it is analytically not possible to access all astrophysical effects on galactic scales. It will thus be desirable to achieve the best interplay between analytic and numerical methods for next generation surveys.

2.2.6 *Lagrangian perturbation theory*

An alternative way to set up a perturbative solutions of the non-linearly evolved density field is to follow the trajectories of the fluid elements (Zel'Dovich, 1970; Buchert, 1989). This procedure is called Lagrangian perturbation theory (LPT), with its central object being the displacement potential $\Psi(\mathbf{q})$, where $\mathbf{q}$ is the initial particle position. Ψ is a mapping from these initial positions to final positions $\mathbf{x}$:

$$\mathbf{x}(\eta) = \mathbf{q} - \boldsymbol{\nabla}\Psi(\mathbf{q},\eta)\ . \tag{2.39}$$

with η being the conformal time coordinate $d\eta = da/a$. The corresponding equation of motion is

$$\frac{d^2\mathbf{x}}{d\eta^2} + aH\frac{d\mathbf{x}}{d\eta} = -\boldsymbol{\nabla}\Phi\ . \tag{2.40}$$

LPT can be related to SPT by taking the divergence of Eq. (2.40):

$$\mathcal{J}(\mathbf{q},\eta)\boldsymbol{\nabla}\cdot\left[\frac{d^2}{d\eta^2}+aH\frac{d}{d\eta}\right]\boldsymbol{\nabla}\Psi=\frac{3}{2}\Omega_m(\eta)(aH)^2(\mathcal{J}(\mathbf{q},\eta)-1)\,, \tag{2.41}$$

with the Jacobian of the transformation between Eulerian and Lagrangian frame:

$$\mathcal{J}(\mathbf{q},\eta)\coloneqq\frac{\partial\mathbf{x}}{\partial\mathbf{q}}\,. \tag{2.42}$$

The Jacobian can be calculated using the mass conservation condition $(1+\delta)d^3x = d^3q$ and therefore

$$\mathcal{J}(\mathbf{q},\eta)=\frac{1}{\det[\mathbb{1}+(\boldsymbol{\nabla}\otimes\boldsymbol{\nabla})\Psi]}\,. \tag{2.43}$$

LPT breaks down if the Jacobian vanishes, since the mapping is no longer invertible is this case (meaning that trajectories of particles cross each other) and the density field diverges. The linear solution to Eq. (2.41) is given by (Catelan and Moscardini, 1995):

$$\boldsymbol{\nabla}\cdot(\boldsymbol{\nabla}\Psi)\equiv\Delta\Psi=D_+(\eta)\delta(\mathbf{q})\,, \tag{2.44}$$

where one has to impose that the large scale displacement potential recovers SPT. This is usually referred to as the Zel'dovich approximation (ZA) (Zel'Dovich, 1970).

2.3 BEYOND THE STANDARD MODEL

The model outlined so far assumes GR to be the valid theory of gravity, that the cosmological principle holds and that our Universe is filled with CDM, relativistic matter and baryons. Furthermore, the accelerated expansion observed today is due to the cosmological constant as a second coupling constant in Eq. (2.1). Lastly, the expansion history was preceded by inflation. In this section we will discuss possibilities and reasons why to go beyond this standard picture.

2.3.1 *Fundamental theoretical and observational consideration*

The scenario of inflation is very similar to the late time expansion of the Universe in such a way that both can possibly be driven by a scalar field, however the energy scales involved are very different. Clearly inflation itself cannot be driven by a mechanism like the cosmological constant since it eventually has to end. This, nonetheless, still suggests that both mechanisms might arise from a similar physical process and the inflationary picture should be considered for the late-time accelerated expansion as well. At the very least this will help us to understand the connection between these different building blocks. Furthermore, the cosmological constant has two naturalness problems, which arise from its measured value today and its time evolution.

The first problem is usually called the cosmological constant problem which refers to the fact that Λ, if due to some microscopic field theory, should undergo vacuum fluctuations and will thus have a ground state with non-vanishing energy density, which will act as a cosmological constant. Further contributions arise from phase

transitions during symmetry breaking. Let us for example consider the Higgs field which has a single minimum before the symmetry is broken. During the electroweak transition the former minimum becomes a local extrema and the field will roll into the minimum of the Higgs potential, thus having a non-zero field value and again serving as a Λ-like term. A similar reasoning holds for phase transitions in quantum electrodynamics. For a review we refer to Martin (2012). In summary, the effective cosmological constant observed today is a sum of all contributions and it turns out that they would have to cancel each other very precisely in order to match the observed value for Λ today. It should be noted that the contribution from the vacuum energy due to quantum fluctuations is a back of the envelope calculation and it depends strongly on the renormalization scale of the theory as well as on the background metric considered. Thus in principle the cosmological constant problem should be addressed in a quantum gravity framework which is not yet formulated consistently. Nonetheless, these arguments hint a fine-tuning problem.

Secondly, the so-called coincidence problem refers to Ω_m and Ω_Λ having very similar values today. At the same time their relative contribution scales with a^{-3}. So clearly Λ was completely sub-dominant, i.e. not observable in the past. Furthermore, changing the initial conditions for Λ a bit, one could end up with no structures at all, or alternatively we would never observe Λ in the first place. This situation is very similar to the flatness problem in the inflationary paradigm and again indicates a fine tuning of parameters.

From an observational point of view, a theory can only be proven to be better than an alternative if an alternative theory is provided facing the same observations. Otherwise one might end up constraining a wrong model over and over again, a situation referred to as confirmation bias[1]. Despite its success, the ΛCDM model is very rigid in the sense that slight deviations from a constant Λ can not be captured. Additionally, a lot of observations require a cosmological model to convert the data into something which can be related to theoretical predictions. This is for example the case when converting redshift into a distance, or for baryonic acoustic oscillation (BAO) measurements. Thus investigating cosmologies different from ΛCDM helps us to understand observations in a more model-independent way. Lastly, there is small tension between different cosmological probes, which might be a hint for new physics or can be caused by poorly understood systematics.

Given these considerations one is basically left with three options or a combination of them: First one can give up the cosmological principle. While isotropy is very well tested by observations of the CMB, homogeneity is not testable very easily, since we only have access to our backward lightcone. Therefore we just might live in a large underdense region and thus distant galaxies are moving away from us in an apparent accelerated fashion (Tolman, 1934; Bondi, 1947; Clarkson, 2012). However, combining different observations Redlich et al. (2014) and Meyer et al. (2015) showed that one still needs a cosmological constant to explain the accelerated expansion. In the following section we will discuss the two other possibilities.

1 This situation can, however, also be reversed, since one can always come up with a more complex theory to fit or avoid observational constraints.

2.3.2 *Modifying the matter sector*

With GR assumed to be valid, Eq. (2.4) immediately implies that accelerated expansion can be achieved if an energy species with $p < -\rho/3$ is present. This scenario is usually called DE and the cosmological constant can be interpreted as a DE model with $w = -1$. A straightforward extension would be a phenomenological ansatz Taylor expanding $w(a)$ around its fiducial value (Chevallier and Polarski, 2001; Linder, 2003). The first principle starting point would be to postulate an action for some field φ which can drive accelerated expansion:

$$S_\varphi = \int \eta \left(\frac{1}{2} \partial_\mu \varphi \partial^\mu \varphi + V(\varphi) \right) . \tag{2.45}$$

This situation is often referred to as *Quintessence* and the equations of motion for the field, φ, are given by a Klein-Gordon type equation including a friction term due to the Hubble expansion (see Copeland et al., 2006; Tsujikawa, 2010, for reviews). These models are restricted to $w \geqslant -1$ and can be categorized into thawing, freezing and tracking models depending whether the field is held by the Hubble friction, freezes at $w = -1$ at later times, or tracks the dominant energy component respectively. The last ones are often called early DE, alleviates the coincidence problem and increases the Hubble function at all times, thus reducing structure formation (Copeland et al., 1998; Doran and Robbers, 2006; Skordis et al., 2006). Other *Quintessence* models have very little effect on structure formation and only impact the background evolution. The reason for this is that perturbations of φ have a speed of sound $c_s = c$ and a mass of the order of the Hubble scale (in natural units). Therefore clustering only happens on scales comparable to the Hubble horizon. Eq. (2.45) can be generalized to k-*essence*, allowing for non-canonical kinetic terms in the action.

In general dark energy can also cluster, even though its perturbations are small compared to the matter perturbations, however they can still influence the formation of matter perturbations. The key quantity to describe the perturbations in the dark energy component is the effective sound speed $c_s^2 \equiv \delta P/\delta\rho$ where $c_s = 0$ corresponds to full clustering. Especially for k-*essence* models c_s can be much smaller than c as in the case of CDM. Therefore, there can be a direct influence on linear and non-linear structure growth.

2.3.3 *Modifying the gravity sector*

The final possibility is to modify the field equations (2.1) by changing the underlying action. It is however necessary to acknowledge the simplicity and success of GR, which has been tested over a lot of scales, for example in the weak field regime through perihelion precession of mercury, light deflection and spin precession (see Berti et al., 2015, for a review).

When modifying GR, it is important to keep two theorems in mind: (i) higher than 2nd order in the field derivatives will generally lead to instabilities, which can be avoided by considering non-canonical kinetic terms. (ii) Lovelock's theorem states that any metric, 2nd order, local energy-momentum conserving theory of gravity in four space-time dimensions is uniquely given by the *Einstein-Hilbert* action including a cosmological constant (Lovelock, 1974). Additional care must be taken since some

theories seem to violate the Ostrogradski theorem but can effectively be cast into a theory which satisfies it. One example would be $f(R)$ gravity, which can be cast into a metric theory with an additional scalar degree of freedom, which is stable and circumvents Lovelock's theorem by adding this additional field. This turns out to be a very general class of theories which we will therefore discuss in the following.

Scalar-tensor theories

In this thesis we will in particular investigate scalar-tensor theories of gravity, whose action can be written as

$$S = \int \eta \left[f(\varphi) \frac{R}{16\pi G} - \frac{1}{2} \nabla_\mu \varphi \nabla^\mu \varphi - V(\varphi) \right] + S_{\text{matter}}(\mathbf{g}, \boldsymbol{\psi}) \,, \tag{2.46}$$

where $\eta = \sqrt{-g} d^n x$ is the canonical volume form, φ is the additional scalar degree of freedom and $\boldsymbol{\psi}$ encodes all matter fields. Eq. (2.46) can be cast into the Einstein frame by a conformal transformation of the metric and a redefinition of φ to keep the structural form of its Lagrangian:

$$S = \int \eta \left[\frac{R}{16\pi G} + \nabla_\mu \tilde{\varphi} \nabla^\mu \tilde{\varphi} - V(\tilde{\varphi}) \right] + S_{\text{matter}}(f^{-1}(\tilde{\varphi}) \mathbf{g}, \boldsymbol{\psi}) \,. \tag{2.47}$$

The difference between Eq. (2.46) and (2.47) is that for the first the gravity term has a non-standard form, while the coupling to matter fields is canonical. The second one retains the standard *Einstein-Hilbert* term in the action, but the metric coupling to the matter fields explicitly depends on the scalar degree of freedom. One might therefore rewrite the action in the following form

$$S = \int \eta_G R(\mathbf{g}_G) + \int \eta_M \mathcal{L}(\mathbf{g}_M, \boldsymbol{\psi}) \,, \tag{2.48}$$

where we have two different metrics, one acting only on the gravity sector and another one coupling the matter fields. Bekenstein (1993) wrote down the most general relation between $\mathbf{g}_M$ and $\mathbf{g}_G$, which is basically given by

$$\mathbf{g}_M = A(\varphi, X) \mathbf{g}_G + B(\varphi, X) \boldsymbol{\nabla} \varphi \otimes \boldsymbol{\nabla} \varphi \,, \tag{2.49}$$

where X denotes the canonical kinetic term of the scalar field. Observations are performed in the frame of (2.46). A theory which is consistent with current observations should therefore have an acceleration mechanism when expressed in this frame, which is called *Jordan frame*. Furthermore, we can generalize Lovelock's theorem by dropping the assumption of having a metric only, in other words, what is the most general scalar tensor theory, which has second order equations of motion. The gravity Lagrangian in this case is given by the following form (Horndeski, 1974)

$$S[\mathbf{g}, \varphi] \propto \int \eta \sum_{i=2}^{5} \mathcal{L}_i[\mathbf{g}, \varphi], \tag{2.50}$$

where the individual terms can be brought into the following form (de Felice et al., 2011)

$$\begin{aligned}
\mathcal{L}_2 &= G_2(\varphi, X), \\
\mathcal{L}_3 &= -G_3(\varphi, X)\Box\varphi, \\
\mathcal{L}_4 &= G_4(\varphi, X)R + G_{4X}(\varphi, X)\left[(\Box\varphi)^2 - \varphi_{;\mu\nu}\varphi^{;\mu\nu}\right], \\
\mathcal{L}_5 &= G_5(\varphi, X)G_{\mu\nu}\varphi^{;\mu\nu} \\
&\quad - \frac{1}{6}G_{5X}(\varphi, X)\left[(\Box\varphi)^3 + 2\phi_{;\mu}{}^{\nu}\varphi_{;\nu}{}^{\alpha}\varphi_{;\alpha}{}^{\mu} - 3\varphi_{;\mu\nu}\varphi^{;\mu\nu}\Box\varphi\right],
\end{aligned} \tag{2.51}$$

where we denoted a covariant derivative by a semicolon, $\nabla_\mu \coloneqq \varphi_{;\mu}$. Note that the term $\mathcal{L}_2$ corresponds to a standard k-essence DE. Furthermore higher derivative terms in the field equations will cancel each other due to the antisymmetry of the terms containing $\varphi_{;\mu\nu}$. GR is naturally recovered for constant $G_4(\varphi, X)$, while all other G_i vanish. The theory is completely specified if all four functions G_i are provided.

Screening

An important ingredient for all modified gravity theories which have a significant impact on cosmological scales is a screening mechanism. They effectively hide modifications at small scales to provide agreement with small scale tests of GR. Quite generally they can be divided into potential and kinetic screening mechanisms. If one uses an additional scalar field φ, the interaction potential is given by a Yukawa potential with characteristic scale m_φ, which describes the range of the interaction. If the mass of the scalar, m_φ depends on the environment in such a way that it is large if the density is high, GR will be recovered in these regions. This can be achieved by a suitable choice of the interaction potential of the scalar field, since the mass corresponds to its second derivative. This is called *Chameleon mechanism* (Khoury and Weltman, 2004b; a). A kinetic screening is for example the *Vainshtein mechanism* (Vainshtein, 1972), for which the kinetic term X screens modifications on small scales.

Structure growth in modified gravity

Structure formation for MG theories is more difficult than for GR since the equations are more complicated, especially the growth factor (2.30) can become scale dependent.

For linear structure formation in modified gravity one starts from a perturbed background model in Newtonian gauge

$$ds^2 = -(1 + 2\Psi)c^2dt^2 + a^2(1 - 2\Phi)dx^2 . \tag{2.52}$$

Here non-relativistic particles with $v \ll c$ feel gradients in Ψ, while massless particles feel the sum of both potentials Ψ and Φ, which is usually referred to as gravitational slip. In GR one finds $\Phi = \Psi$. A common approach to describe the relations of the perturbations in Φ and Ψ to the density contrast is to introduce the following to functions γ and μ:

$$k^2\Psi = -4\pi G a^2 \rho\delta\mu(k, a), \quad \Phi = \gamma(k, a)\Psi . \tag{2.53}$$

As we will see in Chapter 3 the observables of the LSS will depend on these functions. The linear perturbations in Horndeski theories can be described by using the effective field theory (EFT) formalism. That is, solving for a specified background evolution and then for the linear perturbations. In Horndeski theories this procedure requires the specification of five functions, which depend on time only. There are two general types of functions, those which influence background and perturbations and those which only influence the growth of perturbations at linear order. The EFT action for the linear perturbations is given by (Bloomfield, 2013; Bellini and Sawicki, 2014; Gleyzes et al., 2014)

$$S^{(2)} = \int d^3x\, dt\, a^3 \frac{M_*^2}{2}\Big[\delta K^i_j \delta K^j_i - \delta K^2 + R\delta N + (1+\alpha_T)\delta_2\sqrt{h}Ra^{-3} + \alpha_K H^2 \delta N^2 + 4\alpha_B H \delta K \delta N\Big] + S^{(2)}_{\text{matter}}[\mathbf{g}, \psi]\,. \tag{2.54}$$

Here M_* is the effective Planck mass, N the lapse function, $\mathbf{K}$ the extrinsic curvature, R the Ricci scalar and H the Hubble function. The action of the matter perturbation is described in the Jordan frame and is denoted by $S^{(2)}_{\text{matter}}$. Therefore the action is described by four functions if we take the background evolution as given by a cosmological model:

- *Kineticity*, α_K, relates to the kinetic energy of the perturbations and reduces the sound speed of scalar perturbations.
- *Braiding*, α_B, causes dark energy to cluster and mixes the kinetic terms in the metric with the ones in the scalar degree of freedom.
- *Tensor speed excess*, α_T, describes the deviation of the propagation speed of tensorial modes from the speed of light, thus leading to anisotropic stress.
- *Running of the Planck mass*, α_M, while the Planck mass itself does not yield a different gravitational theory if only changed by a constant, its running will create anisotropic stress and alter the relation between the density and the potential.

Once the functions are set, the theory is fully specified at the background level and at linear order in perturbation theory. In certain limits the α-functions can be related to the phenomenologically motivated functions μ and γ. However, one gets them also by solving the Boltzmann equation for the different perturbations numerically as we will discuss in Section 3.1.

3

OBSERVATIONAL PROBES

In Chapter 2 we introduced a class of spherically symmetric and homogeneous models for our Universe and described their dynamical properties and how perturbations on top of the homogeneous background evolve. We will now introduce some phenomenology in this chapter and investigate some of the key observation probes of the cosmological standard model which can be used to measure the cosmological parameters. Earlier we already discussed the concept of standard candles and rulers. However, SNIa only probe the background expansion, at least at lowest order. In Section 2.3 we then saw that different cosmological models can have the same expansion history but different perturbations, it is therefore necessary to study observables which probe the structures in our Universe and compare them to model predictions. In particular we will discuss the CMB, weak gravitational lensing and galaxy clustering. There are also other probes, which we will not describe here, such as redshift space distortions (e.g. Tadros, 1993; Ballinger et al., 1995; Ryden, 1995) or galaxy cluster counts (e.g. Noonan, 1974; Majumdar, 2004; Lacasa and Rosenfeld, 2016) to name a few. For all plots in this chapter the cosmological parameters used are the reference ones from Table 4.

3.1 COSMIC MICROWAVE BACKGROUND

When the Universe had a thermal energy of the order of 0.1 MeV (corresponding to a redshift of 10^9) light elements could form, this epoch is called primordial nucleosynthesis. The abundance fraction of a light element, A, relative to the number of baryons is controlled by the binding energy of the element in question, B_A and by the baryon to photon ratio η_b. The latter is measured to be 10^{-9}, which means that the elements formed only after the temperature dropped well below B_A. Due to its high density and temperature, the radiation is thermalized quickly during this time and thermal equilibrium is maintained until the reaction rate drops below the expansion rate $\tau \sim H^{-1}$, this process is called particle freeze-out. From the production of Deuterium Gamow (1948) estimated the temperature of the CMB today to be of the order of 10 K, since the CMB is a perfect black body (Penzias and Wilson, 1965; Wright et al., 1992; Fixsen et al., 1996) and thus constrains processes that would pump energy into the photon baryon plasma before decoupling. Thermal equilibrium is mainly maintained due to radiative Compton scattering and later Compton scattering. If energy is dumped into the electrons, Compton scattering distributes it back to the CMB. At low frequencies Bremsstrahlung is also important to maintain thermal equilibrium at the electron temperature.

As long as the process, $p + e^- \leftrightarrow H + \gamma$, is still fast compared to τ, the ionization fraction is kept at its equilibrium value. Since η_b is so small, the electrons and protons recombine, again much later as one would naively expect, at a temperature of $T \approx 0.3$ eV. At this point the scattering between H and γ happens for the last time, the corresponding spatial hyper-surface is thus called last-scattering surface. The latter

estimate is determined by Saha's equation. An exact treatment would also involve a contribution from the recombination of Helium in addition to Hydrogen (e.g. with RECFAST Seager et al., 2000). After recombination the Universe stayed neutral until $z \approx 10$.

In the following section we will discuss how inhomogeneities in the early Universe are imprinted on the temperature and polarization maps of the CMB.

3.1.1 *Temperature anisotropies basics*

Having a black body spectrum, the angular distribution of the CMB can be characterized by its temperature, $T(\hat{n})$, which is decomposed into spherical harmonics for convenience:

$$\Theta(\hat{n}) \coloneqq \frac{T(\hat{n}) - T_0}{T_0} = \sum_{\ell m} \Theta_{\ell m} Y_{\ell m}(\hat{n}) \,, \tag{3.1}$$

where $\hat{n}$ is a vector pointing to a position on the unit sphere and $T_0 = \langle T(\hat{n}) \rangle$. If the fluctuations are statistically isotropic and homogeneous the power spectrum is diagonal in m and ℓ

$$\langle \Theta_{\ell m} \Theta^*_{\ell' m'} \rangle = \delta_{\ell \ell'} \delta_{m m'} C(\ell) \,. \tag{3.2}$$

One frequently considers the quantity

$$\mathcal{C}(\ell) \coloneqq \frac{\ell(\ell+1)}{2\pi} C(\ell) \approx \frac{k^3 P(k)}{2\pi^2} \equiv \Delta^2_T \,, \tag{3.3}$$

where the approximation holds if Δ^2_T is constant around the peak of the spherical Bessel function $j_\ell(k\chi_*)$, with χ_* being the comoving distance to the surface of last scattering. $\mathcal{C}(\ell)$ is a measure for the variance per logarithmic multipole interval, $\ln \ell$.

The dominant process in the plasma before the CMB is released is Thomson scattering with the Thomson cross section, $\sigma_T = 6.65 \times 10^{-25}$ cm^2, corresponding to a comoving mean free path

$$\lambda_C = \frac{1}{n_e \sigma_T a} \,, \tag{3.4}$$

where n_e is the density of free electrons. For typical cosmologies λ_C is of the order of a couple of Mpc and thus much smaller than the comoving horizon, showing that the baryons are tightly coupled to the photons, therefore sharing the same bulk motion.

In order to understand the basic pattern of the temperature power spectrum we will assume a tightly coupled fluid with the following continuity equation for the number density of photons:

$$\frac{dn_\gamma}{d\eta} + \frac{3}{a}\frac{da}{d\eta} n_\gamma + \boldsymbol{\nabla} \cdot (n_\gamma \boldsymbol{v}_\gamma) = 0 \,, \tag{3.5}$$

with the perturbed version at linear order being

$$\frac{d}{d\eta}\left(\frac{\delta n_\gamma}{n_\gamma}\right) = -\boldsymbol{\nabla} \cdot \boldsymbol{v}_\gamma \,, \tag{3.6}$$

which can be rewritten in terms of temperature fluctuations Θ, since $n_\gamma \propto T^3$:

$$\frac{d\Theta}{d\eta} = -\frac{1}{3}\boldsymbol{\nabla}\cdot\boldsymbol{v}_\gamma \,. \tag{3.7}$$

Momentum conservation is again expressed via the Euler equation, by exploiting that the energy density of the photons $\rho_\gamma \propto a^{-4}$ and that $p_\gamma = \rho_\gamma/3$ we can write:

$$\frac{d\boldsymbol{v}_\gamma}{d\eta} = -\boldsymbol{\nabla}\Theta \,. \tag{3.8}$$

Eq. (3.7) and (3.8) can be combined to form an oscillator equation in Fourier space

$$\frac{d^2}{d\eta^2}\Theta(k) + c_s^2 k^2 \Theta(k) = 0 \,, \tag{3.9}$$

where $c_s^2 = 1/3$ is the adiabatic speed of sound. The sound horizon is defined as

$$\chi_s \coloneqq \int c_s d\eta \,. \tag{3.10}$$

Solutions to Eq. (3.9) correspond to standing waves in real space, which oscillate until electrons and protons recombine and the density of the free electrons available for Thomson scattering drops drastically. When this happens, the propagation speed of the waves basically drops to zero, as the electrons are no longer coupled to the photons. They can thus be seen today as anisotropies in the temperature map. In particular $\Theta(\eta_*) \propto \cos(k\chi_*)$ is a solution to Eq. (3.9), clearly extrema occur at wavenumbers $k_n = n\pi/\chi_*$ for positive integer n. The first peak corresponds to the following scale:

$$\ell_s = k_s D_{ang} \,, \tag{3.11}$$

which can serve as a test of the spatial geometry of the Universe. If the Universe is flat we find $\ell_s \approx 200$ for typical parameter values. On top of this simple argument for the BAO signal there are also other effects, such as the Doppler effect due to the relative motion of the plasma with respect to the observer introduced by the BAO motion itself. A simple analysis shows that they are in principle of equal amplitude but phase-shifted by $\pi/2$. Thus quadratically adding both contributions would lead to a scale free power spectrum at recombination. This summation is, however, not correct since the Doppler effect depends on the projection of the velocity onto the line of sight $\boldsymbol{v}_\gamma \cdot \hat{\boldsymbol{n}}$. Thus the peak is dominated by Θ and not by $\boldsymbol{v}$. Furthermore, gravitational forces also play a role in the formation of the peaks which we neglected so far completely. To include them, one perturbs the background metric by the two Bardeen potentials Ψ and Φ, note that a Newtonian approach is not sufficient here, yielding the following evolution equation:

$$\frac{d^2\Theta}{d\eta^2} + c_s^2 k^2 \Theta = -\frac{k^2}{3}\Theta - \frac{d^2\Phi}{d\eta^2} \,. \tag{3.12}$$

The potential is generated by the matter fluctuations via the Poisson equation as in (2.22). In a matter dominated epoch the Newtonian potential is constant and we can rewrite Eq. (3.12) as

$$\frac{d^2}{d\eta^2}(\Theta + \Psi) + c_s^2(\Theta + \Psi) = 0 \,, \tag{3.13}$$

displacing the minimum of the solution to (3.9), in the sense that the temperature fluctuations observed change from Θ to $\Theta + \Psi$. Ψ thus corresponds to a gravitational redshift contribution. The splitting in these two pieces has no invariant meaning and can be transformed away by a gauge transformation, with which the observed temperature can be written as

$$\Theta + \Psi = \frac{\Psi}{3} \,, \tag{3.14}$$

which is known as the Sachs-Wolfe (SW) effect (Sachs and Wolfe, 1967), thus cold spots correspond to over-dense regions.

In reality the situation is more complicated than outlined in this basic discussion. First, one needs to add the inertial effect of baryons, which adds additional mass to the plasma and thus increases the momentum density. This modifies the oscillator equation for tightly coupled baryons. Secondly, the ratio of the momentum density of photons and baryons evolves with time. Furthermore, one needs to extend the calculations beyond the matter dominated epoch and thus the evolution of the potential Ψ will be different and will eventually act as a driving force of the oscillations, which would be absent in a matter dominated era as the potentials would stay constant. Finally, one needs to treat the imperfections of the fluid due to the mean free path of Compton scattering as the diffusion is strong at this scale and the baryons are no longer tightly coupled. This is called *Silk damping* (Silk, 1967).

3.1.2 *Polarization anisotropies*

Thomson scattering generates linearly polarized radiation if the incoming radiation has a spatial quadrupole. Generally the polarization is much smaller than the temperature isotropy and is thus mainly associated with the acoustic peaks of the temperature power spectrum. It was first detected by Kovac et al. (2002).

The statistical description proceeds similar to the one of the temperature anisotropies with the only complication being the tensorial nature of the polarization. Quite generally one can express the statistical properties of the polarization matrix $\mathbf{P}$ in a complete basis:

$$\mathbf{P} \coloneqq \langle \mathbf{I}(\hat{\mathbf{n}})\mathbf{I}^{\dagger}(\hat{\mathbf{n}})\rangle = \theta(\hat{\mathbf{n}})\sigma_0 + U(\hat{\mathbf{n}})\sigma_1 + V(\hat{\mathbf{n}})\sigma_2 + Q(\hat{\mathbf{n}})\sigma_3 \,, \tag{3.15}$$

where σ_μ are the Pauli matrices. Here V defines the circular polarization states, while Q and U describe the linear polarization states. The latter are called Stokes parameters, which play a crucial role in weak lensing as well. However, the distinction between both depends on the choice of the coordinate system. A better decomposition in terms of parity states is

$$Q(\hat{\mathbf{n}}) \pm iU(\hat{\mathbf{n}}) = -\sum_{\ell m} [E_{\ell m} \pm iB_{\ell m}]_{\pm 2}Y_{\ell m}(\hat{\mathbf{n}}) \,, \tag{3.16}$$

where we introduced the spin-2 spherical harmonics ${}_{\pm 2}Y_{\ell m}$ and the E and B mode contributions. The spherical harmonics obey the usual orthogonality relation and one can describe the power spectra

$$\begin{aligned} \langle E^*_{\ell m} E_{\ell m}\rangle &= \delta_{\ell\ell'}\delta_{mm'}C_\ell^{EE} \,, \\ \langle B^*_{\ell m} B_{\ell m}\rangle &= \delta_{\ell\ell'}\delta_{mm'}C_\ell^{BB} \,, \\ \langle \Theta^*_{\ell m} E_{\ell m}\rangle &= \delta_{\ell\ell'}\delta_{mm'}C_\ell^{\Theta E} \,, \end{aligned} \tag{3.17}$$

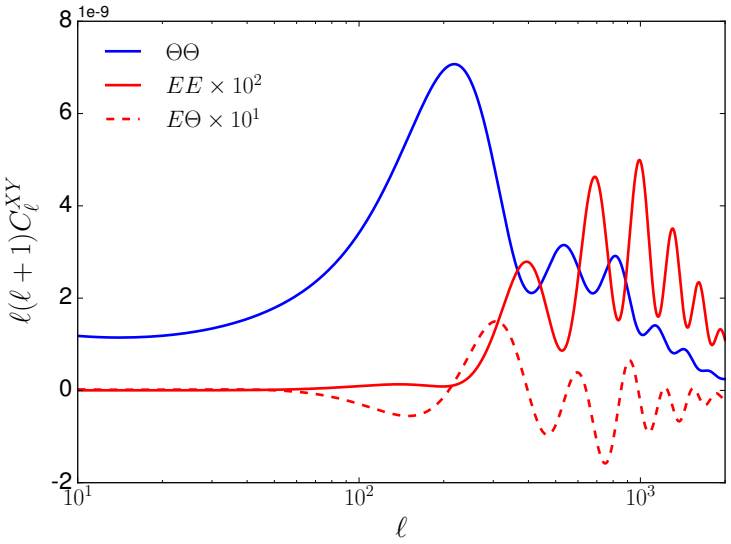

Figure 3.1: CMB temperature, θ, polarization E-mode power and the corresponding cross spectrum as produced by `HiCLASS`. Note that the modes are normalized to the CMB temperature and are therefore dimensionless. The E-modes are amplified by a factor 10 to emphasize their features.

with all other spectra vanishing due to parity considerations. The basic polarization pattern of Thomson scattering can be directly seen from its differential cross section, which involves a scalar product between the incoming and outgoing polarization vectors. Polarization oscillations are out of phase with the temperature oscillations.

3.1.3 *Spectra from Boltzmann codes*

Even though the basic structure of the temperature and polarization anisotropies can be understood analytically, the accurate spectra have to be calculated numerically. The system of equation which needs to be solved is a set of Boltzmann type equations for the different particle species on a background cosmology in a particular gauge (Ma and Bertschinger, 1995). Integrating the equations then yields the fluctuation in temperature and polarization which allows for the calculation of the different spectra. There are quite a few such Boltzmann codes out there, for example `CMBFAST`, `CAMB`, `CMBEASY` and `CLASS` (Seljak and Zaldarriaga, 1996; Lewis et al., 2000; Doran, 2005; Lesgourgues, 2011), which work with different programming languages and algorithms. These codes usually work with cosmological models assuming GR, however, there exist other codes, which can also incorporate deviations from GR such as `EFTCAMB` or `HiCLASS` (Hu et al., 2014; Zumalacarregui et al., 2016). In Figure 3.1 the temperature anisotropy and polarization power spectra are shown. One can clearly see the acoustic peaks in ΘΘ and their damping at high ℓ. On very large scales an integrated version of the SW effect becomes important, which occurs due to evolving gravitational potentials and an effective wavelength change of the photons. The amplitude of the E-mode spectrum is much smaller than the one of the temperature spectrum and is therefore amplified by a 10^2. The acoustic peaks are of

phase with the ones of the temperature due to the directional dependence on the momentum of Thomson scattering. Lastly, the dashed curve shows the cross-correlation of the temperature with the polarization showing combined features of both curves.

3.2 WEAK GRAVITATIONAL LENSING

Gravitational lensing studies the bending of light by massive objects. For detailed introductions to the topic we refer to Straumann (1991) and Schneider et al. (1992). If we are given a single lens at distance D_d and a source at distance D_s, the lens equation is given by

$$\boldsymbol{\beta} = \boldsymbol{\theta} - \boldsymbol{\alpha}(\boldsymbol{\theta}) \,, \tag{3.18}$$

with the scaled deflection angle $\boldsymbol{\alpha}$, the observed position $\boldsymbol{\theta}$ and the true position $\boldsymbol{\beta}$. Note that all vectors involved are two dimensional objects. Clearly Eq. (3.18) can have multiple solutions for given $\boldsymbol{\beta}$, showing that multiple images can occur. If this happens a lensing system must be what is called a strong lens. Here we will only consider situations where the change in image shapes is of the order of a percent. The deflection angle, $\boldsymbol{\alpha}$, can be written in terms of a potential, the lensing potential, $\boldsymbol{\alpha} = \boldsymbol{\nabla}\psi$. Now the lens mapping (3.18) can be linearized locally such that images are distorted according to

$$\mathcal{A}(\boldsymbol{\theta}) \coloneqq \frac{\partial\boldsymbol{\beta}}{\partial\boldsymbol{\theta}} = \begin{pmatrix} 1-\kappa-\gamma_1 & -\gamma_2 \\ -\gamma_2 & 1-\kappa+\gamma_1 \end{pmatrix} \,, \tag{3.19}$$

where we defined the complex shear $\gamma \equiv \gamma_1 + i\gamma_2$ and the convergence κ with components

$$\gamma_1 = \frac{1}{2}\left(\partial_{11}\psi - \partial_{22}\psi\right) \,, \quad \gamma_2 = \partial_{12}\psi \,, \quad 2\kappa = \Delta\psi \,. \tag{3.20}$$

The key observable of weak lensing measurements is the complex ellipticity of the images, which is for example determined by the brightness moments of the images. It is a good estimator for the reduced shear: $g \coloneqq \gamma/(1-\kappa)$. In the weak lensing regime $\kappa \ll 1$ and thus $\gamma \approx g$.

3.2.1 *Cosmic shear*

Weak gravitational lensing by the LSS is called cosmic shear. We set up the equation of geodesic deviation which governs the propagation of a light bundle in a general space time:

$$\frac{d^2\xi}{d\lambda^2} = \mathcal{T}\xi \,, \tag{3.21}$$

with the optical tidal matrix $\mathcal{T}$. λ is an affine parameter of the curve and ξ is the transverse separation of neighbouring geodesics. In presence of weak perturbations relative to a spatially flat Friedmann-Lemaître-Robertson-Walker (FLRW) background the local deflection is given by

$$\frac{d^2\boldsymbol{x}}{d\chi} = -\frac{2}{c^2}\delta\left(\boldsymbol{\nabla}_\perp\Phi[\boldsymbol{x}(\boldsymbol{\theta},\chi),\chi]\right) \,, \tag{3.22}$$

where δ denotes the difference in the gradients perpendicular to the line of sight $\boldsymbol{\nabla}_\perp$ and $\mathbf{x}$ is a comoving separation. Eq. (3.22) is solved by the following Green's function

$$G(\chi,\chi') = \chi - \chi' \quad \text{if } \chi > \chi' \,. \tag{3.23}$$

The inhomogeneity can then be integrated to find a solution for $\mathbf{x}$, which involves an integration of $\boldsymbol{\nabla}_\perp\Phi$ along the true path of the neighbouring rays. One typically assumes that the separation changes due to lensing is small compared to the actual separation of the unperturbed rays. This procedure is known as the Born approximation from scattering processes. The comoving separation of two light rays propagating through the unperturbed background is given by $\mathbf{x} = \chi\boldsymbol{\theta}$, which yields for the deflection angle

$$\boldsymbol{\alpha}(\boldsymbol{\theta},\chi) = \frac{\chi\boldsymbol{\theta} - \mathbf{x}(\boldsymbol{\theta},\chi)}{\chi}\frac{2}{c^2}\int_0^\chi d\chi' \frac{\chi-\chi'}{\chi}\boldsymbol{\nabla}_\perp\Phi(\chi'\boldsymbol{\theta},\chi') \,. \tag{3.24}$$

To arrive at (3.24) we used three well satisfied approximations: first that the Newtonian potential is small, i.e. $|\Phi| \ll c^2$, second that perturbations responsible for deflections are small compared to the Hubble radius and third that corrections can be calculated relatively to the fiducial ray.

The convergence is the derivative of the deflection angle. For cosmological weak lensing it takes the following form

$$\kappa(\boldsymbol{\theta},\chi) = \frac{1}{c^2}\int_0^\chi d\chi' \frac{(\chi-\chi')\chi'}{\chi}\boldsymbol{\nabla}_\perp\cdot\boldsymbol{\nabla}_\perp\Phi(\chi'\boldsymbol{\theta},\chi') \,, \tag{3.25}$$

where we used Eq. (3.24). One can now use the perturbed Poisson equation (2.25) to replace the two dimensional Laplacian in (3.25) by augmenting the line of sight contribution which would average to zero in the limits used here. Since Eq. (3.25) is the convergence for a fixed source at comoving distance χ, we can straightforwardly expand this to a source distribution $G(\chi)$. Furthermore, the convergence is an integrated quantity of the Newtonian potential and evolutionary information of the Universe gets wiped out. This information is, however, crucial if one wants to constrain for example dark energy. A way out is to use tomographic methods (Hu, 1999) by splitting the sources into redshift bins. Since photons from different bins will partially go through the same structure, there will be a non-vanishing cross-correlation between the bins, which allows to restore information about the evolution of the Universe. The effective convergence in tomographic bin i is then given by

$$\kappa_i(\boldsymbol{\theta}) = \frac{3\Omega_{m0}}{2\chi_H^2}\int_0^{\chi_H} d\chi\, W_i(\chi)\chi\frac{\delta(\chi,\boldsymbol{\theta},\chi)}{a(\chi)} \,, \tag{3.26}$$

with the weighting function

$$W_i(\chi) = \int_{\min(\chi,\chi_i}^{\chi_{i+1}} d\chi' p(\chi')\frac{\chi'-\chi}{\chi'} \,. \tag{3.27}$$

Here the sources are distributed according to $p(z)dz = p(\chi)d\chi$. For *Euclid* $p(z)$ is given by (Laureijs et al., 2011):

$$p(z)dz \propto z^2 \exp\left[-\left(\frac{z}{z_0}\right)^\beta\right] \,, \tag{3.28}$$

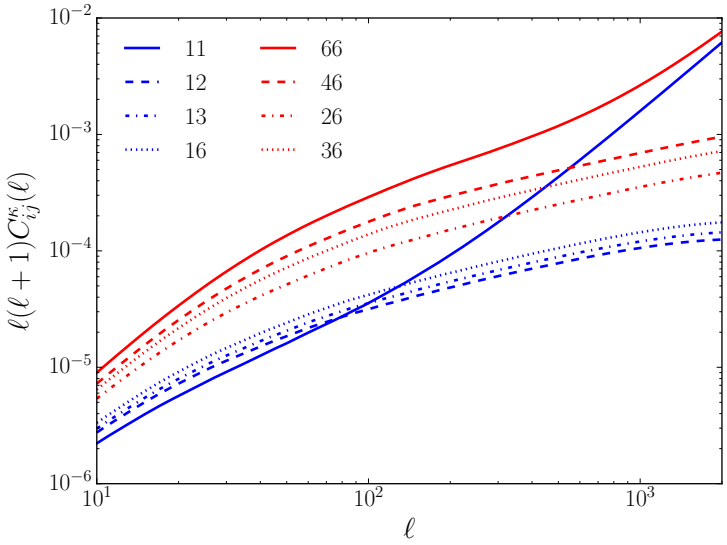

Figure 3.2: Convergence angular power spectrum C^{κ}_{ij} for a survey with 6 tomographic bins. Solid lines show auto-correlations, while dashed and dotted lines show cross-correlation between different bins.

with $\beta = 1.5$ and $z_0 \approx 0.9$. Individual galaxies cannot be used to determine cosmic shear since the effect is too small and galaxies are intrinsically elliptical. However, the coherent distortion of neighbouring galaxy images as a function of angular scale can be measured, i.e. the correlation function or alternatively the angular power spectrum. Since the convergence is a weighted projection of the density, its statistical properties have been derived under the assumption of a finite correlation length much smaller than the Hubble radius by Limber (1953). In Fourier space the tomographic cosmic shear power spectrum in tomographic bins i and j is given by:

$$C^{\kappa}_{ij}(\ell) = \int \frac{d\chi}{\chi^2} W_i(\chi) W_j(\chi) P(\ell/\chi, \chi) \, . \tag{3.29}$$

Observed cosmic shear spectra suffer from a shape noise contribution due to the finite number of galaxies:

$$C^{\kappa}_{ij}(\ell) \to C^{\kappa}_{ij}(\ell) + \frac{\sigma^2_{\epsilon} n_{\rm bin}}{\bar{n}} \delta_{ij} \, , \tag{3.30}$$

where σ^2_{ϵ} is the intrinsic ellipticity dispersion, $n_{\rm bin}$ the number of tomographic bins and $\bar{n}$ the mean number of sources per steradian. Typical values are $\sigma_{\epsilon} = 0.3$, $\bar{n} = 30$ arcmin^{-2} and $n_{\rm bin} = 6$. Figure 3.2 shows the cosmic shear spectra from Eq. (3.30) for a *Euclid* like survey. Clearly tomographic bins at higher redshifts obtain a higher lensing signal, since the photons pass through more LSS. Furthermore, one clearly sees how the shot noise term for the auto-correlation dominates at high multipoles. At a multipole $\ell \approx 300$ non-linear clustering sets in, which can be seen by the small bump present in the power spectrum. For linear clustering the power spectrum would drop at high ℓ.

3.2.2 *Weak gravitational lensing of the CMB*

The photons of the CMB, as discussed in Section 3.1, travel through the LSS with potential depths of the order of $|\Phi|/c^2 \approx 10^{-5}$ leading to deflection angle of $|\alpha| \approx 10^{-4}$ (Cole and Efstathiou, 1989; Seljak, 1996; Hu, 2000). Potential wells in the LSS have a diameter of a few hundred Mpc and the distance to the last scattering surface $\chi(z_*)$, where $z_* \approx 1100$ is roughly 14 Gpc. Therefore the scattering of the deflection angle is roughly two arcminutes. These deflection angles will be correlated over the size of a typical potential well, which is roughly two degrees on the sky, meaning that their correlation length is similar to the one of the acoustic peaks meaning that the BAO features get washed out slightly.

The theoretical prediction for the lensing potential or the convergence and its power spectrum proceeds in complete analogy to cosmic shear with a single source placed at the last scattering surface, i.e. we replace $p(\chi)$ by a delta distribution $\delta_D(\chi - \chi_*)$ in the weight function of (3.26) to get the convergence. Similarly the power spectrum is simply computed to be

$$C^{\kappa_{CMB}}(\ell) = \int \frac{d\chi}{\chi^2} W_{CMB}(\chi) W_{CMB}(\chi) P(\ell/\chi, \chi) \,, \tag{3.31}$$

with the mentioned weighting function W_{CMB}. Calculating the lensed temperature and polarization spectra of the CMB is a bit more involved. One can use a series expansion of the deflection angle to derive the lensed spectra, but also non-perturbative approaches (Seljak, 1996; Metcalf and Silk, 1997) exist. Lensing effectively re-arranges the temperature patches Θ according to:

$$\begin{aligned} \tilde{\Theta}(\mathbf{x}) &= \Theta(\mathbf{x}') = \Theta(\mathbf{x} + \boldsymbol{\nabla}\psi) \\ &\approx \Theta(\mathbf{x}) + \boldsymbol{\nabla}\psi(\mathbf{x}) \cdot \boldsymbol{\nabla}\Theta(\mathbf{x}) + \frac{1}{2} \mathrm{tr}\left[(\boldsymbol{\nabla}\psi \otimes \boldsymbol{\nabla}\psi)(\boldsymbol{\nabla} \otimes \boldsymbol{\nabla}\Theta)^T \right] + \dots \end{aligned} \tag{3.32}$$

Which can be used to calculate the lensed temperature power spectrum in terms of the unlensed one:

$$\tilde{C}_\ell^{\Theta\Theta} \approx (1 - \ell^2 R^\Psi) C_\ell^\Theta + \int \frac{d^2\ell'}{(2\pi)^2} [\ell' \cdot (\ell - \ell')]^2 C^\psi_{|\ell - \ell'|} C_{\ell'}^{\Theta\Theta} \,, \tag{3.33}$$

where C_ℓ^ψ is the power spectrum of the lensing potential, which is related to (3.31) by the Poisson equation $\Delta\psi = 2\kappa$. Furthermore we defined the averaged deflection angle

$$R^\psi = \frac{1}{4\pi} \int d\ell \, \ell^3 C_\ell^\psi \,. \tag{3.34}$$

The second term in Eq. (3.33) is a convolution of the unlensed spectrum with the spectrum of the lensing potential, smoothing out the temperature anisotropies. There are two important limits where one can investigate this result: On the one hand on very large scales, i.e. small ℓ, where the spectrum is nearly scale invariant, the effect of lensing will not be present. Clearly if the field is homogeneous, shuffling patches around by lensing will not yield any effect. On the other hand for very small scales the power in the unlensed spectrum is very weak due to Silk damping, therefore the Taylor expansion in (3.32) is again valid, even though the lensing effect would be

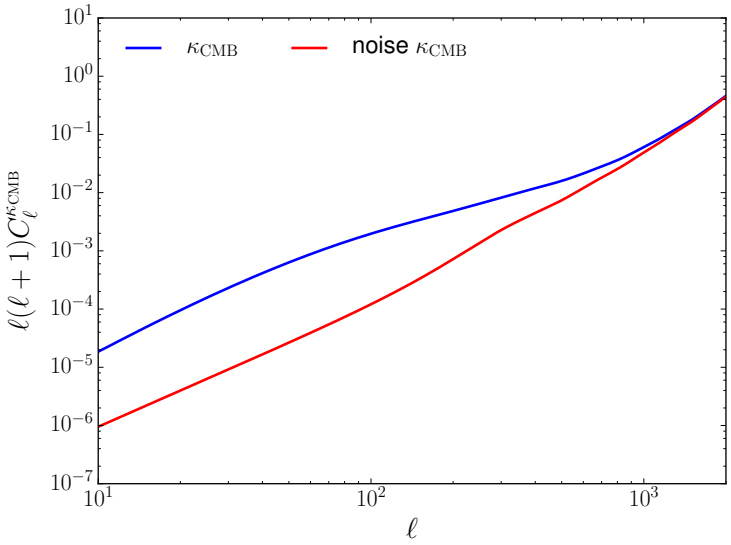

Figure 3.3: Power spectrum of the CMB lensing convergence including noise (blue curve). The red curve shows the noise contribution.

large in principle. Lensing of the polarization spectrum proceeds in a very similar way and we will refer to Lewis and Challinor (2006) for a detailed review.

Measuring the lensing potential itself is done by using the estimated spectra of the CMB primaries. Since the unlensed CMB is very well understood theoretically and the characteristic pattern of the lensing effect, it is possible to reconstruct the lensing potential directly from the measured power spectra (Hu, 2001; Hu and Okamoto, 2002). Especially on small scales the lensing effect can be measured directly. The basic idea of these methods is that the ℓ modes of the unlensed CMB are independent. This property is destroyed by lensing and therefore one can use the off-diagonal elements of $\langle\tilde{\Theta}(\ell)\tilde{\Theta}(\ell')\rangle$ for fixed ψ to estimate the lensing potential (Hu, 2001; Hu and Okamoto, 2002; Cooray and Kesden, 2003). The lensing potential can then be reconstructed and its noise properties determined by the cosmic variance of the different spectra, the finite number of available modes as well as observational effects. In Figure 3.3 we show the CMB lensing spectrum together with the noise obtained by the quadratic estimator from Hu and Okamoto (2002). Clearly the noise becomes important already below $\ell = 1000$, thus most of the signal will originate from linear scales at low multipoles.

3.3 GALAXY CLUSTERING

A very direct probe of the LSS are galaxy counts, i.e, measuring the density contrast δ in terms of the density of galaxies δ_g. The basic goal here is to directly measure the matter power spectrum (Groth and Peebles, 1977; Baumgart and Fry, 1991; Feldman et al., 1994) from galaxy clustering and to decompose it into spherical harmonics in radial shells (e.g. Heavens and Taylor, 1995; Di Dio et al., 2016; Raccanelli et al.,

2016). The logic is therefore very similar to a cosmic shear analysis and we consider the projected tomographic power spectrum:

$$C_{ij}^{g}(\ell) = \int_0^{\chi_H} \frac{d\chi}{\chi^2} W_{g_i}(\chi) W_{g_j}(\chi) P(\ell/\chi, \chi) \,, \tag{3.35}$$

with a suitable weighting function $W_{g_i}(\chi)$ in the i-th tomographic bin. Being in principle a very clean probe of the underlying cosmological model, galaxy counts defined via

$$\delta_g := \frac{n_g(\mathbf{x}) - \langle n_g \rangle}{\langle n_g \rangle} \,, \tag{3.36}$$

are a biased probe of the underlying matter distribution. Since galaxy formation itself is a very complicated process and depends strongly on the environment the galaxy density δ_g will in full generality be a complicated function of scale and space:

$$\delta_g(\mathbf{x}, a) = b(a, \mathbf{x}) \delta(\mathbf{x}, a) \,. \tag{3.37}$$

On large, linear scales this relation can however be very simple and just depend on time rather than on the scale k. If one proceeds to even smaller scales, more involved

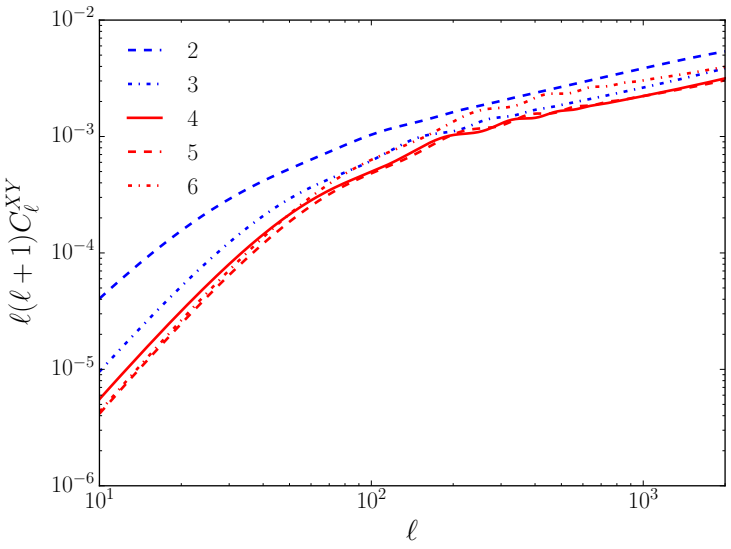

Figure 3.4: Galaxy clustering power spectrum for five different redshift bins. Note that in our approximation the cross-correlation between different tomographic bins vanishes since the weight functions do not overlap. Furthermore the shown spectra include the Poissonian noise term.

models have to be considered in order to match the relation between the matter power spectrum and the observed galaxy power spectrum. The basic idea of galaxy bias is to introduce operators $\mathcal{O}$ in a series expansion:

$$\delta_g(\mathbf{x}, a) = \sum_{\mathcal{O}} b_{\mathcal{O}}(a) \mathcal{O}(\mathbf{x}, a) \,, \tag{3.38}$$

where $b_{\mathcal{O}}(a)$ are called bias parameters and $\mathcal{O}$ are operators which are constructed from the density field, the gravitational potential and related random fields. Therefore the galaxy density δ_g is related to the matter density δ in a non-linear way. Figure 3.4 shows galaxy clustering power spectrum in different tomographic bins. Note that the number density in all bins is equal.

4

A LIE BASIS FOR THE VARIATION OF COSMIC LARGE-SCALE STRUCTURE COVARIANCE MATRICES

Statistical inference involves calculations of the likelihood as a function of the data and the model parameters. The inference process itself is usually carried out using MCMC methods, while forecasting is often done with a Fisher matrix approach, which approximates the posterior around the maximum likelihood estimator (MLE) point by a Gaussian distribution. Being asymptotically unbiased the MLE yields the true underlying model when averaging over all possible data. However, the signal strength of the measurement, as well as the model non-linearities depend on this true value. The errors obtained by a measurement therefore depend on the underlying model and its parameters. Those variations need to be studied. An even more severe situation occurs when reconstructing the power spectrum from cosmological random fields such as the weak cosmic shear signal. While all modes evolve independently during linear structure formation, non-linear growth will couple different modes in such a way that they are no longer statistically independent. This manifests itself in a non-vanishing tri-spectrum of the underlying random field. Since correlations between different modes now exist, they need to be incorporated correctly into the inference process. The covariance between different modes is, however, only accessible via numerical N-body simulations, which must span a huge dynamical range in order to keep up with future surveys. They also need to be known precisely enough and thus the covariance has to be deduced by a set of simulations at every point in parameter space (Sellentin and Heavens, 2016). With a typical MCMC usually containing of the order of 10^5 likelihood evaluations, the amount of needed computer time becomes unbearable. It is therefore necessary to find a good sampling of parameter space with simulations, which is both precise and computationally feasible.

We describe the change of the matter covariance and of the weak lensing covariance matrix as a function of cosmological parameters by constructing a suitable basis, where we model the contribution to the covariance from non-linear structure formation using Eulerian perturbation theory at third order. Our formalism is capable of dealing with large matrices and reproduces expected degeneracies and scaling with cosmological parameters in a reliable way. Comparing our analytical results to numerical simulations we find that the method describes the variation of the covariance matrix found in the SUNGLASS weak lensing simulation pipeline within the errors at one-loop and tree-level for the spectrum and the trispectrum, respectively, for multipoles up to 1300. We show that it is possible to optimize the sampling of parameter space where numerical simulations should be carried out by minimising interpolation errors and propose a corresponding method to distribute points in parameter space in an economical way.

The contents of this chapter is published in Reischke et al. (2017), while some ideas are also published in Schäfer and Reischke (2016).

4.1 INTRODUCTION

Measurements of cosmological parameters and investigations into the properties of gravity on large scales are the focus of a number of upcoming surveys of the cosmic large-scale structure. These investigations require probing how the expansion dynamics of the Universe and the gravitational model affect the growth rate of structures, as well as understanding the relation between redshift and distance. A tool combining both these sources of cosmological information is weak gravitational lensing (e.g. Kaiser, 1998; Bacon et al., 2000; Kaiser et al., 2000; Maoli et al., 2000; Mellier et al., 2000; Bartelmann and Schneider, 2001; Kilbinger, 2003) which, as a line-of-sight integrated quantity of the Newtonian tidal shear field, probes both structure growth and the evolution of the background cosmology by measuring a correlation in the shapes of galaxies.

The estimation of cosmological parameters based on large-scale structure observations requires a precise knowledge of the covariance matrix, which describes the cosmic variance, the statistical dependence of the modes of the cosmic matter distribution, and the noise inherent in the surveys. Due to mode coupling in non-linear structure formation the covariance matrix is non-diagonal, acquires large amplitudes on small scales, and renders the statistical properties of the cosmic matter distribution non-Gaussian; In this respect cosmological large-scale structure observations differ significantly from observations of primary covariance matrix-fluctuations (Komatsu et al., 2011), where the assumption of Gaussian statistics is very good.

The scaling of non-linear structure growth with cosmological parameters is necessarily non-linear, which is immediately apparent in all perturbative approaches to cosmic structure formation (Bernardeau, 1994; Bernardeau and Kofman, 1994; Taruya et al., 2002). Each order of perturbation theory is characterised by a different dependence on cosmology, and in assembling a perturbation series these dependences are mixed by superposition. Mode coupling in non-linear structure formation generates off-diagonal entries in the covariance matrix (e.g. Scoccimarro et al., 1999; Cooray and Hu, 2001; Takada and Bridle, 2007; Takada and Jain, 2009; Sato et al., 2009; Kayo et al., 2012, etc.) and therefore reduces the information content of the density field (e.g. Hu and Kravtsov, 2003; Takada and Bridle, 2007; Sato et al., 2009; Sato et al., 2011). On the other hand, fluctuations in the cosmic density field are strongly amplified by non-linear structure formation, which allows measurements on small scales which are otherwise inaccessible due to the sparsity of galaxies. Future experiments such as the Euclid mission[1] (Laureijs et al., 2011) will use the weak gravitational lensing effect to probe the cosmic web on scales deep in the non-linear regime (e.g. Benjamin et al., 2007; Laureijs et al., 2011; Van Waerbeke et al., 2013; Kitching et al., 2014). In fact, Euclid's anticipated weak lensing signal, with a significance of close to 1000σ, is largely generated by non-linear scales.

Because non-linear structure formation cannot yet be fully described by analytical methods, estimates of the covariance matrix require simulations of cosmic structure formation. Due to the large volume of future surveys and the necessity to observe at non-linear scales, cosmological simulations require both large volumes and high resolutions. In addition, a large suite of statistically equivalent simulations is required to estimate covariance matrices using ensemble-averaging. This estimation needs to

1 http://www.euclid-ec.org

be undertaken throughout the anticipated parameter space, because non-linear structure formation depends strongly on the choice of cosmological parameters.

Standard spatially flat dark energy cosmologies typically have six parameters. Thus, even a rather coarse sampling of parameter space would require a tremendous number of N-body ray-tracing simulations (Fosalba et al., 2008; Hilbert et al., 2009) or other techniques such as line-of-sight integrations (Kiessling et al., 2011), which are, up to now, the only robust method to determine the mode coupling and induced higher order cumulants to the desired accuracy. The computational load to produce large suites of simulations at Gpc-scales, while retaining resolution at sub-Mpc-scales, quickly becomes prohibitive. As a consequence, it is inevitable, that variations in the covariance matrices in parameter space are being investigated (Eifler et al., 2009) and a way to interpolate between these points must now be developed.

In this context a number of questions arise: (i) How strong are the variations of the covariance matrix with varying cosmological parameters? (ii) To which cosmological parameters is the covariance matrix most sensitive? (iii) Is there a way of predicting variations and in which directions in parameter space the strongest variations are encountered? (iv) Is it possible to decompose changes to the shape, size and orientation of the covariance matrix in a geometrically clear way? (v) What would be sensible choices of cosmological parameters for simulations in order to cover the relevant parameter space economically? (vi) Is there a natural way to interpolate between covariance matrices from numerical simulations?

Recently Schäfer and Reischke (2016) introduced a method to interpolate between Fisher matrices at different points in parameter space We now intend to apply this formalism to the variation of the covariance matrix of the matter and convergence power spectrum estimators. This should be possible because both Fisher-matrices and covariance matrices share positive-definiteness as a common property, which is required by our formalism. The focus will be on the power spectrum of the weak lensing convergence, as it is directly linked to observables provided by Euclid. Non-linear structure formation on small scales generates a non-Gaussian contribution to the covariance matrix, where we employ Eulerian perturbation theory at tree-level to predict the trispectrum as the lowest-order non-Gaussian contribution (Scoccimarro et al., 1999). We consider perturbation theory as an easily manageable tool for predicting non-linear corrections to the covariance matrix and do not imply that it describes all non-linearities accurately, but we will check its validity against numerical simulations.

The fiducial cosmological model is a spatially flat ΛCDM model with base parameters $\Omega_m = 0.3$, $\Omega_\Lambda = 1 - \Omega_m$, $h = 0.7$, $n_s = 1$, $w_0 = -1$ and $w_a = 0$. Moreover, we will use the sum convention throughout this chapter, thus implying summation over repeated indices. After a brief review of the lensing observables we will review the covariance matrix theory for the matter and convergence spectrum in Section 4.2. In Section 4.3 the Lie basis is constructed and applied to the covariance matrix in Section 4.4, where we also compare the theoretical prediction with simulations. In Section 4.5 we summarize.

4.2 COVARIANCE MATRICES

4.2.1 *Covariance matrix of the matter spectrum estimator*

We estimate the power spectrum $P(k)$, as defined in Eq. (2.15) with the Fourier convention (2.14) from a survey of finite volume V. Fitting a model to the power spectrum estimator involves the knowledge of the estimation error of the estimator $\hat{P}(k_i)$ in a certain k-bin. The estimation error consists of different pieces: firstly the density field used for $\hat{P}(k_i)$ will be sampled from a finite number of objects, e.g. galaxies, and will therefore suffer from Poissonian noise. Secondly, the estimated power spectrum will suffer from cosmic variance and thirdly, non-linear structure formation will lead to non-vanishing correlations between different k-bins.

The estimation proceed as follows: $P(k)$ can be estimated from a survey of volume V by dividing it into N spherical shells in Fourier-space with radii k_i and width Δk_i as the variance of all modes within a shell,

$$\hat{P}(k_i) = \frac{1}{V}\int_{k_i} \frac{d^3k}{V_s(k_i)}\,\delta(\mathbf{k})\delta(-\mathbf{k}), \tag{4.1}$$

where $V_s(k_i)$ is the volume of the ith shell. The Fourier-transform is Hermitean, $\delta(\mathbf{k}) = \delta(-\mathbf{k})^*$, because δ is real-valued.

The covariance matrix for the estimates $\hat{P}(k_i)$ is now given by

$$C^{\delta}_{ij} = \frac{1}{V}\left[\frac{(2\pi)^3}{V_s(k_i)} 2P^2(k_i)\delta_{ij} + \bar{T}_{ij}\right], \tag{4.2}$$

with a Gaussian, diagonal part, and a non-Gaussian contribution $\bar{T}_{ij}$,

$$\bar{T}_{ij} = \int_{k_i}\frac{d^3k_1}{V_s(k_i)}\int_{k_j}\frac{d^3k_2}{V_s(k_j)} T(\mathbf{k_1}, -\mathbf{k_1}, \mathbf{k_2}, -\mathbf{k_2}), \tag{4.3}$$

related to the matter trispectrum T which appears as the connected part of a 4-point correlation function that does not separate into squares of the matter spectrum if δ assumes non-Gaussian statistical properties. The emergence of non-Gaussian terms like the matter trispectrum can be approximated by perturbation theory and ultimately require simulations.

4.2.2 *Covariance matrix of the weak lensing spectrum*

We now play the same game again, but for the power spectrum of the weak lensing convergence from Eq. (3.30). In this case the projected trispectrum of the weak lensing convergence in tomographic bins m, n is given by

$$T^{\kappa}_{mn} = \int \frac{d\chi}{\chi^6}\, W^2_m(\chi) W^2_n(\chi)\, T(\ell_1/\chi, -\ell_1/\chi, \ell_2/\chi, -\ell_2/\chi), \tag{4.4}$$

where T^{κ}_{mn} is a function of the combination $(\ell_1, -\ell_1, \ell_2, -\ell_2)$ of wave vectors, which was omitted for shorthand notation.

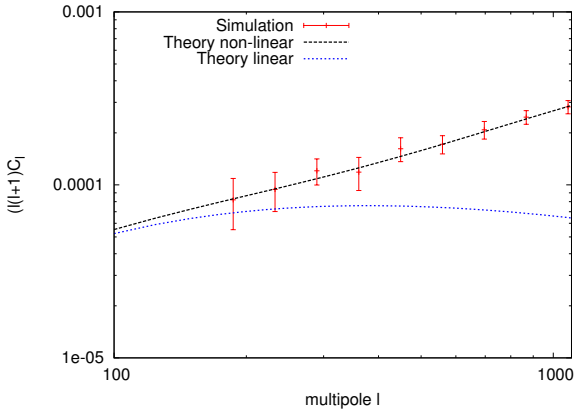

Figure 4.1: Comparison of the convergence power spectrum obtained from the simulation with the linear and non-linear theoretical prediction. The latter is obtained from the fitting formula described in . Note that the errors shown for the simulation are taken to be the diagonal parts of the covariance matrix. Therefore they are not uncorrelated.

The covariance of estimates $\hat{C}^{\kappa}_{mn}(\ell)$ of the tomographic weak lensing power spectra proceeds in complete analogy to the previous case: The solid angle Ω in Fourier-space is divided into N rings centred at the wave vectors ℓ_i, with width $\Delta\ell_i$ and volume $A_r(\ell_i)$. The covariance matrix of the estimates is then given by

$$C^{\kappa}_{ij,mn} = \frac{1}{\Omega}\left(2\,C^{\kappa}_{mn}(\ell_i)^2\frac{(2\pi)^2}{A_r(\ell_i)}\delta_{ij} + T^{\kappa}_{ij,mn}\right), \tag{4.5}$$

with the bin averaged convergence trispectrum, which has now indices i and j for the ℓ-bins, while m and n label the tomographic bins,

$$T^{\kappa}_{ij,mn} = \int_{\ell_i}\frac{d\ell_1}{A_r(\ell_i)}\int_{\ell_j}\frac{d\ell_2}{A_r(\ell_j)}T^{\kappa}_{mn}(\ell_1,-\ell_1,\ell_2,-\ell_2). \tag{4.6}$$

Here the diagonal elements contain, in principle, the shot noise term due to the finite number of background galaxies and their intrinsic ellipticity distribution. This term, however, does not depend on cosmology and is neglected in our analysis. Naturally, the covariance matrices will depend on the cosmological model and will undergo a transformation if a cosmological parameter assumes a new value; Effectively, we will require a set of transformation matrices for each direction of the parameter space, which is provided exactly by our formalism.

4.2.3 *Trispectrum at tree-level*

The covariance matrix is diagonal in the limit of linear structure formation which conserves the Gaussianity of the initial conditions and the independence of the Fourier-modes. In this case, the 4-point correlator arising in the expression for the covariance separates into squares of spectra by virtue of Wick's theorem. This is different in non-linear gravitational clustering, where mode coupling renders the statistical properties of the density field non-Gaussian and generates a trispectrum contribution to the covariance matrix. There exist various different approaches to non-linear

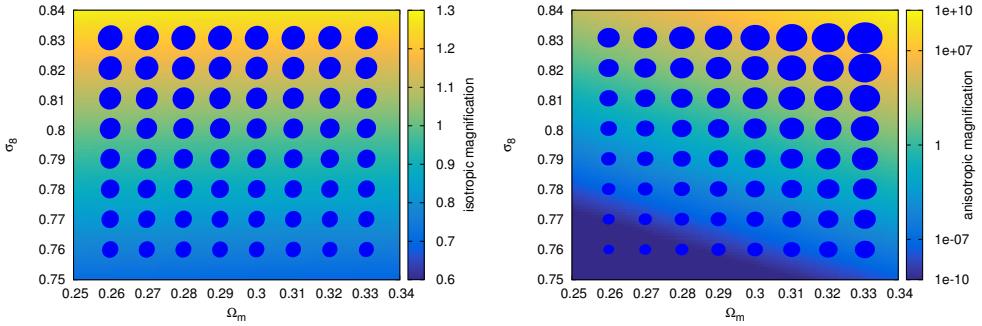

Figure 4.2: Variations of the matter spectrum covariance matrix in the $\Omega_m - \sigma_8$ plane. *Left*: We show the trace of the covariance matrix as isotropic magnification. Furthermore, we show the quadratic form induced by two k-bins as ellipses. The k-bin combination is $(k_1, k_2) = (0.19, 0.2)\ h\mathrm{Mpc}^{-1}$. *Right*: The determinant of the covariance matrix is shown as anisotropic magnification. k-bins are chosen to be $(k_N, k_{N-1}) = (0.8, 0.79)\ h\mathrm{Mpc}^{-1}$.

structure formation such as SPT, LPT or KFT, whose basics have been discussed in Section 2.2. Furthermore, there are more phenomenological models such as the halo model (Cooray and Sheth, 2002) or on the empirical log-normal distribution of the density field (Hilbert et al., 2011).

In this work we use SPT as a model for non-Gaussianities in structure formation, since the covariance matrix can be calculated rather easily and it does not depend on additional parameters such as, for example, the halo model. Thus the dependence on cosmological parameters, which we investigate here, enters directly into the perturbative expansion of the linear solution. We will use third-order perturbations at tree-level because it is an easily manageable model. In Sect. 4.4.3 we will show tests of the accuracy of the model against non-Gaussian lensing convergence maps derived from numerical simulations.

Eulerian perturbation theory, with perturbations of second and third order to the density and velocity fields, gives the trispectrum expression (Fry, 1984)

$$\begin{aligned} T(\mathbf{k}_1, \mathbf{k}_2, \mathbf{k}_3, \mathbf{k}_4) = 4\big[&F_2(\mathbf{k}_{12}, -\mathbf{k}_1) F_2(\mathbf{k}_{12}, \mathbf{k}_3) P_1 P_{12} P_3 \\ &+ \text{cycl.}\big] + 6\big[F_3(\mathbf{k}_1, \mathbf{k}_2, \mathbf{k}_3) P_1 P_2 P_3 + \text{cycl.}\big]\,, \end{aligned} \tag{4.7}$$

where we abbreviated $\mathbf{k}_{12} \equiv \mathbf{k}_1 + \mathbf{k}_2$, and $P_{\mathrm{lin}}(k_i) \equiv P_i$ is the linear power spectrum. The latter is given by the usual expression

$$P_{\mathrm{lin}}(k, a) = D_+^2(a) T^2(k) P_{\mathrm{ini}}(k), \tag{4.8}$$

where $D_+(a)$ is the normalized growth factor, $T(k)$ is the transfer function from Bardeen et al. (1986), and $P_{\mathrm{ini}}(k)$ is the initial power spectrum which is set by inflation to be proportional to k^{n_s} with the spectral index, n_s, being very close to unity. Evaluating the general expression for the configuration of the wave vectors needed in Eq. (4.4) yields

$$\begin{aligned} T(\mathbf{k}_1, -\mathbf{k}_1, \mathbf{k}_2, -\mathbf{k}_2) = {}& 12 F_3(\mathbf{k}_1, -\mathbf{k}_1, \mathbf{k}_2) P_1^2 P_2 \\ &+ 8 F_2^2(\mathbf{k}_1 - \mathbf{k}_2, \mathbf{k}_2) P(|\mathbf{k}_1 - \mathbf{k}_2|) P_2^2 \\ &+ 16 F_2(\mathbf{k}_1 - \mathbf{k}_2, \mathbf{k}_2) F_2(\mathbf{k}_2 - \mathbf{k}_1, \mathbf{k}_1) P_1 P_2 P(|\mathbf{k}_1 - \mathbf{k}_2|) \\ &+ (\mathbf{k}_1 \leftrightarrow \mathbf{k}_2), \end{aligned} \tag{4.9}$$

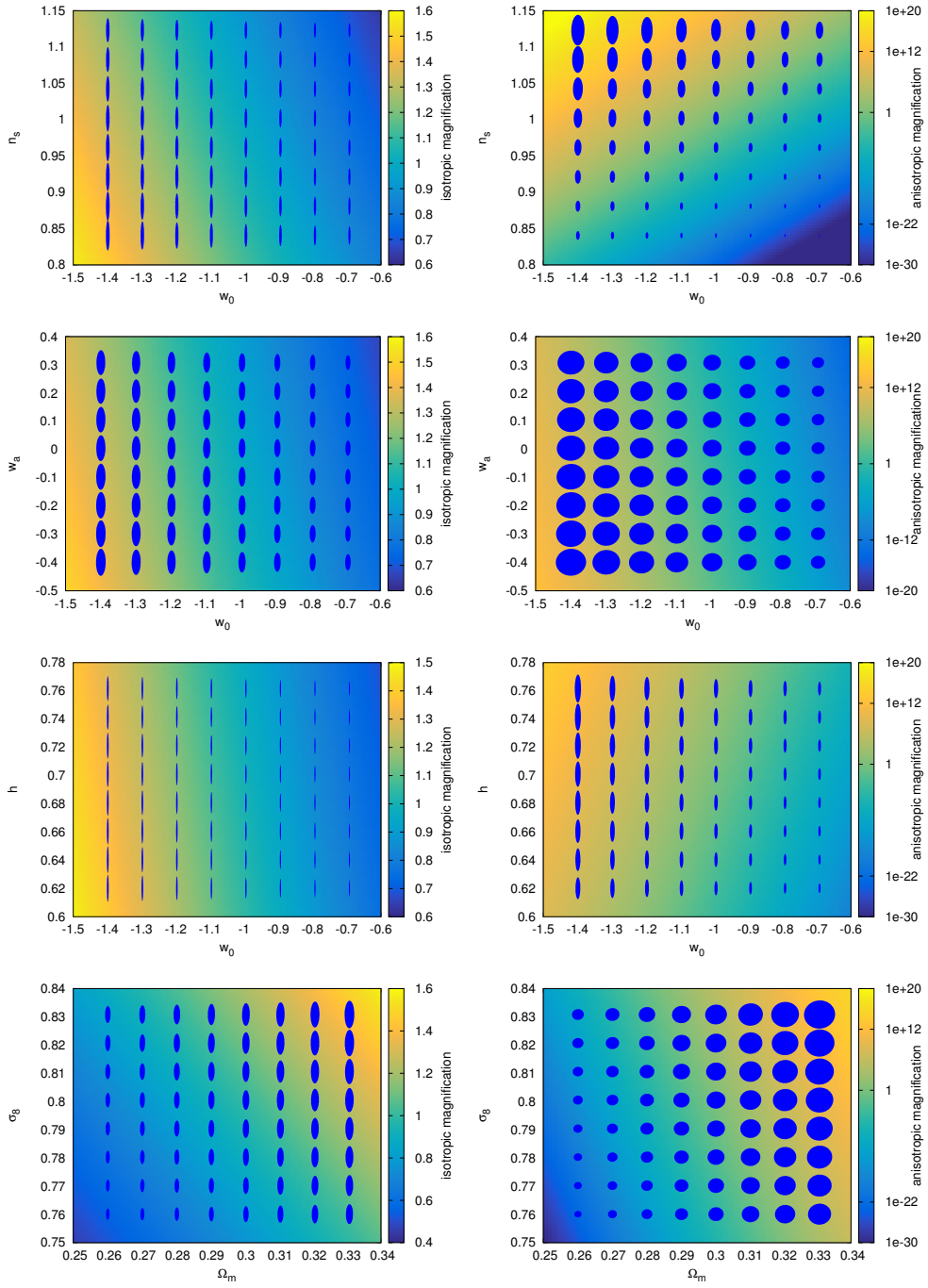

Figure 4.3: Variations of the convergence spectrum covariance matrix in the different parameter planes. *Left*: We show the trace of the covariance matrix as isotropic magnification. Furthermore we show the quadratic form induced by two ℓ-bins as ellipses. The ℓ-bin combination is $(\ell_1, \ell_2) = (100, 140)$. *Right*: The determinant of the covariance matrix is shown as anisotropic magnification. ℓ-bins are chosen to be $(\ell_N, \ell_{N-1}) = (2500, 2460)$.

where the symbol $(\mathbf{k}_1 \leftrightarrow \mathbf{k}_2)$ implies a repetition of the previous term with the wave vectors interchanged.

For practical calculations we note that the trispectrum is only a function of the magnitudes and the relative orientation of $\mathbf{k}_1$ and $\mathbf{k}_2$. In order to be consistent in perturbation theory we evaluate the Gaussian term in Eq. (4.2) at the one-loop level given by

$$P(k,t) = P_{\rm lin}(k,t) + P_{22}(k,t) + P_{13}(k,t), \tag{4.10}$$

where the two one-loop contributions can be written in terms of the linear spectrum $P_{\rm lin}$,

$$\begin{aligned} P_{22}(k,t) &= 2\int d^3q\ [F_2(\mathbf{k}-\mathbf{q},q)]^2\, P_{\rm lin}(|\mathbf{k}-\mathbf{q}|,t)P_{\rm lin}(q,t),\\ P_{13}(k,t) &= 6\int d^3q\, F_3(\mathbf{k},\mathbf{q},-\mathbf{q})P_{\rm lin}(k,t)P_{\rm lin}(q,t). \end{aligned} \tag{4.11}$$

Here it should be noted that although the contributions to the spectrum grow homogeneous in time for each order separately, their linear combination does not because the growth rates of each term are different.

4.2.4 *Simulations*

To estimate the variations of the covariance matrix in comparison to our perturbative model we use simulations generated using the SUNGLASS weak lensing simulation pipeline (Kiessling et al., 2011), which we will briefly summarize here. The pipeline uses the GADGET2 (Springel, 2005) N-body code to generate non-linearly evolved cosmic density fields. Specifically, the simulations assume a ΛCDM cosmology and comprise 512^3 particles in a simulation box with a side length of $512h^{-1}$Mpc. Weak lensing shear and convergence maps are derived from simulation snap-shots by carrying out light-of-sight integrations of tidal shear fields under the Born-approximation. These simulated weak lensing light cones cover a solid angle of 100 square degrees with a depth of $0 \leqslant z \leqslant 2$ in redshift (Kiessling et al., 2011). The light-cones have a *Euclid*-like source redshift distribution as in Eq. (3.28). In Figure 4.1 we show the convergence power spectrum obtained from the simulation together with the non-linear Smith et al. (2003) and the linear power spectrum. The binning which was chosen for the power spectrum will also be used in Sect. 4.4.3. Clearly we are dealing with scales which reach deep into the non-linear regime.

Statistically equivalent simulations for a range of choices of $\Omega_{\rm mo}$ and σ_8 are available, summarised by Table 1, which allows the determination of weak lensing covariances as an ensemble average over the weak lensing spectra derived from each simulated map. Averaging over all realizations of each parameter set allows to calculate the covariance of the spectrum estimator via

$$C^\kappa_{mn} = \left\langle \left(C^\kappa(\ell_m) - \hat{C}^\kappa(\ell_m)\right)\left(C^\kappa(\ell_n) - \hat{C}^\kappa(\ell_n)\right)\right\rangle\ , \tag{4.12}$$

where $\hat{C}^\kappa(\ell_m)$ is the estimated spectrum averaged over all realizations in an unbiased way, i.e. we include the $N-1$ in the denominator as the average power spectrum is estimated from the realizations as well.

Table 1: Cosmological parameters and the number of realizations of the simulations suite produced with the SUNGLASS pipeline.

Ω_{mo}	Ω_Λ	Ω_b	h	σ_8	n_s	N_{real}
0.272	0.728	0.0449	0.71	0.809	1	50
0.272	0.728	0.0449	0.71	0.728	1	50
0.272	0.728	0.0449	0.71	0.890	1	50
0.299	0.701	0.0449	0.71	0.809	1	50
0.245	0.755	0.0449	0.71	0.809	1	50

4.3 LIE BASIS

The covariance matrix depends strongly on the choice of the cosmological model; As a quantity involving second powers of spectra in the linear regime and third powers of the spectra in the perturbative non-linear regime, it scales $\propto \sigma_8^{4\cdots6}$. The proportionality of the weak lensing signal with Ω_m generates a dependence $\propto \Omega_m^4$ and the exact shape of the spectra encapsulated in n_s and h matters due to the mode coupling which determines the superposition of spectra in the expression for the trispectrum. In addition, the weak lensing effect depends on the dark energy properties through the relation between redshift and comoving distance as well as on the amplitude of cosmic structures as a function of distance or redshift. Furthermore, there are degeneracies between the parameters and situations where different parameter choices result in very similar covariance matrices. In summary, small changes in these physical properties account for a variation of the covariance matrix, which illustrates the necessity of accurate models.

Estimates of the covariance matrix require suites of cosmological simulations to be run throughout the expected parameter space, but coverage with a fine grid quickly becomes unfeasible given the dimensionality of basic wCDM-models. However, given an understanding of the variations of the covariance matrix, one could distribute the simulations in an economic way by identifying directions of rapid changes of the covariance matrix while sampling the parameter space only sparsely in directions with parameter degeneracies. The starting point of such a description of the variations of the covariance matrix is the construction of a basis, which determines the rate of change with each cosmological parameter.

We follow the procedure outlined in Schäfer and Reischke (2016) describing the change of the covariance matrix C_{ij}^κ at some fiducial model x_α to another point in parameter space x'_α by the action of a linear transformation U_{ij}

$$C'_{ij} \equiv C_{ij}(x'_\alpha) = U_{ik} C_{km}(x_\alpha) U_{mj}, \quad i,j = 1,...,N\,, \tag{4.13}$$

with the dimensionality N of the covariance matrix, i.e. the number of k- or ℓ-bins, which are indexed by i and j in the above formula. For simplicity, we revert to a non-tomographic weak lensing measurement; However, in principle, the tomographic weak lensing spectra would only add a technical complication to the formalism.

We construct the transformation by drawing the matrix root (i.e. the Cholesky decomposition of U_{ij}) $C_{ij}(x'_\alpha) = B_{ik}B_{kj}$ and identifying identical pairs. Then,

$$U_{ij} = B_{il}(B^{-1})_{lj} \,. \tag{4.14}$$

For an infinitesimal displacement $\delta x_\alpha \equiv x'_\alpha - x_\alpha$ the infinitesimal transformation takes the usual form

$$U_{ij} = \delta_{ij} + (x'_\alpha - x_\alpha)T_{ij\alpha}, \quad l = 1 \dots M \,, \tag{4.15}$$

with $T_{ij\alpha}$ being the generators of the transformation. Note that $T_{ij\alpha}$ is a collection of M matrices, i.e. one $N \times N$ matrix for every parameter direction. This is very similar to the action of the connection coefficients in general relativity. $T_{ij\alpha}$ is given by differentiation

$$T_{ij\alpha} = \partial_\alpha U_{ij} \,. \tag{4.16}$$

Multiple actions of the infinitesimal transformation lead in the limit to the global transformation, which is the usual matrix exponential

$$U_{ij} = \exp\left((x'_\alpha - x_\alpha)T_{ij\alpha}\right) \,. \tag{4.17}$$

Approximating this up to linear order in $x'_\alpha - x_\alpha$ yields

$$U_{ij} = \delta_{ij} + (x'_\alpha - x_\alpha)T_{ij\alpha} \,, \tag{4.18}$$

similar to the infinitesimal transformation before. Note that with this approximation the transformations in different parameter directions commute. Numerically, the generators are derived using finite differencing of U_{ij}

$$T_{ij\alpha} = \frac{U_{ij}(x_\alpha + \Delta x_\alpha) - U_{ij}(x_\alpha - \Delta x_\alpha)}{2\Delta x_\alpha} \,. \tag{4.19}$$

In this way it is possible to describe the transformation of the covariance matrix C_{ij} between $\mathbf{x}_\alpha$ and $\mathbf{x}'_\alpha$, and to decompose the transformation U_{ik} in terms of geometrically easy to interpret modes.

4.4 VARIATIONS OF THE COVARIANCE MATRICES

4.4.1 *Matter spectrum covariance*

As a proof of concept we calculate the covariance matrix in $N = 60$ equidistant k-bins of width $\Delta k \approx 0.01\,h\mathrm{Mpc}^{-1}$ with $k_1 \equiv k_{\min} = 0.19\,h\mathrm{Mpc}^{-1}$ and $k_N \equiv k_{\max} = 0.8\,h\mathrm{Mpc}^{-1}$. We take the survey volume to be unity as it only yields an overall factor. The covariance matrix is calculated at the fiducial model and at two other points in parameter space for each parameter direction. The variation Δx_α for the finite differencing in Eq. (4.19) is chosen to be 0.01 for σ_8 and Ω_m. We show the change of the covariance matrix using the trace, the determinant, and by picking out pairs of k-bins, which give rise to a quadratic form which can be represented as an ellipse.

The trace quantifies the isotropic magnification (relative to the fiducial model) of the covariance matrix because the off-diagonal elements do not enter. Conversely, the

determinant quantifies the anisotropic magnification due to the fact that the value of the determinant depends on the magnitude of the off-diagonal elements in relation to the diagonal elements. Because the magnitude of the off-diagonal elements is bounded by the geometric mean of the corresponding diagonal elements as a consequence of the Cauchy-Schwarz inequality, large correlation coefficients describe strong degeneracies and therefore strong anisotropic magnification.

Figure 4.2 shows the trace and determinant of the submatrix of the matter spectrum covariance as measures of isotropic and anisotropic magnification. It can be seen that changes in the traces are mainly due to σ_8 which is expected as it is mainly a rescaling of the elements of the covariance matrix. Note that the scaling with σ_8 seems rather obvious on first sight, however this simple scaling gets destroyed by the trispectrum entering in the expression for the covariance matrix, which, at tree-level, contains different powers of P. Nonetheless the leading order scaling of the power spectrum is dominant in the overall scaling of the covariance matrix. The dependence of the trace on Ω_m is weaker because the matter content influences the shape of the matter spectrum but not the amplitude. In contrast, the determinant shows a degeneracy between Ω_m and σ_8, which is due to the fact that an increasing Ω_m shifts the peak of the spectrum to higher k values, thus the mode coupling terms in the trispectrum include different values at different values of k.

Blue ellipses indicate the magnitude and the correlation coefficient of the covariance matrix in two different k bins. In the left plot we show the covariance matrix for the wave vector pair (k_1, k_2) while the right plot shows the covariance matrix for the pair (k_{N-1}, k_N). Clearly the behaviour of the ellipses follows the behaviour of the magnifications. This also shows that at low k the shape of the covariance matrix is dominated by σ_8 and quantifies linearly evolving scales due to the near diagonality, while at higher k also the off-diagonal elements become important as a consequence of non-linear structure formation.

4.4.2 *Convergence spectrum covariance*

We apply our technique to the covariance of the convergence spectrum, Eq. (4.5). As the convergence is a line-of-sight integral it will carry more information about the evolution of the Universe namely via the growth of structures and the geometrical evolution which both enter into Eq. (4.5); In particular we expect a much stronger variation of the weak lensing covariance matrix with the matter density Ω_m. Technically, we use $N = 60$ equidistant ℓ-bins with width $\Delta\ell = 40$ and in the range from $\ell_1 = 100$ to $\ell_N = 2500$. Furthermore, we assume a source redshift distribution with a mean redshift of 0.9, which would correspond to Euclid's anticipated redshift distribution. Since the redshift bins are summed over for each ℓ in the likelihood we only use one redshift bin.

Figure 4.3 shows the variation of the covariance matrix in parameter space, spanned by Ω_m, σ_8, h, n_s and the two dark energy parameters w_0 and w_a. Specifically, we quantify the isotropic and anisotropic changes of the covariance matrix by means of the trace and the determinant of a submatrix taken at low and high multipoles as before.

In the (σ_8, Ω_m)-plane the isotropic magnification shows the usual degeneracy between these two parameters, because lensing is sensitive to the product of the two,

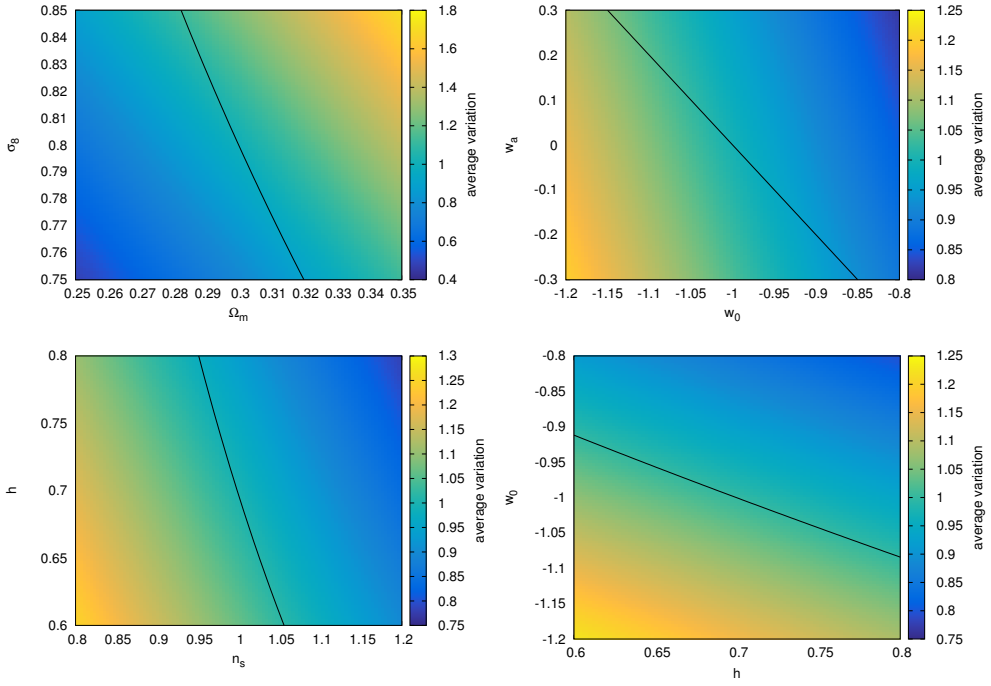

Figure 4.4: Average variation of each component of the covariance matrix calculated by the relative value of the Frobenius norm of C_{ij} with respect to the fiducial model. The black lines show the degeneracy of the frobenius norm along parameter space. In the (σ_8, Ω_m) plane the degeneracy corresponds roughly to $\sigma_8 \times \Omega_m = \text{const}$. In the (w_a, w_0) plane the black line shows models with constant effective equation of state. For (h, n_s) and (w_0, h) we used fits of the form $h n_s^a = \text{const}$. and $w h^b = \text{const}$. respectively. We find $a \approx 2.75$ and $b \approx -0.6$. The covariance matrix is the same as in Figure 4.3.

to lowest order. As described before the anisotropic magnification shows an even stronger dependence on Ω_m due to different mode coupling contributions in the off-diagonal elements.

The (h, w_0)-plane shows that the diagonal part of the covariance matrix is hardly influenced by the Hubble constant as its influence on the matter spectrum and the growth factor is rather small. In contrast, the equation of state parameter w_0 strongly influences the growth of structures and the geometry. In particular a more negative value of w_0 increases structure growth at early times and increases the lensing efficiency, thus leading to larger values for the lensing covariance. For the anisotropic magnification the dependence changes slightly due to the modification of the spectrum which becomes important in the non-Gaussian part of the covariance matrix.

For the (w_0, w_a)-plane, we adopted a linear evolution for the equation of state $w(a) = w_0 + w_a(1 - a)$ (Chevallier and Polarski, 2001; Linder, 2006). There are significant degeneracies between the two parameters for dark energy. This is due to the fact that the lensing signal depends on the equation of state function $w(a)$ through a triple integral, so effectively only on the average equation of state parameter. This effect can be seen in the anisotropic and isotropic magnification, thus mode coupling as well as the Gaussian part of the covariance matrix contain the same degeneracy.

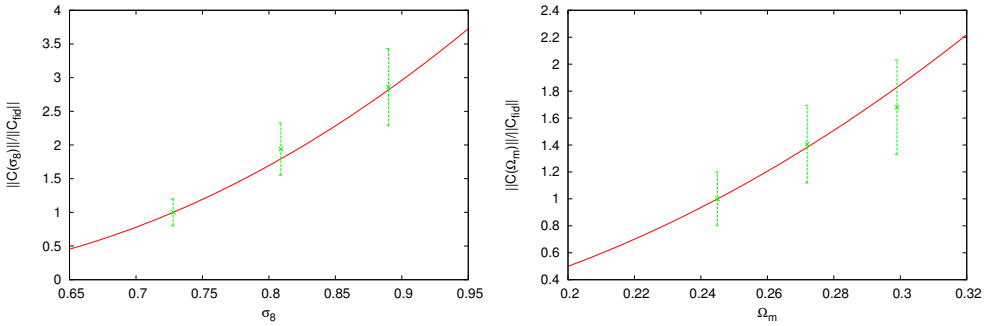

Figure 4.5: Theoretical prediction (red line) vs. simulation (green crosses with error bars) of the weak lensing covariance matrix as a function of σ_8 (left) and with Ω_m (right). We compute the Frobenius-norm of the full covariance matrix and normalise it to the norm at the fiducial values $\sigma_8 = 0.728$ and $\Omega_m = 0.245$. The error bars indicate the variance within the set of numerical simulations.

In order to get an intuition for the average change the covariance matrix while moving along parameter space we compare the Frobenius norm given by

$$\|C\| \equiv \sqrt{C_{ij}C_{ji}}, \tag{4.20}$$

relative to that of the fiducial cosmology. The ratio $\|C(x'_\alpha)\|/\|C(x_\alpha)\|$ corresponds to the relative change of the covariance matrix as a function of a cosmological parameter x_α. Nonetheless, it is clear that certain components of C will change more drastically when changing the cosmology than others. Figure 4.4 shows the average variation of the covariance matrix C along different parameter combinations. The black line indicates an expected or fitted degeneracy of C. As already mentioned before lensing is sensitive to the product of σ_8 and Ω_m, consequently the line plotted in the top left panel of Figure 4.4 has $\Omega_m \times \sigma_8 = \text{const}$ in the (Ω_m, σ_8) plane. Clearly the expectation is well represented in the colour plot. For the dark energy equation of state in the top right panel we plot a line where the effective equation of state is $w_{\text{eff}} = -1$, with

$$w_{\text{eff}} = \int_0^1 da\, w(a). \tag{4.21}$$

In contrast, there are no straightforward arguments for the degeneracies regarding (h, n_s) and (h, w_0). Therefore, we fit the degeneracy with a power law of the form $xy^a = \text{const}$ and interpret the results.

For (h, n_s) we obtain an exponent of roughly $a = 2.75$ with $hn_s^a = \text{const}$ which shows that the dependence on the spectral index is stronger than the dependence on the Hubble constant. Increasing h shifts the peak of the matter spectrum to higher k. Thus, the amplitude of the spectrum becomes smaller if σ_8 is kept fixed, and as a consequence the values of the covariance matrix become smaller. Finally, the (w_0, h) plane shows a degeneracy with $w_0 h^a = \text{const}$, with $a \approx -0.6$. If $w_0 > -1$ structure growth is decreased at early times, thus leading to smaller entries in the covariance matrix.

The analysis shows that the variation in the covariance matrix is strongest for the cosmological parameters responsible for structure formation. Relative changes

with respect to the fiducial model of roughly 80% can occur in these parameters in the range of parameter values considered. The amount of variation is reduced if one applies priors and restricts the allowed parameter space, for instance by using cosmic microwave background data (e.g. Planck Collaboration XIII, 2015).

It is important to note that we only kept terms linear in the generator. Of course one can also consider more terms in the expansion of the transformation matrix U_{ik} in Eq. (4.18), although one loses commutativity of the generators and has to keep track of this using the Baker-Campbell-Hausdorff formula (Schäfer and Reischke, 2016). However, if the changes of the covariance matrices are small enough, ~10%, this approximation is justified.

4.4.3 *Comparing the variation with simulations*

We use the weak lensing light-cones described in Section 4.2.4 to construct the spectrum of the convergence field κ in $N = 9$ logarithmically equidistant bins in the angular wave vector, between $\ell_{\min} = 186$ and $\ell_{\max} = 1345$. Lower multipoles will exhibit large fluctuations due to the size of the simulation volume, while higher multipoles contain a strong shot noise contribution and suffer from resolution limits. For more details we refer to Kiessling et al. (2011).

For each cosmological parameter set from Table 1 the covariance matrix is estimated as described in Eq. (4.12) from the available set of statistically equivalent simulations. Due to the relatively small number of realizations (see Table 1) the estimator for the covariance itself is rather noisy with a relative error of ~14% due to Poisson noise and convergence may not have been reached yet (for convergence of covariance matrix estimators we refer to Sellentin and Heavens, 2016; Petri et al., 2016). Therefore it is not useful to compare single components of the covariance matrix and instead we again compare the average change of the covariance matrix by means of the Frobenius norm, Eq. (4.20). Note that it would certainly be sensible to test the algorithm against a more robust estimate of the covariance matrix. This, however, would require significant computational resources since at least roughly $\sim 10^4$ simulations are needed at each point in parameter space to get a more reliable estimate of the covariance matrix with errors at the percent level.

Figure 4.5 shows the theoretical prediction compared with the simulation for the two parameters σ_8 and Ω_m. Clearly the theoretical prediction matches the simulation quite well for both parameters. By fixing a fiducial value we force the covariance matrix to agree at one point in parameter space. This, however, is not the case (at least in the non-linear regime), as it has been shown by various authors (e.g. Cooray and Hu, 2001) that the covariance matrix with a trispectrum correction from Eulerian perturbation theory underestimates the covariance in comparison to that found in numerical simulations. Nonetheless the results show that the scaling of the spectra, trispectra and covariances with cosmological parameters can be captured well perturbativly even at one-loop and tree-level, respectively, even though the absolute magnitude cannot be precisely calculated.

In order to analyze the variation of the covariance matrix more accurately, i.e. comparing single components of it, more realizations of the simulated convergence field are needed. Furthermore the theoretical part can be improved by adding more order in perturbation theory, using the halo model, or including additional terms

such as the halo sample variance (Cooray and Hu, 2001; Takada and Jain, 2004; Takada and Bridle, 2007; Takada and Jain, 2009; Sato et al., 2009; Kayo et al., 2012) as well as super sample covariance (Takada and Hu, 2013).

However, in this paper we intended to show that the covariance matrix exhibits variations across parameter space, which can be well captured via the linear mapping introduced in Eq. (4.13). It is therefore sufficient to keep the transformation matrix U up to linear order. Furthermore, this will also preserve the Abelian structure of the transformation group, as commutativity is destroyed when including non-linear terms in the transformation (Schäfer and Reischke, 2016). A similar question in this context is related to the validity of the linear approximation; Because the variation of the covariance matrix is captured well by the model we introduced in Section 4.2, we can compare the Frobenius norm of Lie approximated covariance matrix to the exactly calculated covariance matrix (at tree-level). As soon as the deviation becomes larger than some error threshold, which is given by the necessary accuracy for the covariance matrix, a new Lie basis should be constructed at this point. Alternatively the sampling of the parameter space can also be constructed on the level of the generators $T_{ij\alpha}$. For each direction, α, this describes an $N \times N$ matrix relating the covariance matrix at one parameter point to the covariance matrix at another parameter point. The matrix U_{ij} given in Eq. (4.18) is a good approximation for the transformation as long as the first term dominates over the higher order ones. This implies that a new Lie basis should be constructed in direction α at point x'_α as soon as $(x'_\alpha - x_\alpha)T_{ij\alpha} \approx 1$.

Figure 4.6 shows one example for the outlined procedure. The Frobenius norm of the covariance matrix stays constant along the black lines, while it changes by roughly 10% between neighbouring lines. The red dot marks the fiducial model and the blue ellipse indicates the marginalized priors from Planck Collaboration XIII (2015) on both parameters. The direction of strongest change in the weak lensing covariance matrix is clearly into the direction of larger Ω_m and larger σ_8, while in the orthogonal direction the weak lensing covariance matrix does not change due to the proportionality of the weak lensing signal to the product $\Omega_m \times \sigma_8$. Consequently, it is sufficient to evaluate the covariance matrix by generating suites of simulations sparsely along lines of constant $\Omega_m \times \sigma_8$, while perpendicularly to that the variation of the weak lensing covariance must be followed in finer detail.

From another point of view, the eigenvectors of the matrix $A_{\alpha\beta}$, given by

$$A_{\alpha\beta} = \partial^2_{\alpha\beta} \|C\|, \tag{4.22}$$

with parameter directions α and β, point into the degeneracy direction and perpendicular to it, while the magnitude of the eigenvalues corresponds to the amount of change in these directions. For the completely degenerate case, as in Figure 4.6, the eigenvalue of the eigenvector, which is parallel to the degeneracy lines, would have eigenvalue zero. Accordingly, the grid on which the covariance is sampled could be rotated into the principal frame of matrix A, reducing this two dimensional sampling problem into a one dimensional one with degeneracy direction roughly given by the constraint $\Omega_m \times \sigma_8 = \text{const}$. This procedure generalizes straightforwardly to higher dimensions.

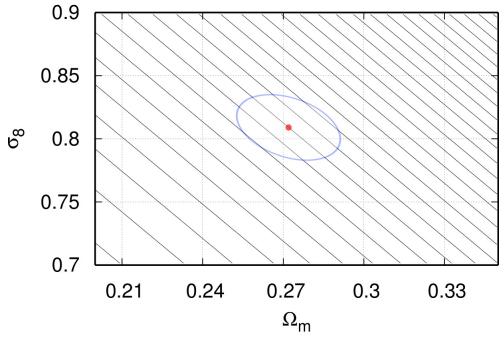

Figure 4.6: Average change of the covariance matrix estimated using the Frobenius norm. The covariance matrix stays constant along the black lines and changes by 10% from one black line to the other with respect to the fiducial model which is marked with a red dot. The blue ellipse indicates the approximate region of marginalized priors as found from covariance matrix measurements.

4.5 CONCLUSION

In this paper we investigated variations of the covariance matrix of cosmic large-scale structure observations, where non-linear structure formation processes generate non-Gaussian and non-diagonal contributions. We described the variation of the covariance matrix with a change of the cosmological model by constructing a basis, and considered as specific examples the matter density and weak lensing convergence power spectra. We worked with an analytical model for non-linear structure formation based on Eulerian perturbation theory and derived non-Gaussian contributions to the covariance matrices by evaluating the spectrum and the trispectrum in third order. This analytical model was juxtaposed with the results from numerical simulations. We summarize our principal results as follows:

1. The fundamental scaling of the analytical model with the parameters Ω_m and σ_8 was reproduced correctly in comparison to numerical simulations.

2. The covariance matrix of estimates of spectra depends on cosmological parameters, both in the linear and non-linear regime. We investigated the scaling of the covariance matrix with parameters from a *w*CDM-cosmology. By constructing a basis for the transformation which relates covariance matrices at different points in parameter space to each other we were able to predict the magnitude and degeneracies rather well, and were able to identify directions in parameter space associated with large changes in the covariance.

3. Our formalism was able to represent variations in the covariance matrix for a wide region of the parameter space. In fact, it could describe variations much larger than that allowed by current experiments like Planck. Furthermore, the formalism also captured degeneracy lines, i.e. parameter combinations along which the covariance matrices effectively remain constant, which we showed to have clear physical explanations.

4. The identification of directions in parameter space in which the largest variations of the covariance matrix occur allows for an economical sampling with

numerical simulations; This is feasible because our formalism effectively provides a metric which determines the distance in different directions in parameter space where the variation of the covariance matrix would be larger than a predefined threshold. Apart from predicting variations, our formalism is also well suited for inter- and extrapolation of covariance matrices which are ultimately determined from a large set of numerical simulations at discrete, specifically chosen, parameter points.

5

SPHERICAL COLLAPSE OF DARK MATTER HALOS IN TIDAL GRAVITATIONAL FIELDS

The statistics of the peaks in the random field of the LSS provides a complementary probe to the usual two-point or higher order statistics discussed in Chapter 3. In order to count peaks in a random field one needs two ingredients: the underlying distribution and an upcrossing threshold. The random field under consideration in cosmology is usually the density contrast, δ, Eq. (2.12). Its distribution function at early times is very well described by a Gaussian distribution due to cosmological inflation. However non-linear clustering drives the distribution function away from Gaussianity and it is known only empirically to be log-normal from N-body simulations (Kayo et al., 2001) at late times. A perturbative approach to describe the distribution would be the Edgeworth expansion (Juszkiewicz et al., 1995; Sellentin et al., 2017a) using the cumulants of the underlying distribution.

Another possibility is to describe the growth of structures in terms of a Gaussian random field, which is analytically much more feasible then for generic distributions. In order to keep the Gaussianity of the density contrast field one needs to restrict the treatment to linear evolution. To describe non-linear objects which form at peaks in the density field, i.e. galaxy groups and clusters, or even galaxies an extrapolation method from the non-linear to the linear regime must be given. The SPC model of dark matter halos serves as such a method by studying the formation of spherically symmetric virialized dark matter structures and by providing a linearly evolved density contrast $\delta_{\rm crit}$ at which a dark matter halo can be considered to have formed. In this chapter we will investigate the assumption that halos form in a uniform background by placing a test particle into a Gaussian random field and calculating the exerted tidal forces on it. We then solve the spherical collapse equation including the external forces, thus changing the collapse dynamic and therefore changing the value of $\delta_{\rm crit}$. Furthermore $\delta_{\rm crit}$ is now a random variable itself and will have a mass dependence due to the smoothing of the density contrast on different scales.

The contents of this chapter is published in Reischke et al. (2016b) and 2017, while some ideas are also published in Pace et al. (2017).

5.1 INTRODUCTION

A promising tool to reveal the time evolution of dark energy observationally is the halo mass function, which enters for example in cluster counts (Sunyaev and Zeldovich, 1980; Majumdar, 2004; Diego and Majumdar, 2004; Fang and Haiman, 2007; Abramo et al., 2009; Angrick and Bartelmann, 2009) or weak lensing peak counts (Maturi et al., 2010; Maturi et al., 2011; Lin and Kilbinger, 2014; Reischke et al., 2016a). The halo mass function deals with objects in the highly non-linear regime and therefore a method is needed to extrapolate the linearly evolved density to the non-linear one. This is usually done by using the spherical collapse model introduced by Gunn and Gott (1972) and later extended in several works (Fillmore and Goldreich, 1984; Bertschinger, 1985; Ryden and Gunn, 1987; Avila-Reese et al., 1998; Mota and van de Bruck, 2004; Abramo et al., 2007; Pace et al., 2010; 2014, a). The model assumes perturbations to be spherically symmetric non-rotating objects which decouple from the background expansion and thus reach a maximum point of expansion after which they collapse. In principle they would collapse to a single point. However, in reality the kinetic energy due to the collapse is converted into random motions of the particles in the over-dense regions, such that an equilibrium situation (in the sense of virialized structure, Schäfer and Koyama, 2008) is created. This model is, despite its simplicity, rather successful.

It is therefore important to get some insight into the theoretical assumptions of this model and to extend it towards more realistic situations. Especially rotation and shear effects are important extensions to the collapse model. Mainly rotational effects have been described in Pace et al. (2014b) which delay the collapse due to centrifugal forces, thus delaying the collapse of structures leading to a larger over-density needed for virialized structures. As the collapse model assumes a homogeneous sphere, shear effects are usually neglected, however, there can also be shear effects in homogeneous spheres and as real structures form in over-dense regions, there there will be shear effects due to external tidal fields. Those, if small enough, would not violate the symmetry assumptions of the model. External shear automatically leads to a mass dependence of the fundamental parameter of the spherical collapse, the critical over-density δ_c, as light and therefore smaller objects will feel higher fluctuations in the density field than heavy objects. In this paper we will investigate the influence of external shear effects and how it depends on the underlying cosmological model. To this end we calculate the shear directly from the underlying density field by using first order Lagrangian perturbation theory, i.e. the ZA (Zel'Dovich, 1970). We set up a random process to sample shear values from the statistics of the underlying density field and investigate how this affects the collapse on different scales. This procedure has the advantage that we do not need to rely on phenomenological models, as we can instead calculate the tidal shear from first principles as it is for example also done in angular momentum correlations of large scale structure due to tidal torquing (Schäfer, 2009).

Since the tidal field is described by a potential flow there is no vorticity generation. However, a rotation of the collapsing region can be modelled by a mechanism called tidal torquing (White, 1984; Catelan and Theuns, 1996; Crittenden et al., 2001; Schäfer, 2009; Schäfer and Merkel, 2012). We will therefore consider a peak in the density field with inertial tensor $\mathbf{I}$ and tidal shear tensor $\boldsymbol{\Psi}$ and investigate jointly the

induced shear and rotation. Assuming that halos form at peaks, we will use the values estimated for the shear and the rotation as input for the spherical collapse model leading to a self-consistent description of the spherical collapse in gravitational tidal fields. We will furthermore show that the restriction to peaks in the density field has some very general consequences on the induced rotation and shear.

The structure of this chapter is the following: We will review the SPC model in Section 5.2 and describe the sampling of the tidal shear field Section 5.3. In Section 5.4 we investigate the influence of the halo's mass at its environment and in Section 5.5 we discuss the influence on the collapse threshold in different dark energy scenarios. Section 5.6 and Section 5.7 describe the influence of the changed collapse threshold on the mass function, on counts of galaxy cluster and on parameter estimation. Finally in Section 5.8 we also investigate the influence of rotation on the collapse and conclude in Section 5.10.

5.2 THE SPHERICAL COLLAPSE MODEL

The SPC model has been discussed by various authors, e.g Bernardeau (1994); Padmanabhan (1996); Ohta et al. (2003); 2004; Abramo et al. (2007) and Pace et al. (2010); 2014, a. Here we start with the hydrodynamical equations

$$\begin{aligned} \dot{\delta} + (1+\delta)\nabla_x \mathbf{u} &= 0 \,, \\ \dot{\mathbf{u}} + 2H\mathbf{u} + (\mathbf{u}\cdot\nabla_x)\mathbf{u} &= -\frac{1}{a^2}\nabla_x \phi \,, \\ \nabla_x^2 \phi &= 4\pi G a^2 \rho_0 \delta \,, \end{aligned} \tag{5.1}$$

with comoving coordinate x, comoving peculiar velocity $\mathbf{u}$, Newtonian potential ϕ, overdensity δ and background density ρ_0. The dot represents a derivative with respect to cosmic time t. They can be obtained by projecting the relativistic energy-momentum conservation equation onto an observer and perpendicular to it. Taking the divergence of the Euler equation and inserting the Poisson equation yields

$$\begin{aligned} \dot{\delta} &= -(1+\delta)\theta \,, \\ \dot{\theta} &= -2H\theta - 4\pi G\rho_0\delta - \frac{1}{3}\theta^2 - (\sigma^2 - \omega^2) \,, \end{aligned} \tag{5.2}$$

where we used the decomposition

$$\nabla_x \cdot [(\mathbf{u}\cdot\nabla_x)\mathbf{u}] = \frac{1}{3}\theta^2 + \sigma^2 - \omega^2 \,, \tag{5.3}$$

with the expansion $\theta = \nabla_x \cdot \mathbf{u}$, the shear $\sigma^2 \equiv \sigma_{ij}\sigma^{ij}$ and the rotation $\omega^2 \equiv \omega_{ij}\omega^{ij}$. The rotation and the shear tensors are themselves the antisymmetric and the symmetric traceless part of the velocity divergence tensor, respectively. They are defined as

$$\begin{aligned} \sigma_{ij} &= \frac{1}{2}\left(\partial_i u_j + \partial_j u_i\right) - \frac{\theta}{3}\delta_{ij} \,, \\ \omega_{ij} &= \frac{1}{2}\left(\partial_i u_j - \partial_j u_i\right) \,, \end{aligned} \tag{5.4}$$

where $\partial_i \equiv \partial/\partial x^i$. We now use the relation $\partial_t = aH(a)\partial_a$ and $f \equiv 1/\delta$ which leads to

$$\begin{aligned} f' &= \frac{\theta}{aH} f(1+f) \,, \\ \theta' &= -\frac{2\theta}{a} - \frac{3H\Omega_m}{2af} - \left(\frac{1}{3}\theta^2 + \sigma^2 - \omega^2\right)\frac{1}{aH} \,. \end{aligned} \tag{5.5}$$

The system in Eq. (5.5) is solved numerically until $f \sim 10^{-14}$ and then it is extrapolated to zero. This yields the appropriate initial conditions for the linear evolution of the density contrast which gives δ_c. In the classical SPC model, σ^2 and ω^2 are neglected. However, their influence has been investigated by Del Popolo et al. (2013a) and b in the ΛCDM and dark energy cosmologies and by Pace et al., 2014b in clustering dark energy models. The authors employ a heuristic model for the term $\sigma^2 - \omega^2$ which allows to study an isolated collapse including a (mass dependent) quantity α, defined as the ratio between the rotational and the gravitational term. Quantitatively, the term is

$$\alpha = \frac{L^2}{M^3 R G} \,, \tag{5.6}$$

where L denotes the angular momentum of the spherical overdensity considered and M and R its mass and radius, respectively. The angular term is important for galaxies and negligible for massive clusters; in particular $\alpha \approx 0.05$ for $M \approx 10^{11}\ M_\odot\ h^{-1}$ and of the order of 10^{-6} for $M \approx 10^{15}\ M_\odot\ h^{-1}$. By defining the twiddled quantities $\tilde{\theta} = \theta/H$, $\tilde{\sigma} = \sigma/H$ and $\tilde{\omega} = \omega/H$, the combined contribution of the shear and rotation term can effectively be modelled by

$$\tilde{\sigma}^2 - \tilde{\omega}^2 = -\frac{3}{2}\alpha\Omega_m\delta \,, \tag{5.7}$$

leading to the modified Euler equation

$$\tilde{\theta}' + \left(\frac{2}{a} + \frac{H'}{H}\right)\tilde{\theta} + \frac{\tilde{\theta}^2}{3a} + \frac{3}{2a}(1-\alpha)\Omega_m\delta = 0 \,. \tag{5.8}$$

In the notation of this work, Eq. (5.8) reads

$$\tilde{\theta}' + \left(\frac{2}{a} + \frac{H'}{H}\right)\tilde{\theta} + \frac{\tilde{\theta}^2}{3a} + \frac{3}{2a}\frac{(1-\alpha)\Omega_m}{f} = 0 \,. \tag{5.9}$$

As shown by the authors, the effect of the term $\tilde{\sigma}^2 - \tilde{\omega}^2$ is to slow down the collapse and to decrease the number of objects. This effect is differential and depends on mass and on redshift. At high redshifts, modifications are small, while at low redshifts they are more substantial. In addition, we can appreciate the slowing of the collapse (now mass dependent) for low mass objects. In this work we follow a complementary approach. Instead of trying to model the additional non-linear term, we will derive only the shear contribution from the statistics of the density field in linear perturbation theory, since at early times velocities decay rapidly and vorticity is not sourced in the linear regime. Hence a direct comparison with the work by Del Popolo et al., 2013a; b; Pace et al., 2014b cannot be performed. Note, however that we can expect an opposite behaviour of the collapse, since it is well known (Angrick and Bartelmann, 2010) that the ellipsoidal collapse proceeds faster than the spherical collapse.

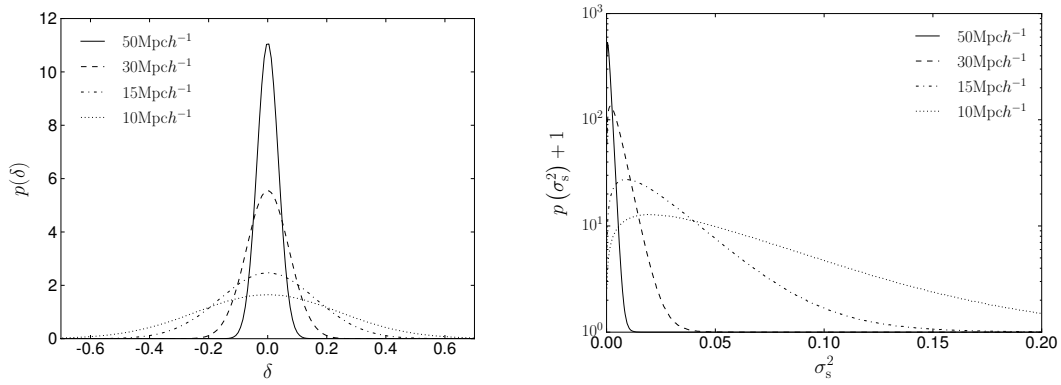

Figure 5.1: *Left*: Normalized distribution of the density contrast $\delta = \psi_{ii}$ for different length scales. Note that we show the distribution of σ_s^2 with an offset of unity on the right. Clearly the values for δ below $R \approx 10\,\mathrm{Mpc}h^{-1}$ would become too large in order to satisfy the assumption $\delta \ll 1$. *Right*: Normalized distribution of the tidal shear invariant σ_s^2 given in Eq. (5.12) for different length scales. Note that we show the distribution of σ_s^2 with an offset of unity.

5.3 SAMPLING TIDAL SHEAR VALUES

For the tidal shear we assume Zel'dovich velocities (Zel'Dovich, 1970), thus approximating the velocity field as a potential flow. For the trajectories one assumes

$$x_i = q_i - D_+(t)\partial_i\psi \equiv q_i - D_+(t)\psi_{,i}\,, \tag{5.10}$$

with the displacement field ψ which is related to the density contrast δ via a Poisson relation, $\Delta\psi = \delta$, the initial position q and the linear growth factor $D_+(t)$. The velocity is then given by

$$\dot{x}_i(t) = -\dot{D}_+(t)\psi_{,i} = -H\frac{d\ln D_+}{d\ln a}D_+\psi_{,i}\,. \tag{5.11}$$

Clearly there is no vorticity generated in this configuration, due to the permutability of the second derivatives. Thus the only remaining contribution to the spherical collapse is the traceless shear tensor

$$\sigma^2 \equiv \sigma_{ij}\sigma^{ij} = \dot{D}_+^2(t)\left(\psi_{,ij}\psi^{,ij} - \frac{1}{3}(\Delta\psi)^2\right) \equiv \dot{D}_+^2(t)\sigma_s^2\,, \tag{5.12}$$

with $\psi_{,ij} \equiv \partial_i\partial_j\psi$. In the last step the time evolution was separated from the constant shear σ_s^2. We now sample values for the shear, $\psi_{,ij}$ directly from the statistics of the underlying density field. To this end we transform to Fourier space and use Poisson's equation leading to

$$\psi_{,ij} = \int \frac{d^3k}{(2\pi)^3}\frac{k_ik_j}{k^2}\delta(\mathbf{k})\exp(i\mathbf{kx})\,. \tag{5.13}$$

However, the correlation between the density field and the tidal shear is complicated in these coordinates. Following Regős and Szalay (1995) and Heavens and Sheth (1999) we consider the density peaks symmetric about the origin on the z-axis and introduce dimensionless complex variables

$$y_{lm}^n = \sqrt{4\pi}\frac{i^{l+2n}}{\sigma_{l+2n}}\int \frac{d^3k}{(2\pi)^3}k^{l+2n}\delta(\mathbf{k})Y_{lm}(\hat{k})\exp(i\mathbf{kx})\,, \tag{5.14}$$

with the direction vector $\hat{k} = \mathbf{k}/k$ and σ_i being the spectral moments of the matter power spectrum

$$\sigma_i^2 = \frac{1}{2\pi^2}\int dk\, k^{2i+2} P(k), \tag{5.15}$$

while Y_{lm} are spherical harmonics. We obtain a linear relation (Schäfer and Merkel, 2012) between y^n_{lm} and the tidal shear values $\psi_{,ij}$

$$\begin{aligned}
\sigma_0 y^{-1}_{20} &= -\sqrt{\frac{5}{4}}\left(\psi_{,xx} + \psi_{,yy} - 2\psi_{,zz}\right) , \\
\sigma_0 y^{-1}_{2\pm1} &= -\sqrt{\frac{15}{2}}\left(\psi_{,xz} \pm i\psi_{,yz}\right) , \\
\sigma_0 y^{-1}_{2\pm2} &= \sqrt{\frac{15}{8}}\left(\psi_{,xx} - \psi_{,yy} \pm 2i\psi_{,xy}\right) , \\
\sigma_0 y^{0}_{00} &= \left(\psi_{,xx} + \psi_{,yy} + \psi_{,zz}\right) .
\end{aligned} \tag{5.16}$$

In particular, the covariance in this basis is trivial, since the auto-correlation matrix is diagonal in l and m:

$$\left\langle y^n_{lm}(\mathbf{x}) y^{n'}_{l'm'}(\mathbf{x})^* \right\rangle = (-1)^{n-n'} \frac{\sigma^2_{l+n+n'}}{\sigma_{l+2n}\sigma_{l+2n'}} \delta_{ll'}\delta_{mm'} . \tag{5.17}$$

Thus, in the y^n_{lm} basis the tidal shear values are uncorrelated Gaussian random variables with unit variance. We obtain the tidal shear values in physical coordinates by inverting the mapping

$$\sigma_0 \boldsymbol{\alpha} = M \boldsymbol{\psi} , \tag{5.18}$$

where the six dimensional vectors $\boldsymbol{\alpha}$ and $\boldsymbol{\psi}$ bundle the variables in spherical and physical coordinates from Eq. (5.16) respectively

$$\begin{aligned}
\boldsymbol{\alpha}^T &= \left(y^0_{00}, y^{-1}_{20}, y^{-1}_{21}, y^{-1}_{2-1}, y^{-1}_{22}, y^{-1}_{2-2}\right) , \\
\boldsymbol{\psi}^T &= \left(\psi_{,xx}, \psi_{,yy}, \psi_{,zz}, \psi_{,xy}, \psi_{,xz}, \psi_{,yz}\right) .
\end{aligned} \tag{5.19}$$

The inverse mapping M^{-1} is then given by

$$M^{-1} = \begin{pmatrix}
1/3 & -\frac{\sqrt{5}}{15} & 0 & 0 & \frac{\sqrt{30}}{30} & \frac{\sqrt{30}}{30} \\
1/3 & -\frac{\sqrt{5}}{15} & 0 & 0 & -\frac{\sqrt{30}}{30} & -\frac{\sqrt{30}}{30} \\
1/3 & 2\frac{\sqrt{5}}{15} & 0 & 0 & 0 & 0 \\
0 & 0 & 0 & 0 & -\frac{\sqrt{30}}{30}i & \frac{\sqrt{30}}{30}i \\
0 & 0 & -\frac{\sqrt{30}}{30} & -\frac{\sqrt{30}}{30} & 0 & 0 \\
0 & 0 & \frac{\sqrt{30}}{30}i & -\frac{\sqrt{30}}{30}i & 0 & 0
\end{pmatrix} \tag{5.20}$$

Note that the components $y^i_{l\pm m}$ are Hermitian conjugate variables, thus preserving the real nature of the shear field. The amount of tidal shear acting on a halo depends on the length scale $R(M)$ of the halo and thus on its mass. In our model a halo will only be affected by the shear caused by structures with length scale $L \gtrsim R(M)$. Therefore we introduce a cut-off for the power spectrum, suppressing high frequencies

$$P(k) \to P(k) W_R^2(k), \tag{5.21}$$

with $W_R(k) = \exp(-k^2R^2/2)$. The mass scale is obtained via $M = \frac{4\pi}{3}\rho_{crit}\Omega_m R^3$, where $\rho_{crit} = 3H^2/(8\pi G)$ is the critical density. Here all quantities are evaluated today, as the time dependence is taken into account via the time derivative of the growth factor in Eq. (5.10). From the sampled shear values $\psi_{,ij}$ the shear invariant σ^2 can be calculated using Eq. (5.12).

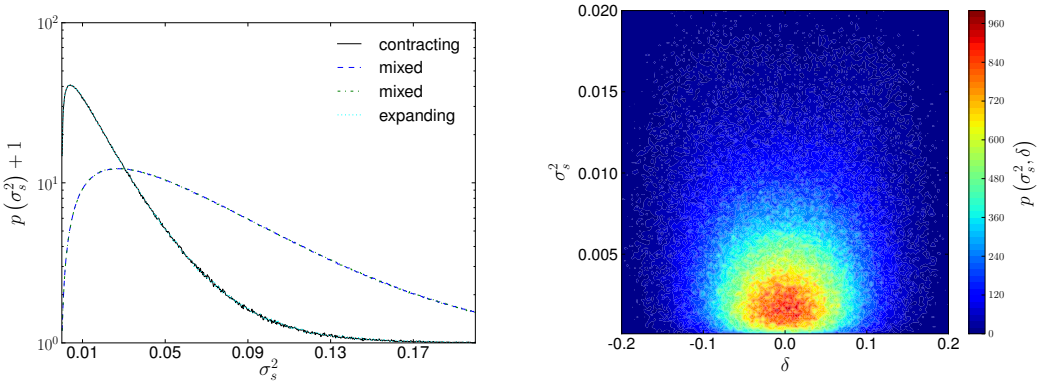

Figure 5.2: *Left*: Distribution of the shear invariant σ_s^2 for different environments. We found that the mixed environment, i.e. where σ_{ij} has positive and negative eigenvalues, is much more likely than the contracting or expanding environment making up for approximately 95% of the sampled values. Note that we again show the normalized distribution with an offset of unity. *Right*: Joint distribution of δ and σ_s^2 for a smoothing radius $R = 30\,\mathrm{Mpc}h^{-1}$.

Clearly for low mass haloes shear becomes more important as the fluctuations in the surrounding density field are larger. Since our model works with a potential flow for the velocities, the variance σ_0 must remain small compared to $|\delta| = 1$, showing the validity of the treatment presented here above a certain scale only on which the evolution of the density contrast can safely be considered as linear. In Figure 5.1 we show the distribution of the sampled density contrast $\delta = \psi_{ii}$ for different mass scales on the left. It is easy to see that smoothing of the density field on smaller scales leads to a broader distribution of delta. Especially this shows that $R \approx 10\,\mathrm{Mpc}h^{-1}$ is the smallest scale at which the approximation used here is applicable as higher order terms will dominate the perturbative expansion. Consequently the velocity field will no longer be a potential flow. Conversely larger scales $R(M)$ will lower the values of σ_s^2, thus high mass halos will be less affected compared to low mass ones. The distribution of the remaining tidal shear invariant σ_s^2 (cf. Eq. (5.12) for details), again for different scales, can be seen in Figure 5.1 on the right.

In Figure 5.2 we show how the invariant σ_s^2 distinguishes between different environments. These are classified by the characteristic of the shear tensor σ_{ij}. Due to $\Delta\psi = \delta$, positive eigenvalues correspond to a collapsing region, while negative eigenvalues correspond to an expanding region. The other two possibilities, i.e. one or two positive eigenvalues, correspond to a mix of both effects. Clearly the tidal shear invariant does not distinguish between contracting and expanding regions, as only the square of the traceless shear tensor enters into the collapse equation. The same is true for the mixed environments. Thus, a fully contracting environment has the same effect on the collapse as a fully expanding one. As halos form in over-dense regions, we are rather interested in a shear value provided the density contrast in

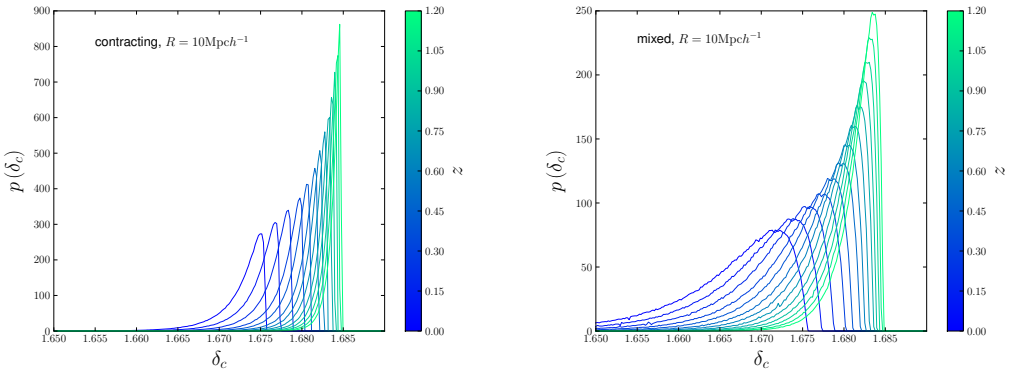

Figure 5.3: Distribution of δ_c in over-dense regions at different redshifts for a radius $R = 10\,\mathrm{Mpc}h^{-1}$. *Left*: Contracting regions, i.e. regions with only positive eigenvalues of the velocity divergence tensor. *Right*: Regions which are partially expanding and partially contracting.

this region satisfies $\delta > 0$. It is important to note that no correlations enter into the model by conditionalizing the random process in such a way. The latter effect is shown in the right panel of Figure 5.2 where the joint distribution of σ_s^2 can be seen to be symmetric around $\delta = 0$ for different values of σ_s^2 as expected from the Gaussian assumption and from Figure 5.1. It is therefore not harmful to neglect all values of the shear matrix which describe an under-dense region. Note that a halo can also form in a large under-dense region. Our results would, however, not be influenced by this effect as we work in the linear regime.

5.4 EFFECT OF MASS AND ENVIRONMENT

The critical linear over-density δ_c in a homogeneous sphere depends on the initial conditions for the linear equation. Those are derived from the fully non-linear equation which in principle includes shear and rotation effects. Within our model δ_c will be influenced by the surrounding shear which is encapsulated in the invariant σ_s^2. As we have seen in Sect. 5.3 the shear values are distributed randomly due to the underlying density field with amplitudes given by the considered scale. Consequently δ_c will also exhibit a distribution rather than a distinct value.

The distribution of δ_c for different collapse redshifts can be seen in Figure 5.3. Contracting environments get less support by tidal shear than mixed environments which is due to the fact that the shear is larger if not all directions are contracting. The high end of both distributions falls off very rapidly which is due to the distribution σ_s^2 growing steeply towards $\sigma_s^2 = 0$. The zero point marks the value for δ_c obtained without tidal shear because σ^2 only enters as a positive contribution in Eq. (5.5) and thus a non-vanishing shear will move the initial conditions for the linear equation to lower values of δ resulting in a smaller value for δ_c. Furthermore the distribution of δ_c becomes narrower if the collapse redshift increases. This is due to the evolution of σ^2 with redshift: physically shear becomes more important with time due to the growth of the cosmic density field. Note that this effect occurs only for z larger than 0.3 since the time evolution of σ^2 in Eq. (5.11) has a maximum at this redshift.

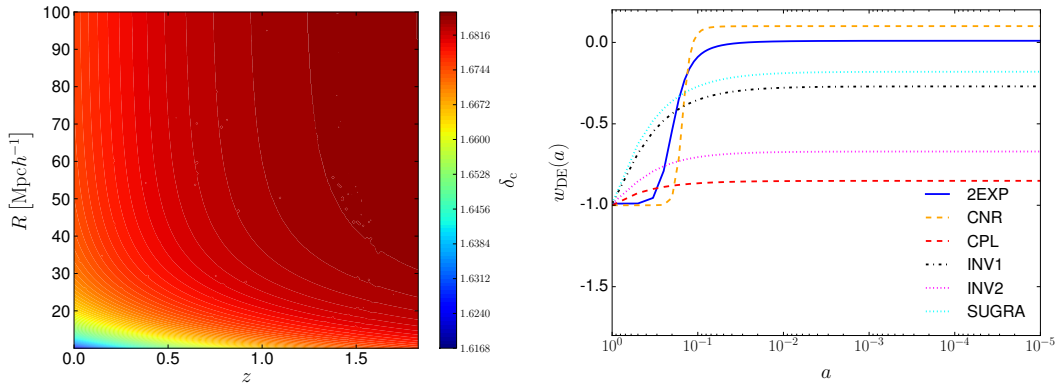

Figure 5.4: *Left*: Mean linearly evolved critical over-density $\bar{\delta}_c(M)$ including the shear as a function of redshift and object scale which is related to the mass of an object via $M = \frac{4\pi}{3} R^3 \rho_0$, with $\rho_0 = \rho_{crit}\Omega_m$. Clearly the effect of external shear is most pronounced at low redshifts and low masses, while it converges to the standard ΛCDM value for the other cases. *Right*: Time-dependent equations of state for the models used in this work as a function of the scale factor a. The light-green dashed-dot black and the magenta short-dashed lines represent the model INV1 and INV2, respectively. The blue curve the 2EXP model. The CPL and the CNR models are shown with the red dashed and the orange dashed curve, respectively. Finally the SUGRA model is shown with the cyan dotted curve.

It coincides with the time when the cosmological constant starts dominating the expansion of the universe, slowing down the growth of structures again.

Having evaluated the distribution of δ_c we can define an effective $\bar{\delta}_c$ which is taken to be the mean:

$$\bar{\delta}_c(M) = \int d\delta_c \; \delta_c \; p(\delta_c, M). \tag{5.22}$$

This mean value is now a function of the mass of the considered halo, which is carried by the amplitude of the density fluctuations on scales larger than the corresponding scale $R(M)$ of the halo and of the redshift via the collapse equation. The left panel of Figure 5.4 shows $\bar{\delta}_c$ as a function of the halo mass in units of $M_\odot h^{-1}$ and of the redshift. As expected from the previous discussion, δ_c is mostly influenced at small radii and small redshifts as shear effects are most important in this regime.

5.5 EFFECT OF COSMOLOGY

Previous works on the effects of shear and rotation on the parameters of the spherical collapse model showed that the behaviour of these additional non-linear terms is mildly affected by the change of the background cosmological model. While overall their mutual combination had the same qualitative effect (increase in δ_c and negligible effect at high masses), differences of the order of several percent appeared across different cosmological models considered. In this section we analyse the effects of dark energy on the linear extrapolated density parameter δ_c and on the virial overdensity when we add the contribution of the shear field as outlined in the previous sections. The models here investigated have been explored before with the same purpose, albeit, as said before, a direct comparison is not possible at this stage. For more

Table 2: Parameter values for the dark energy models with dynamical equation-of-state parameter.

Model	w_0	w_m	a_m	Δ_m
2EXP	-0.99	0.01	0.19	0.043
INV1	-0.99	-0.27	0.18	0.5
INV2	-0.99	-0.67	0.29	0.4
CNR	-1.0	0.1	0.15	0.016
SUGRA	-0.99	-0.18	0.1	0.7

details on the models we refer the reader to Pace et al., 2010 for homogeneous dark energy and to 2014, b for clustering dark energy models. We will explore the effect of dark energy inhomogeneities in a following work.

In particular we will explore the effect of the tidal shear in models described by the following equation-of-state parametrization: three models with constant equation of state ($w_{DE} = -1$ for the cosmological constant Λ, $w_{DE} = -0.9$ for quintessence models and $w_{DE} = -1.1$ for phantom models), and six models with a dynamical equation of state:

- the 2EXP model (Barreiro et al., 2000),
- the CNR and the SUGRA model (Copeland et al., 2000),
- the CPL model (Chevallier and Polarski, 2001; Linder, 2003),
- the INV1 and INV2 models (Corasaniti and Copeland, 2003; Corasaniti, 2004; Sánchez et al., 2009).

In Figure 5.4 we show for clarity on the right the dynamical dark energy models used in this work. The CPL and the INV2 models show a very gentle increase of the equation-of-state parameter while the models SUGRA and INV1 present a more rapid change of the equation of state. The CNR model is approximately constant at low redshifts and is characterized by a sudden change for $a \approx 0.1$. All the models are approximately constant at small scale factors and $w_{DE} \approx -1$ for $a \simeq 1$, as inferred from observational data.

The functional form for the CPL model is

$$w_{DE}(a) = w_0 + w_a(1-a)\,, \tag{5.23}$$

and we used $w_0 = -1$ and $w_a = 0.15$.

The other models can be well described by the following four-parameter formula:

$$w_{DE} = w_0 + (w_m - w_0)\frac{1+e^{\frac{a_m}{\Delta_m}}}{1+e^{-\frac{a-a_m}{\Delta_m}}}\frac{1-e^{-\frac{a-1}{\Delta_m}}}{1-e^{\frac{1}{\Delta_m}}}\,. \tag{5.24}$$

In Table 2 we summarize the values of the parameters used.

Except for the EdS model where we assumed $\Omega_m = 1$, we will use for all the dark energy models the following set of parameters (assuming a flat spatial geometry): $\Omega_m = 0.32$, $\Omega_{DE} = 0.68$, $h = 0.67$ and $n_s = 0.966$.

5.5.1 *Spherical collapse parameters*

In this section we will describe the effects of the introduction of the tidal shear on the two main parameters of the spherical collapse model: the linearly extrapolated overdensity δ_c and the virial overdensity Δ_V. The first one is a very important theoretical quantity usually used in the determination of the mass function according to the prescription of Press and Schechter, 1974 and Sheth and Tormen, 1999. The second one instead is used both in observations and in simulations to determine the mass and the size of the object. For details on how to evaluate them, we refer to Pace et al., 2010; 2012; 2014, a; b.

In Figure 5.5 we show our findings for the parameter δ_c in several dark energy models, with respect to the ΛCDM model and to the respective values in absence of tidal shear. We refer the reader to the caption for the different colours and line-styles adopted for each model. In the left panels we show models with constant equation of state and in the right panels some dynamical models (i.e. with a time-varying equation-of-state parameter.)

From a first qualitative analysis, results are as expected. Tidal shear favours the collapse and the linearly extrapolated overdensity parameter δ_c is smaller than in the spherically symmetric case with no external tidal shear (compare the upper panels with values at $z = 0$ in the bottom panels). The linear overdensity obviously depends on the halo mass now; stronger effects take place at low masses, at high masses the effect is negligible and the result converges to the standard spherically symmetric solution. This is particularly evident for the EdS model (blue dotted curve). Note however that differences from the standard case are quite small, below the 1% level. In the middle panel we fix the mass of the collapsing object at $M = 10^{14}\ M_\odot/h$, so to amplify the effect of the tidal shear, and we study the time evolution of the parameter δ_c. It is illuminating to compare it with the time evolution of the spherically symmetric case (bottom panel) and despite the results are not new since already derived and discussed previously in 2010, we report them once again for clarity. First of all notice that due to the tidal shear, for the EdS model δ_c becomes time-dependent. Effects of the introduction of the ellipticity are more pronounced at low redshifts and they become negligible at high redshift, where the new solution converges to the standard value. Similar results, both qualitatively and quantitatively are obtained for generic dark energy models. All the models analysed show lower values for δ_c, especially at the lower end of the mass interval considered. At high masses values converge to the spherical case. Effects of the tidal shear are most evident at low redshifts and negligible at high redshifts. For $z \gtrsim 3$, the tidal shear contribution is totally negligible. Also for dynamical dark energy models, deviations from the standard case are below 1%.

In Figure 5.6 we present results for the virial overdensity parameter Δ_V. Interestingly, this quantity is insensitive to the introduction of the tidal shear and its time evolution is practically identical to what observed for the standard spherically symmetric case. This implies that for the virial overdensity, the solution of the standard theoretical model is an excellent approximation also for the case including the tidal shear. The reason why the results of the two approaches are identical, is due to the fact that the non-linear overdensity at turn-around, ζ, is insensitive to the tidal shear. Also note that in general, differences between the dark energy models and the ΛCDM model are very limited.

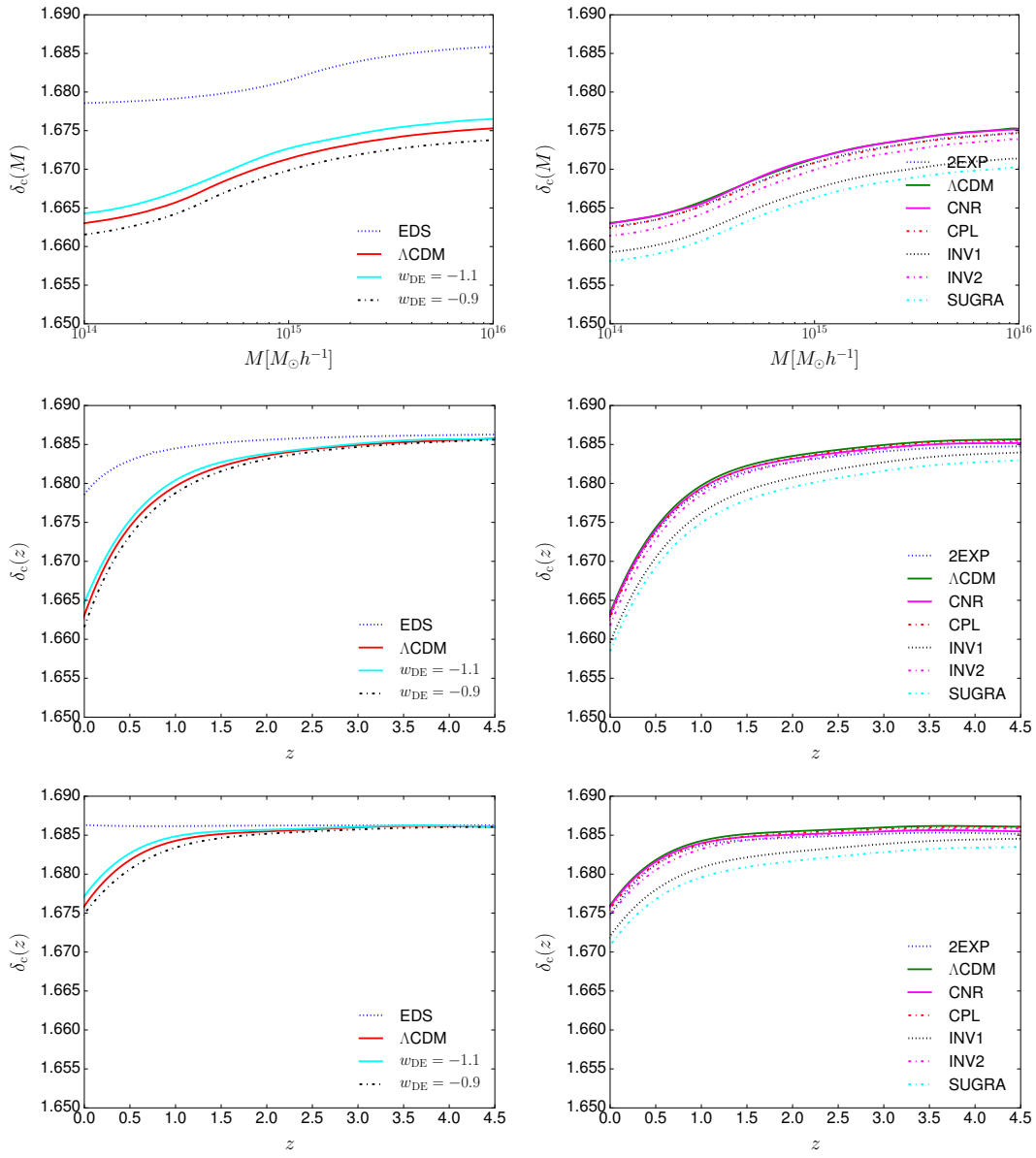

Figure 5.5: *Upper panels*: effects of the tidal shear on δ_c at $z = 0$ for different values of the mass of the collapsing sphere. *Middle panels*: time evolution of δ_c for a mass of $M = 10^{14}\ M_\odot/h$. *Bottom panels*: time evolution of the linear extrapolated overdensity parameter for the standard spherical collapse model (without the inclusion of the tidal shear). Left (right) panels refer to constant (dynamical) equations of state. The red solid line refers to the reference ΛCDM model. For models with constant equation of state, the blue dotted curve shows an EdS model, while the black dashed-dot (cyan solid) curve shows a quintessence (phantom) model with $w_{DE} = -0.9$ ($w_{DE} = -1.1$). For dynamical dark energy models, the black dotted (magenta dashed-dot) curve represents the INV1 (INV2) model; the blue dashed curve the 2EXP model; the CPL (CNR) model with the red dashed-dot (magenta solid) curve and finally the SUGRA model with the cyan dashed-dot-dotted curve.

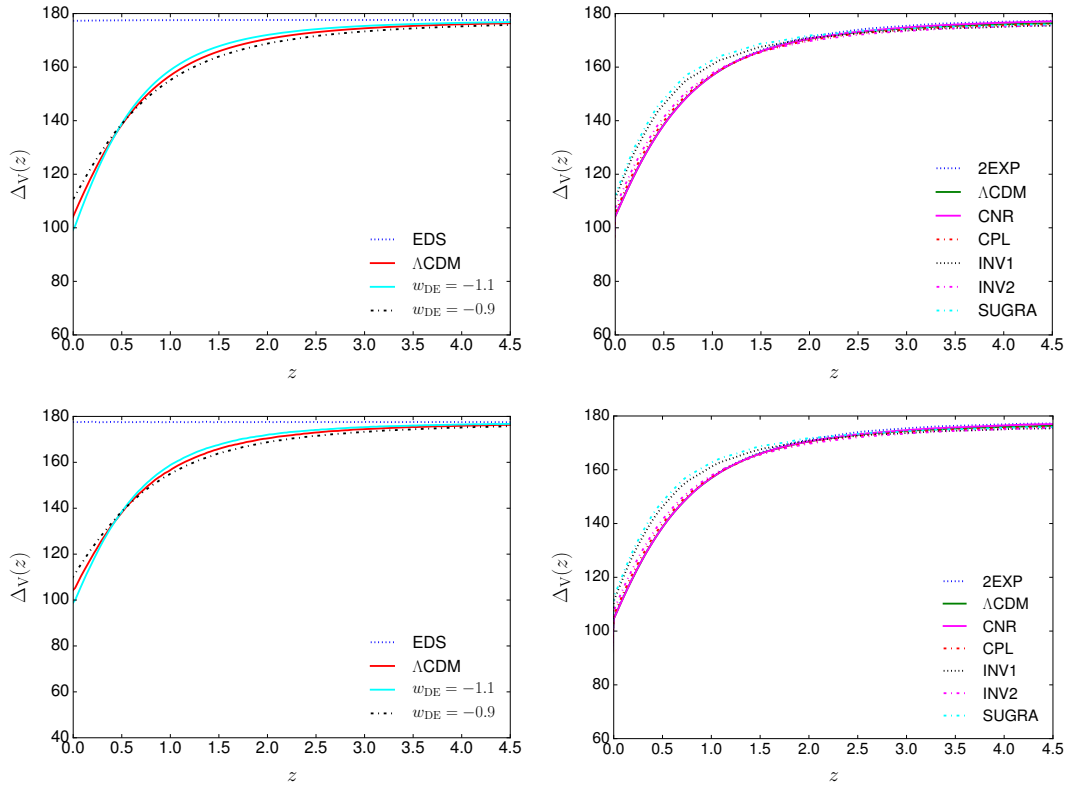

Figure 5.6: *Upper panels*: time evolution of Δ_V for a mass of $M = 10^{14}\ M_\odot/h$. *Bottom panels*: time evolution of the virial overdensity for the standard spherical collapse model. Left (right) panels refer to constant (dynamical) equations of state. Line-styles and colours are as in Figure 5.5.

Our results for δ_c are qualitatively similar to the works of Del Popolo et al., 2013a and b, albeit with some important differences and, as discussed before, with our formalism we can not do a quantitative comparison. First of all, δ_c shows a mass dependence similar to the works mentioned. Effects of the modified collapse increase with decreasing mass and at the very high mass tail these modifications become negligible. Regarding the time dependence, also in our case larger modifications take place at low redshifts and at high enough z, the spherical case is an excellent approximation. In a and b, the authors showed an increase in δ_c rather than a decrease. However, in their heuristic model the dominant term was given by the rotation tensor, hence we would expect a slow-down of the collapse. It would be therefore interesting to find an approach, similar to what we did here, to take into account also the rotation term and then compare the two different approaches. The situation is completely different for the virial overdensity Δ_V: in our case it is totally independent of the tidal shear, hinting towards the hypothesis that probably the rotation is more important or that it is sensitive to the particular prescription adopted. Since the virial overdensity Δ_V is largely independent of the tidal shear, it is interesting to examine why this happens. First of all it is useful to notice that our values for the tidal shear are much smaller than the ones used by Del Popolo and collaborators. To show this, it is sufficient to evaluate the relative strength of the shear term with respect to the Poisson term. In other words we are giving an estimate of the parameter α used in a; b. We find that

in this work, $\alpha \simeq 10^{-8}$, while in previous works it was of the order of few per mill for an object of $10^{14}\ M_\odot/h$.

To have a physical insight of this, we recall the definition of the virial overdensity. Note that we assume it with respect to the critical density, but the same result would apply if we would define it with respect to the background density. The virial overdensity is defined as

$$\Delta_V = \zeta \left(\frac{x}{y}\right)^3 , \tag{5.25}$$

where $\zeta = \delta(a_{ta}) + 1$ is the overdensity at turn-around, $x = a/a_{ta}$ is the scale factor normalised at the turn-around and finally $y = R_{vir}/R_{ta}$ is the virial radius normalized to the turn-around radius. As σ^2 enhances the collapse, ζ is smaller than the perfectly spherically symmetric case, as we need a smaller initial overdensity δ_{ini} to reach the collapse at z_c. But ζ is evaluated only in the mildly non-linear regime, therefore it is only slightly smaller and the relative contribution of the σ^2 term compared to the Poisson term (the α coefficient) is to be about a few per mill at turn-around, in perfect quantitative agreement with our findings about the change of Δ_V.

On the other hand z_{ta} is slightly larger, but the effect is really small. The virialisation condition leading to $y = R_{vir}/R_{ta}$ does not directly depend on σ^2, but only indirectly via z_{ta}. By Taylor expanding Δ_V around the spherically symmetric case ($\sigma^2 = 0$), we have the following relations (the index o refers to the absence of shear):

$$\Delta_V = \Delta_{V,0} \left(1 + \frac{\delta\zeta}{\zeta_0} + 3\frac{\delta z_{ta}}{1+z_{ta,0}} - 3\frac{\delta y}{y_0}\right) , \tag{5.26}$$

where, for a ΛCDM model at $z_c = 0$, we have:

$$\frac{\delta\zeta}{\zeta_0} \simeq -0.015 , \quad \frac{\delta z_{ta}}{1+z_{ta,0}} \simeq 0.0014 \quad \frac{\delta y}{y_0} \simeq -0.0047 .$$

It is therefore clear that albeit extremely small, the dominant contribution is due to the change in ζ, making as expected the virial overdensity only slightly smaller than in the spherical case.

It is also interesting to make a more direct comparison with the ellipsoidal collapse. One of the goals of this work is to establish whether a Press-Schechter formulation of the mass function with the corrections induced on δ_c by the tidal shear tensor could give predictions closer to a Sheth-Tormen formulation with the standard δ_c values. According to Bond and Myers, 1996, the collapse time depends on the ellipticity e and prolaticity p and the dependence of the collapse threshold of an ellipsoidal region can be well approximated by the solution of (Sheth et al., 2001)

$$\frac{\delta_{ec}}{\delta_{sc}} = 1 + \beta \left[5(e^2 \pm p^2)\frac{\delta_{ec}^2}{\delta_{sc}^2}\right]^\gamma , \tag{5.27}$$

where δ_{ec} and δ_{sc} are the values of the critical overdensity for the ellipsoidal and spherical case, respectively and β and γ are parameters to be fitted to the results. Doroshkevich, 1970 and Sheth et al., 2001 found that

$$\delta_{ec} = \delta_{sc}\left[1 + \beta\left(\frac{\sigma(M)^2}{\delta_{sc}}\right)^\gamma\right] , \tag{5.28}$$

with $\beta = 0.47$ and $\gamma = 0.615$. With $\sigma(M)$ of the order unity, δ_{ec} is about 25% - 30% bigger than δ_{sc}. We can therefore conclude that the tidal shear will have small effects on the mass function, as shown later in Figure 5.7.

5.6 MASS FUNCTION

The halo mass function describes the differential abundance of objects with mass M at redshift z. Working within the theory of Gaussian random fields, the main ingredient is the comparison of fluctuations of the linearly evolved density field with δ_c. Objects exceeding δ_c on a certain scale $R(M)$ are then counted as clusters. The fluctuations of the density field are described by the variance σ_R of the underlying random field filtered with a top-hat having a certain scale. Press and Schechter (1974) showed that the mass function (PS) has the form

$$n(M,z) = \frac{2\rho_0}{\pi M}\frac{\delta_c(z)}{D_+\sigma_R}\left|\frac{\partial \ln \sigma_R}{\partial M}\right| \exp\left(-\frac{\delta_c^2(z)}{2D_+^2(z)\sigma_R^2}\right) , \tag{5.29}$$

where the growth factor D_+ accounts for the linear evolution. More elaborate forms of the mass function, fitting numerical N-body simulations better, are given in Sheth and Tormen (1999) or Jenkins et al. (2001). The important functional form for our purpose is however given by the term

$$\frac{\delta_c(z)}{D_+\sigma_R}\exp\left(-\frac{\delta_c^2(z)}{2D_+^2(z)\sigma_R^2}\right), \tag{5.30}$$

where we replace

$$\delta_c(z) \to \bar{\delta}_c(M,z) , \tag{5.31}$$

i.e. we insert the effective δ_c. This has important consequences: Firstly, δ_c changes with the mass which will lead to a different form of the mass function. Furthermore, the shear causes δ_c to be smaller than without shear as it only supports the collapse. Due to the functional form of the mass function we therefore expect more massive haloes in the mass regime where the exponential factor dominates the linear one. On smaller scales, however, the linear term will dominate, thus causing the mass function to tend to smaller values. The reason for this behaviour is that small haloes can form more massive haloes more easily, thus yielding fewer smaller objects. Finally the time dependence of the shear is different from the linear growth of σ_R, we thus expect different impacts of the shear on different redshifts which in principle can make ΛCDM and wCDM models degenerate.

We now want to infer the influence of the tidal shear on the mass function for the several dark energy models analysed in this work. To do so, we evaluate the cumulative comoving number density of objects above a given mass at $z = 0$. For all the models we assume $\sigma_8 = 0.776$. This is done not to introduce volume and normalization effects that would mask the contribution of the tidal shear, that, as we will see, amounts to few percent in a ΛCDM model.

We present our results in Figure 5.7, where we show the ratio between the dark energy and the reference ΛCDM model. In the left panels we show the ratio between the models with and without tidal shear field while in the right panels we show the ratio between the dark energy and the ΛCDM model with tidal shear field.

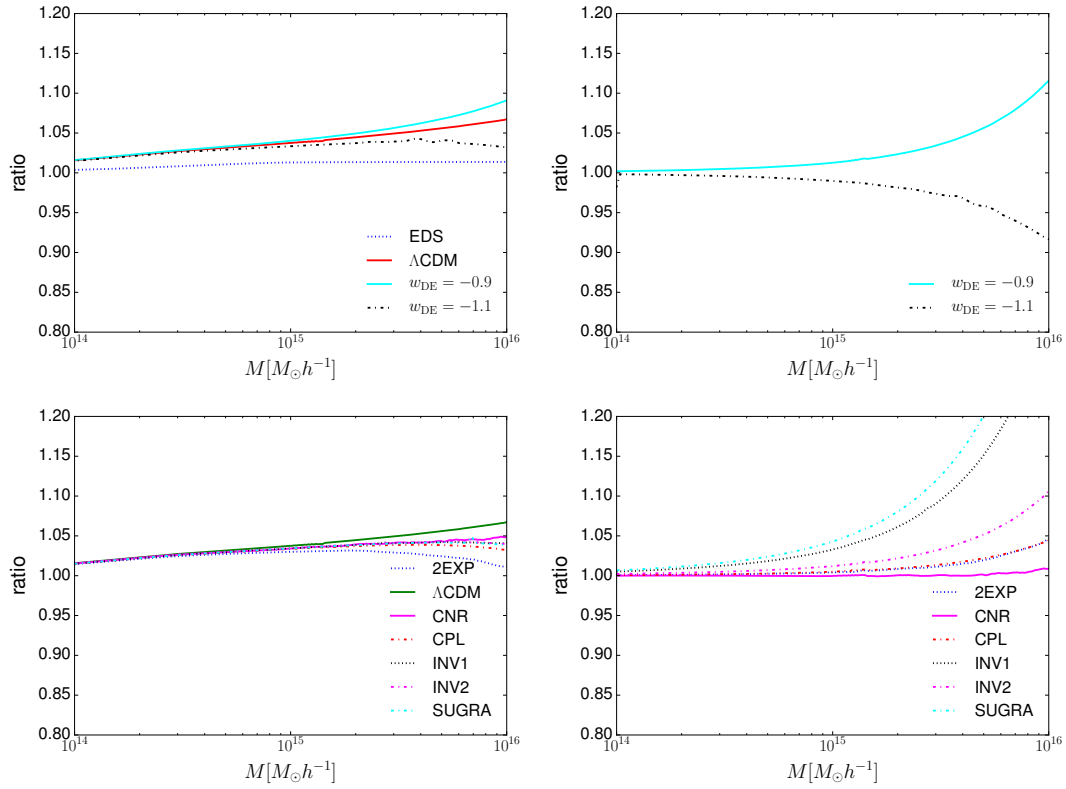

Figure 5.7: Ratio of the cumulative comoving number density of objects above mass M evaluated at $z = 0$. *Left column*: ratio between the expected number counts of the models with and without tidal shear contribution. *Right column*: ration between the dark energy and the ΛCDM model taking into account the effects of the tidal shear. Upper panels show results for the EdS model and dark energy models with constant equation of state ($w_{DE} = -0.9$ and $w_{DE} = -1.1$). Lower panels show results for dynamical dark energy models. Line-styles and colours are as in Figure 5.5.

By inspecting the left panels, we realize that, as expected, tidal shear has a modest contribution, usually growing with increasing mass. The effect is of the order of few percent at the lower limit of applicability of our formalism ($M \approx 10^{14}\ M_\odot/h$) and it increases up to 10% for a model with constant $w_{DE} = -0.9$ at very high masses ($M \approx 10^{16}\ M_\odot/h$). The model being least affected is the EdS, somehow in agreement with what found for the spherical collapse parameter δ_c. Interestingly, the SUGRA model shows an increase with mass up to $M \simeq 10^{15}\ M_\odot/h$ and a slow decrease to bring the model with tidal shear close to the standard one. Note that however differences are never bigger than about 3% for this model. Also note that, except for the model with constant $w_{DE} = -0.9$, all the other models show an effect less pronounced in the high mass tail than the ΛCDM model and all the models, except for the EdS one, are identical to the ΛCDM model up to masses of $\simeq 10^{15}\ M_\odot/h$.

In the right panels we show the ratio between the dark energy models and the ΛCDM one, both with the effects of the tidal shear field included. Results are both qualitatively and quantitatively as expected. For models with constant equation of state, the quintessence (phantom) model predicts more (less) objects with respect to the ΛCDM model and differences grow increasing the halo mass. All the dynamical dark energy models are in the quintessence regime and we see, as expected, more ob-

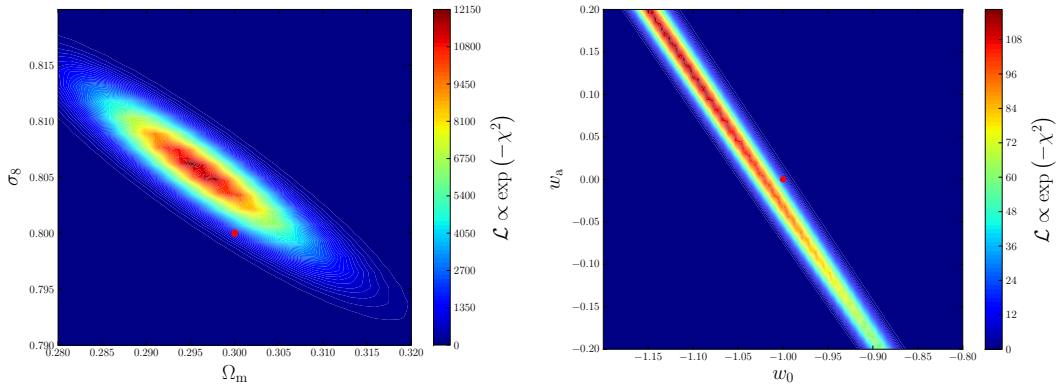

Figure 5.8: Bias on cosmological parameters for redshift cluster counts. Parameters not shown in the respective plot are fixed to their fiducial values. The red dot marks the fiducial cosmology with shear.

jects than the ΛCDM one. The CNR model behaves essentially as the ΛCDM model and the models CPL and 2EXP are practically indistinguishable and predict about 5% more objects than the ΛCDM one. Major differences arise for the SUGRA and the INV1 model.

The mass function described in Sheth and Tormen, 1999 was introduced, as said above, to have a better match with N-body simulations. To do so, the authors incorporated the effect of shear in their calculations within the formalism of the ellipsoidal collapse model. The main quantity characterising the mass function is still the ratio δ_c/D_+ and effects due to the ellipsoidal collapse are incorporated directly in functional form of the mass function. We can therefore try to answer the following question: Will the Press-Schechter mass function approximate better the Sheth-Tormen mass function by using relation (5.31)? The idea behind that is in principle incorporating the tidal shear effects into the linear overdensity parameter and making it mass-dependent could compensate the necessity of modifying the functional form of the mass function. However, as one can see already in Figure 5.5, the influence on the mass function will only be a few percent. Accordingly it will of course improve the agreement between the Sheth Tormen mass function and the PS mass function, nonetheless this improvement is rather marginal with respect to the differences of the two mass functions at the high mass end. This can also be seen from the elliptical collapse model where the effective influence on δ_c is much larger than in our case leading to a big change in the number counts due to the exponential tail for massive objects including the collapse threshold (see Section 5.2 for a more detailed discussion).

5.7 CLUSTER COUNTS

From the mass function, cluster counts can be calculated, which can then be compared to observational data. Using Sunyaev-Zel'dovich cluster surveys (Sunyaev and

Zeldovich, 1980), the number of objects exceeding a mass M_{min} in a redshift bin z_i is given by (Majumdar, 2004)

$$N(z_i) \equiv N_i = 4\pi f_{sky} \int_{z_i-\Delta z_i/2}^{z_i+\Delta z_i/2} dz \frac{dV}{dz} \int_{M_{min}(z)}^{\infty} dM\, n(M,z)\,, \tag{5.32}$$

where f_{sky} is the fraction of the sky. M_{min} has a redshift dependence included. Assuming a Gaussian likelihood, the log-likelihood is given by χ^2:

$$2\chi^2 \equiv L = \sum_i \frac{(N_i - \langle N_i \rangle)^2}{N_i}\,, \tag{5.33}$$

where we sum over all redshift bins and Poisson errors are assumed. $\langle N_i \rangle$ is the model dependent expected number of objects in the i-th bin, while N_i describes the data. We chose redshift bins with $\Delta z = 0.02$ ranging from $z_{min} = 0.01$ to $z_{max} = 2$. For simplicity we assume $M_{min} = 10^{14} h^{-1} M_\odot$ to be redshift independent. The mock data is sampled from a Poisson distribution with mean N_i evaluated at the fiducial cosmology with $\Omega_{mo} = 0.3$, $\Omega_\Lambda = 0.7$, $\sigma_8 = 0.8$, $w_0 = -1$ and $w_a = 1$ and including shear effects in the mass function, cf. Eq. (5.31). A cosmological model without shear effects is fitted to this data, leading to biases in the cosmological parameters.

In Figure 5.8 we show the resulting biases in parameter space. The red dot marks the fiducial cosmology at which the data was sampled from a mass function including tidal shear via δ_c. In contrast the black dot marks the best fit value of cosmological models without shear effects acting on δ_c. Ignoring shear effects accordingly leads to wrong cosmological parameters, which are shifted by $\sim 1\sigma$ with respect to the true values for both (Ω_m, σ_8) and (w_0, w_a).

5.8 SHEAR AND ROTATION

5.8.1 *The model*

We now want to model the shear invariant σ^2 together with the rotation invariant ω^2 which occur in the collapse equation (5.5). Earlier works studied the joint influence of shear and rotation in a phenomenological way as mentioned in an earlier section. The logic here is the following: We assume that dark matter halos form at peaks of the density field, which itself is described by a Gaussian random field and thus by its power spectrum. In order to model $\sigma^2 - \omega^2$ we calculate these values at peaks of the density field using only the statistics of the field itself and the ZA. We then effectively place a test particle into the Gaussian random field at the peak and let it undergo gravitational collapse, with the shear and rotation acting as external forces with no own dynamics (except for the ones given by the background dynamics). Thus the collapse dynamics will stay spherical, while we allow for deviations from sphericity in the estimation of the shear and rotation (especially to find an expression for the inertial tensor). In this way the collapsing object can be seen as a test particle in a tidal gravitational field.

5.8.2 *The tidal tensor and tidal torquing*

The central object of our model is the tidal tensor $\boldsymbol{\Psi}$, which is related to the density field and whose statistics where described in Section 5.3. Its components are given by $(\boldsymbol{\Psi})_{ij} = \partial_{ij}\psi$, as in Eq. (5.19), but now ordered in a rank two tensor.

We now introduce a mechanism known as tidal torquing in order to describe the generation of rotation due to tidal gravitational fields. In the picture of tidal torquing angular momentum is generated by the tidal gravitational field which exerts a torquing moment on the halo. It is important to note that the vorticity $\boldsymbol{\omega}$ is not driven by the non-linear term $\nabla \times (\boldsymbol{v} \times \boldsymbol{\omega})$ in the Euler equation. On the contrary, the angular momentum is generated by vorticity-free flows generating shear effects on the halo prior to collapse. During this process the halo is slightly deformed and tends to align its inertia tensor in the eigenframe of the shear tensor. After decoupling from the shear flow and the start of collapse the length of the lever arms reduces dramatically in comoving coordinates making tidal torquing inefficient. Therefore, the angular momentum just before collapse begins is a good proxy for the total rotation of the halo.

The angular momentum $\mathbf{L}$ of a rotating mass distribution $\rho(\mathbf{r}, t)$ is given by

$$\mathbf{L}(t) = \int_V d^3r\, (\mathbf{r} - \bar{\mathbf{r}}) \times \boldsymbol{v}(\mathbf{r}, t)\rho(\mathbf{r}, t)\,, \tag{5.34}$$

with $\boldsymbol{v}$ being the rotational velocity and V the physical volume under consideration. Making use of the ZA and expressing everything in the Lagrangian-frame (i.e. comoving), the angular momentum becomes

$$\mathbf{L} = \rho_0 a^5 \int_{V_L} d^3q\, (\mathbf{q} - \bar{\mathbf{q}}) \times \dot{\mathbf{x}}\,, \tag{5.35}$$

neglecting higher order terms (White, 1984; Catelan and Theuns, 1996; Crittenden et al., 2001). The velocity $\dot{\mathbf{x}}$ is given via the gradient of the potential ψ, which can be expanded in the vicinity of the centre of gravity $\bar{\mathbf{q}}$ if its variation across the Lagrangian volume V_L is small:

$$\partial_i\psi(\mathbf{q}) \approx \partial_i\psi(\mathbf{q})\big|_{\mathbf{q}=\bar{\mathbf{q}}} + \partial_{ij}\psi(q)\big|_{\mathbf{q}=\bar{\mathbf{q}}}(\mathbf{q} - \bar{\mathbf{q}})_j\,, \tag{5.36}$$

with expansion coefficients $\psi_{ij} \equiv \partial_{ij}\psi$ describing the tidal shear given in Eq. (5.19). The first term can be neglected as it only describes the displacement of the protohalo, the second however will be responsible for the rotational effects. Introducing the inertial tensor I_{ij} as

$$I_{ij} = \rho_0 a^3 \int_{V_l} d^3q\, (\mathbf{q} - \bar{\mathbf{q}})_i(\mathbf{q} - \bar{\mathbf{q}})_j\,, \tag{5.37}$$

the angular momentum can be written as

$$L_i = a^2\dot{D}_+\epsilon_{ijk}I_{jl}\psi_{lk}\,, \tag{5.38}$$

with the Levi-Civita symbol ϵ_{ijk}. The matrix product in the latter expression $\mathbf{X} = \mathbf{I}\boldsymbol{\Psi}$ can be decomposed into a symmetric $\mathbf{X}^+$ and anti-symmetric part $\mathbf{X}^-$ defined via the anti-commutator and the commutator, respectively:

$$\mathbf{X}^+ \equiv \frac{1}{2}\{\mathbf{I}, \boldsymbol{\Psi}\}\,, \quad \mathbf{X}^- \equiv \frac{1}{2}[\mathbf{I}, \boldsymbol{\Psi}]\,. \tag{5.39}$$

With this definition the angular momentum can be written as (Schäfer, 2009; Schäfer and Merkel, 2012)

$$L_i = a^2 \dot{D}_+ \epsilon_{ijk} X_{jk} = a^2 \dot{D}_+ \epsilon_{ijk} X^-_{jk}, \tag{5.40}$$

since the contraction with ϵ_{ijk} will only pick out the anti-symmetric part of $\mathbf{X}$. Thus, angular momentum is not generated if inertia and tidal shear have a common eigen-system, which is always the case for a matter distribution invariant under SO(3), therefore we need to have $\mathbf{X}^- \neq 0$ to generate angular momentum. On the other hand $\mathbf{X}^+$ will measure the alignment of the eigensystems of inertia and shear and thus cause shear effects due to deformations.

The components of the inertial tensor $\mathbf{I}$ can be expressed via second derivatives of the density field $\delta(\mathbf{x})$ which are given by

$$\delta_{ij} = -\int \frac{d^3k}{(2\pi)^3} k_i k_j \delta(\mathbf{k}) \exp(i\mathbf{k}\mathbf{x}) \, . \tag{5.41}$$

Thus the decomposition works in the same way as before:

$$\begin{aligned} \sigma_2 y^0_{20} &= -\sqrt{5/4}\,(\delta_{xx} + \delta_{yy} - \delta_{zz}) \, , \\ \sigma_2 y^0_{2\pm1} &= -\sqrt{15/2}\,(\delta_{xz} \pm i\delta_{yz}) \, , \\ \sigma_2 y^0_{2\pm2} &= \sqrt{15/8}\,(\delta_{xx} - \delta_{yy} \pm 2i\delta_{xy}) \, , \\ \sigma_2 y^1_{00} &= (\delta_{xx} + \delta_{yy} + \delta_{zz}) \, . \end{aligned} \tag{5.42}$$

At a peak in the density field, the peak slope is approximated by a parabolic function

$$\delta(\mathbf{x}) = \mathbf{x}_p - \frac{1}{2}\lambda_i (\mathbf{x} - \mathbf{x}_p)^2_i \, , \tag{5.43}$$

with the eigenvalues λ_i of the mass tensor $m_{ij} = -\delta_{ij}$ at the peak. If the boundary of the peak is given by the isodensity contour with $\delta = 0$, the inertia tensor can be written as

$$\mathbf{I} = \frac{\eta_0}{5} \Gamma \, \mathrm{diag}\left(A_y^2 + A_z^2, A_x^2 + A_z^2, A_x^2 + A_y^2\right) \, , \tag{5.44}$$

in the eigen-system of the paraboloid. Here $A_i = \sqrt{2\delta/\lambda_i}$ are the ellipsoids semi-axes, Γ its volume and η_0 its density, such that $M = \eta_0 \Gamma$ is the mass of the peak. In our approximation the density field is assumed to be homogeneous to first order and thus $\eta_0 = \Omega_m \rho_{crit} a^3$. We thus sample values for $\mathbf{X}^\pm$ from the joint covariance matrix of δ_{ij} and ψ_{ij}. All calculations are carried out in the eigen-system of the inertia tensor, i.e. we sample values y^n_{lm} and calculate the inertia tensor by inverting Eq. (5.42) and using Eq. (5.44).

5.8.3 *Decomposition of the shear tensor*

In the last two parts we described how the statistics of the density field induce tidal gravitational fields, encoded in $\mathbf{\Psi}$, and how these tidal fields can give rise to rotation. Since the shear effects are as well described by the tidal tensor the scope

of this section will be to decompose $\boldsymbol{\Psi}$ into two separate parts whose invariants can be identified with σ^2 and ω^2. Physically the shear corresponds to convergent flows, which will deform the halo, while the rotational part will give rise to an overall spinning of the halo induced by the external fields. As already mentioned, angular momentum will only be sourced by the anti-symmetric part of the matrix product $\mathbf{X}$; the Hodge dual to the angular momentum is the tensor

$$L_{ij} = a^2 \dot{D}_+ [\mathbf{I}, \boldsymbol{\Psi}]_{ij} \,. \tag{5.45}$$

Now, since the angular momentum can also be expressed as

$$L_i = I_{ij} \omega_j \,, \tag{5.46}$$

with angular velocity ω_j, we can conclude that

$$L_{ij} = I_{il} \omega_{lj} \,, \tag{5.47}$$

and thus, in matrix-vector notation

$$\boldsymbol{\omega} = \mathbf{I}^{-1} \mathbf{X}^- \,. \tag{5.48}$$

For the shear we proceed in complete analogy, but using the anti-commutator instead of the commutator. In particular we decompose the tidal gravitational field as follows:

$$\boldsymbol{\Psi} = \mathbf{I}^{-1} \mathbf{I} \boldsymbol{\Psi} = \mathbf{I}^{-1} \mathbf{X}^+ + \mathbf{I}^{-1} \mathbf{X}^- \equiv \tilde{\boldsymbol{\sigma}} + \tilde{\boldsymbol{\omega}} \,. \tag{5.49}$$

Here we identified the shear tensor $\tilde{\boldsymbol{\sigma}}$ and the rotation tensor $\tilde{\boldsymbol{\omega}}$. Since $\tilde{\boldsymbol{\sigma}}$ still carries a trace we need to subtract it to arrive at the following expressions for the shear tensor and rotation tensor respectively:

$$\boldsymbol{\sigma} = \frac{1}{2} \left(\boldsymbol{\Psi} + \mathbf{I}^{-1} \boldsymbol{\Psi} \mathbf{I} \right) - \frac{\mathrm{tr} \boldsymbol{\Psi}}{3} \mathbb{I}_3 \,, \quad \boldsymbol{\omega} = \frac{1}{2} \left(\boldsymbol{\Psi} - \mathbf{I}^{-1} \boldsymbol{\Psi} \mathbf{I} \right) \,. \tag{5.50}$$

The interpretation of the two expressions is straightforward: $\boldsymbol{\sigma}$ measures the alignment between the eigen-frames of the tidal tensor and the inertial tensor, while $\boldsymbol{\omega}$ measures their misalignment. Clearly, if both are completely aligned, the tidal tensor will not induce any rotation and only the shear effect is present. If, however, the two frames are not aligned the inertial tensor will start rotating into the frame of the tidal tensor and keep its rotation once the lever arm will reduce dramatically during collapse.

5.8.4 *Model comparison*

Having set up all the important relations, it is worthy to compare the models presented here with the one from Section 5.3 and the phenomenological model in Del Popolo et al. (2013a) and b.

The procedure in Section 5.3 is quite similar to the one outlined here. Values for the tidal tensor $\boldsymbol{\Psi}$ are sampled in the same way, the values for the inertial tensor, however, are not sampled from the density field and $\mathbf{I}$ is implicitly assumed to be the one of a spherical object. $\mathbf{I}$ is thus proportional to the identity, which itself commutes with

every other tensor, thus setting $\boldsymbol{\omega}$ to zero identically. Especially this means Eq. (5.50) was

$$\boldsymbol{\sigma} = \boldsymbol{\Psi} - \frac{\mathrm{tr}\boldsymbol{\Psi}}{3}\mathbb{I}_3 \,, \quad \boldsymbol{\omega} = 0 \,, \tag{5.51}$$

for the model presented in Section 5.3, thus the inertial tensor is not needed as well as the condition to consider peaks in the density field only. This leads to a few subtle differences between the two models in terms of the physical interpretation: Both models describe the collapse of a spherically symmetric test object in a Gaussian random field. In both cases the tidal tensor $\boldsymbol{\Psi}$ is evaluated from the statistics of the underlying linearly evolved density field and gives rise to effective external forces which act on the collapse equation as an inhomogeneity. While the position of the test mass in Section 5.3 has been arbitrary, we restrict ourself to peaks in the density field here and include the possible spin up due to tidal torquing of the test mass. The restriction to peaks in the density field will generally lead to higher values in $\boldsymbol{\Psi}$ compared to Section 5.3, due to the non-trivial correlation with $\mathbf{I}$. In this sense the model presented here is more realistic, in terms of the shear and rotation being just inhomogeneities entering in the collapse equation, then the one in Section 5.3.

The comparison with b is somewhat more difficult as their model was heuristically motivated only. In contrast our model relies on the statistics of the cosmic density field only and is in this sense only restricted by the validity of Lagrangian perturbation theory at first order. This is certainly valid as long $\delta \ll 1$. If we are considering objects with masses above $10^{14}\ M_\odot$, this criterion is certainly satisfied in the sense of that the variance of the density field smoothed at this scale is well below unity. In particular, b find values for $\omega^2 > \sigma^2$ which is not possible with our treatment. This is because in b, the rotation term was derived to match the angular momentum of galaxies and clusters today, being therefore a non-linear quantity. This value will be exceeding our estimate of the rotation tensor and lead to effects that are opposite to what we find.

5.8.5 *Calculation of the invariant* $\sigma^2 - \omega^2$

The invariant quantities σ^2 and ω^2 just differ by the sign of the cross terms and by the terms which arise due to the term including the trace of $\boldsymbol{\Psi}$. It is easy to see that the latter terms vanish identically, thus the only difference between σ^2 and ω^2 is the sign of the two cross terms, which are themselves identical due to the cyclicity of the trace. Generalizing this reasoning to higher order invariants in a coordinate free way, we use that the invariants correspond to the Frobenius-norm of the tidal tensor and the inertia tensor. The Frobenius norm of a symmetric matrix $\mathbf{A}$ is defined as

$$||\mathbf{A}||^2 := \mathrm{tr}\mathbf{A}^2 \equiv A_{ij}A^{ji} \,. \tag{5.52}$$

An inner product can be defined in the following way:

$$\langle \mathbf{A}, \mathbf{B} \rangle = \mathrm{tr}\mathbf{A}\mathbf{B} = A_{ij}B^{ji} \,, \tag{5.53}$$

which is also called Frobenius scalar product, then inducing the Frobenius norm defined above. With this we find

$$\begin{aligned} \sigma^2 &= ||\{\mathbf{I}, \boldsymbol{\Psi}\}||^2 = ||\mathbf{I}\boldsymbol{\Psi}||^2 + 2\langle \mathbf{I}\boldsymbol{\Psi}, \boldsymbol{\Psi}\mathbf{I} \rangle + ||\boldsymbol{\Psi}\mathbf{I}||^2 \\ \omega^2 &= ||[\mathbf{I}, \boldsymbol{\Psi}]||^2 = ||\mathbf{I}\boldsymbol{\Psi}||^2 - 2\langle \mathbf{I}\boldsymbol{\Psi}, \boldsymbol{\Psi}\mathbf{I} \rangle + ||\boldsymbol{\Psi}\mathbf{I}||^2 \end{aligned} \tag{5.54}$$

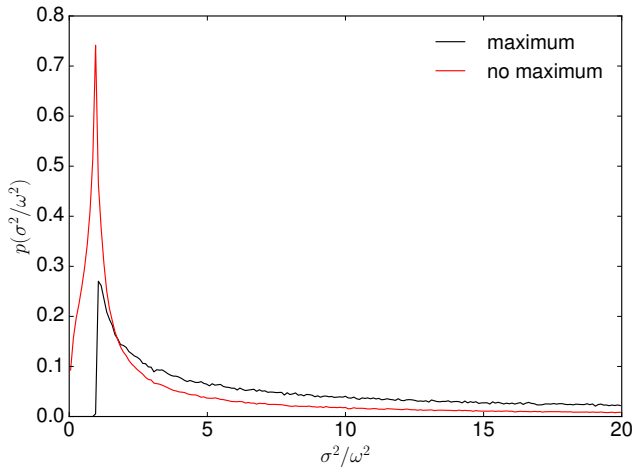

Figure 5.9: Distributions of the ratio of the two invariants σ^2 and ω^2. The red curve does not include the maximum constraint, i.e. $\lambda_i > 0$, while the black curve includes this constraint. Clearly the constraint moves all values which would have $\sigma^2 < \omega^2$ to values $\sigma^2 > \omega^2$ as it is expected from the analytical considerations made in Eq. (5.54). The smoothing length for the power spectrum is $R = 10\,\mathrm{Mpc}h^{-1}$.

Clearly, the positive definiteness of the Frobenius-norm implies that $\sigma^2 > \omega^2$ is fulfilled if $\langle \mathbf{I}\Psi, \Psi\mathbf{I}\rangle > 0$. Due to the cyclic property of the trace this term can be shown to be $\langle \mathbf{I}\Psi, \Psi\mathbf{I}\rangle = \mathrm{tr}(\mathbf{I}\Psi^2\mathbf{I}) = \mathrm{tr}(\mathbf{I}^2\Psi^2) = \langle \mathbf{I}^2, \Psi^2\rangle$, which in turn is positive for positive (semi-) definite matrices $\mathbf{I}$ and Ψ.

To show this, one can use the generalisation of the inequality of the arithmetic and geometric mean,

$$\frac{1}{n}\langle \mathbf{I}^2, \Psi^2\rangle = \frac{1}{n}\mathrm{tr}(\mathbf{I}^2\Psi^2) \geqslant (\det(\mathbf{I})\det(\Psi))^{\frac{2}{n}} \geqslant 0\,, \tag{5.55}$$

which is only valid for positive (semi-)definite matrices, with n being the dimension of the matrices. The tidal shear is positive definite at a peak of the density field, because $\mathrm{tr}(\Psi) = \Delta\Psi = \delta > 0$ due to the Poisson-equation, and the inertia can only sensibly be defined at a maximum of the density field, where the curvature of the density field assumes positive values, resulting in a positive definite inertia $\mathrm{tr}(\mathbf{I}) > 0$. The argumentation applies for the traceless shear as well, as a positive semi-definite matrix. Both determinants are positive for positive definite matrices, and constrain the scalar product $\langle \mathbf{I}^2, \Psi^2\rangle$ to be larger than zero. This is an important result, we find that the induced shear is always larger than the induced rotation by tidal torquing.

Figure 5.9 shows the effect mentioned in Eq. (5.54) very clearly: If we restrict the random process to maxima in the density field all values with $\sigma^2 < \omega^2$ disappear and get shifted to larger ratios of σ^2/ω^2. Thus, gravitational tidal fields will always introduce more shear than rotation by tidal torquing if only maxima of the underlying density field are considered. This is indeed a necessary condition, since otherwise the inertia tensor would not be defined in a proper way. As a consequence the collapse will always proceed faster in a scenario with tidal gravitational fields than in a uniform background as it is the case for the SPC. We show the, not normalized, joint distribution of σ^2 and δ in Figure 5.10. Due to the correlations in the y^n_{lm} basis

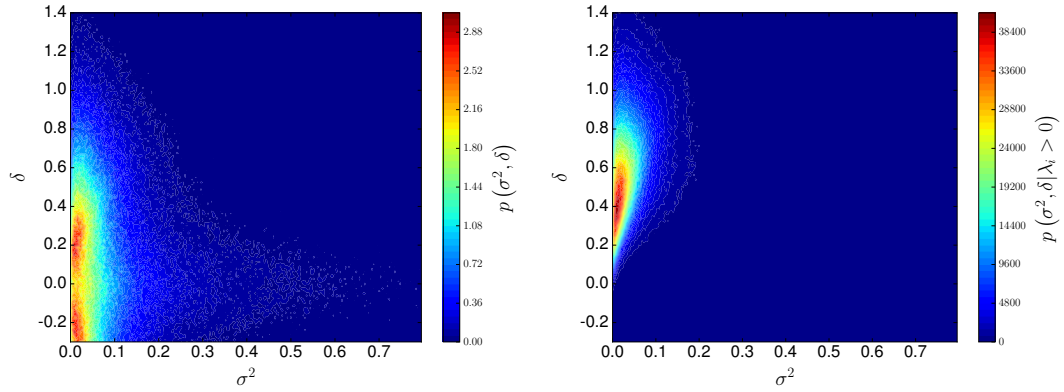

Figure 5.10: Joint distributions (not normalized) of the density contrast $\delta = \mathrm{tr}(\Psi)$ and the invariant σ^2. *Left panel*: No maximum constraint. The distribution is similar to the distribution found in Section 5.3. *Right panel*: The maximum constraint is imposed. Clearly the constraint enforces higher values of δ and thus also in σ^2, which is due to the correlations in the y^n_{lm} basis given in Eq. (5.17). The smoothing length for the power spectrum is $R = 10\,\mathrm{Mpch}^{-1}$.

given in Eq. (5.17), the maximum constraint enforces higher values in δ and σ^2. In particular, peaks can only be found if $\delta > 0$, which is indeed necessary to write down the inertia tensor as in Eq. (5.44), as the ellipsoid is a region with boundary $\delta = 0$. Also the density peaks are significantly higher than without the constraint.

In the left panel of Figure 5.11 we show the distribution of $\sigma^2 - \omega^2$ with different thresholds for the overdensity δ at the peak. Clearly, higher overdensities at the peak imply higher shear values as the potential is more curved at higher peaks.

5.9 INFLUENCE ON δ_c, Δ_V AND SCALING PROPERTIES

In this section we investigate the influence of the tidal gravitational fields on the collapse dynamics by substituting the invariants σ^2 and ω^2 into the collapse equation. Additionally we will study the scaling with the mass of the collapsed structure. The cosmology is chosen to be a concordance ΛCDM model with $\Omega_m = 0.3$, $\Omega_\Lambda = 0.7$, $w = -1$, $h = 0.7$, $\sigma_8 = 0.8$ and $n_s = 0.96$.

In the right panel of Figure 5.11 the resulting distribution of δ_c is shown. The collapse always proceeds faster than in the case without tidal fields. For more work on this we refer to Hoffman (1986); Zaroubi and Hoffman (1993); Bertschinger and Jain (1994). As discussed in the previous section, this is due to the fact that the tidal field induced shear is always higher than the effect due to tidal torquing, provided we restrict our considerations to maxima in the density field. Thus the strong drop of the distribution at higher δ_c marks the value which one would get within a uniform background.

Due to the faster collapse, virialised objects form more easily, thus yielding more massive objects. This effect is similar to modified gravities theories or dark energy cosmologies with non-phantom equations of state. Since the distribution found for δ_c is similar to the one found in Section 5.9 and no significant differences were found for more complex dark energy models. δ_c exhibits a mass dependence due to the low-pass filter with a scale R which is introduced to model the effective tidal fields acting

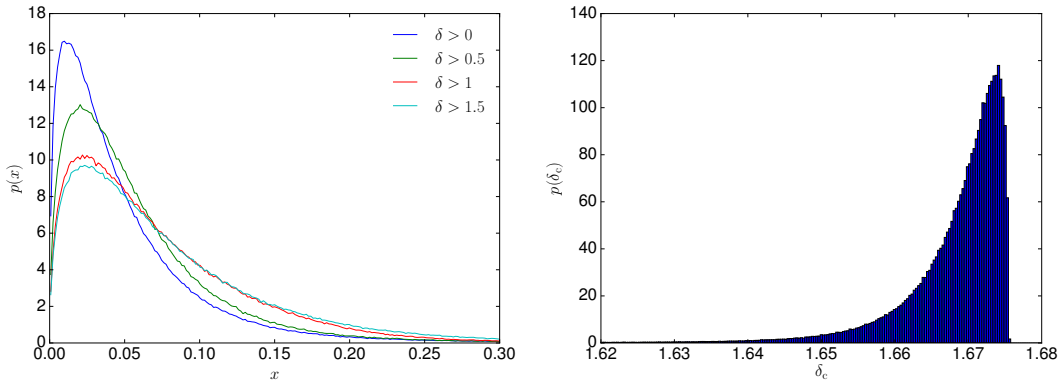

Figure 5.11: *Left*: Distributions of the invariants $\sigma^2 - \omega^2$ for different thresholds δ on a scale of $R = 10\,\mathrm{Mpc}h^{-1}$. Higher peaks induce higher values for $\sigma^2 - \omega^2$. *Right*: Distribution of the critical linear overdensity δ_c for a standard ΛCDM cosmology. The smoothing scale is again $R = 10\mathrm{Mpc}h^{-1}$ and the density threshold is $\delta = 0$.

on an object of size $R(M)$. We consider again the averaged values of the invariant $\sigma^2 - \omega^2$ or the linear critical density contrast from Eq. (5.22).

On the left panel in Figure 5.12 we show the scaling of $E[\sigma^2 - \omega^2]$ with respect to the mass. The general scaling shows that higher masses result into lower values for $\sigma^2 - \omega^2$ as larger objects are only influenced by low frequency modes which become smaller for increasing scale. In the case considered here we restrict ourselves to maxima in the density field, thus the situation is constructed such that the curvature of the density field must be negative, yielding slightly more shear on large scales than for a random point in the density field. On smaller scales, however, the situation is reversed. This argument is precisely due to the additional factor k^4 which enters in the random process for δ_{ij} (cf. Eqs. 5.15 and 5.42).

The right panel of Figure 5.12 shows the resulting scaling of $E[\delta_c]$. Here we additionally show the constant value (green curve) obtained without gravitational tidal fields. As for the invariants σ^2 and ω^2 the qualitative behaviour is identical. We find that the the term $\sigma^2 - \omega^2$ will always favour the collapse, thus lowering $E[\delta_c]$. Even though ω^2 will act against the collapse, as it corresponds to a centrifugal force, it can never dominate σ^2 as we showed before. Furthermore we note that the time evolution of the invariant is controlled by the time derivative of the growth factor introduced in Eq. (5.10) and is thus purely due to background dynamics. If one instead starts with a non-spherical collapse, one would find larger effects on δ_c compared to this idealised model. An example for this is the ellipsoidal collapse model (Eisenstein and Loeb, 1995; Ohta et al., 2003; 2004; Angrick and Bartelmann, 2010), where δ_c values are normally substantially higher than for the spherical collapse case, especially at low redshift and mass.

A very important and interesting quantity that can be evaluated within the framework of the spherical collapse model is the virial overdensity Δ_V, representing the overdensity of the collapsing object at the virialisation epoch (see also Meyer et al., 2012, for a discussion of this quantity in a general relativistic setting). The virial overdensity is also related to the size of spherically symmetric halos and its value can be inferred by embedding the virial theorem into the formalism. When includ-

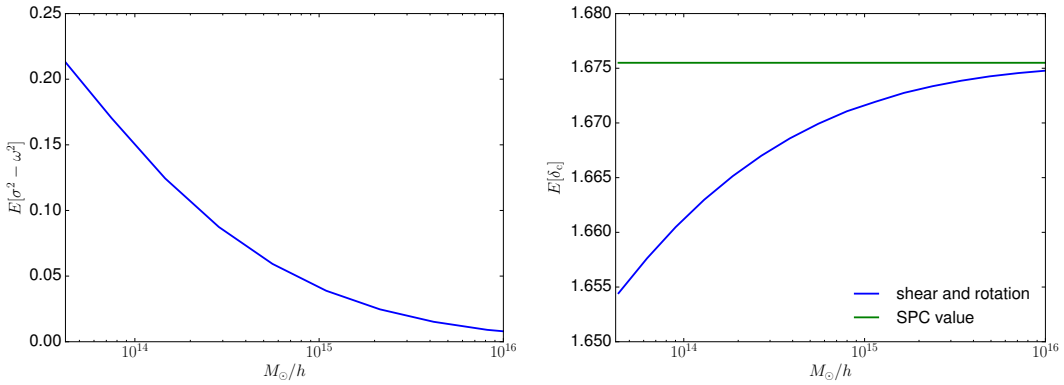

Figure 5.12: Scaling relations of averaged quantities with mass evaluated at redshift zero. The blue curve shows the effect derived in this paper by including both σ^2 and ω^2. The influence of gravitational tidal fields is highest for low masses, thus δ_c is also influenced most at the low-mass tail. *Left:* Averaged invariants, *Right:* averaged δ_c. The value for the SPC for a ΛCDM universe is shown in green.

ing the shear and the rotation terms into the equations of motion for dark matter perturbations, Δ_V becomes, in analogy to δ_c, mass-dependent. However, one finds that Δ_V is practically independent of mass and it evolves as if the system is evolving in a ideal background, i.e. without shear and rotation. This is an interesting result but not unexpected. As showed in Section 5.9, the virial overdensity is insensitive to mass since the quantities involved for its determination are evaluated still in the linear regime and perturbations with respect to the spherically symmetric case are of the order of per mill. Taking also into account that rotation has always a smaller contribution than the shear and their combined effect makes the rotating ellipsoid closer to the sphere in terms of the perturbation quantities, it is easy to understand why the feature found in Section 5.9 still holds.

5.10 CONCLUSION

In this chapter we investigated the influence of external tidal shear effects on the spherical collapse model using first order Lagrangian perturbation theory. The shear is evaluated directly from the statistics of the underlying density field in which the halo forms and therefore it does not need any further assumptions. Clearly, we cannot include direct vorticity generation with our formalism, as the rotation vanishes identically for a potential flow, however for the scales investigated the assumption of linear growth is still valid, implying that, even if initial vorticity was present it would decay as the halo forms. In this sense our ansatz for the shear is self-consistent.

We summarize our findings for this first part as follows:

1. External tidal shear supports the spherical collapse, which can be understood by noticing that virialized objects form in overdense regions in the first place. The effect is largest at small masses and low redshifts.

2. The effect on the important collapse parameter δ_c is of the percent level for both ΛCDM and more general dark energy models. Furthermore the influence on

the virial overdensity Δ_V is very small and it is nearly indistinguishable from a collapse without external shear. The reason for this is mainly that the virial overdensity is basically evaluated using the time at turn-around. At this time the evolution is only in the mildly non-linear regime, therefore shear effects are not important.

3. Gaining a mass dependence due to our formalism, the influence on the mass function is two-fold. At lower masses the linear term dominates the exponential, suppressing the occurrence of lighter objects. Furthermore the influence of δ_c is largest at high masses, as the exponential tail dominates there. However, the effect of shear on δ_c becomes smaller for higher masses. The mentioned effects leads to a change of the mass function of roughly 2%.

4. The mass dependence translates into differences also in the cumulative number counts. Tidal shear affects number counts of massive halos of only few percent when compared to the corresponding model without it. When compared to the ΛCDM model with tidal shear, results are qualitatively and quantitatively the same as without tidal shear.

5. Neglecting the shear in the estimation of cosmological parameters using number counts, e.g. in redshift space, can lead to 1σ biases on cosmological parameters such as Ω_m, σ_8, w_0 and w_a.

6. The bias in the cosmological parameters is such that the inferred σ_8 (Ω_m) is higher (lower) than without and a ΛCDM model results into a dynamical phantom model for $a \approx 1$. The increase in σ_8 is in the right direction to at least alleviate the tension between the power spectrum normalization at late and early times, even if the amount is not sufficient. Remember however, that we neglected the rotation contribution and this could either balance or strengthen the shear contribution. Also the resulting phantom model is in agreement with SNIa observations, but at this stage we cannot draw any firm conclusion.

7. Previous works on the extended spherical collapse model introduced the effect of shear and rotation with heuristically motivated models (Del Popolo et al., 2013a). In this model, both shear and rotation are combined into a single term that depends on mass and result into a modification of the Poisson term, but the rotation term has a predominant role with respect to the shear. While a direct comparison cannot be made, our approach has some points in common and some major differences. While both approaches lead to a mass dependent spherical collapse, we find that effects of the shear are at percent level, contrary to what found in previous works. This leads to the question of the importance of the rotation and of its effective modelization.

We then incorporated rotational effects induced by tidal torquing. By jointly considering the gravitational tidal field and the curvature of the density field we separated its action into a symmetric traceless part and an anti-symmetric part which correspond to the shear tensor and rotation tensor respectively. These tensors were used to construct the invariants σ^2 and ω^2 in the collapse equation. Physically, the protohalo, forming at the location of a peak, feels the surrounding tidal gravitational

field and thus shear effects as well as rotation induced by tidal torquing. Our findings are the following:

1. The invariant quantity ω^2 of the rotational part of the tidal tensor is always smaller than the shear invariant σ^2 within the framework of tidal torquing. This statement is not of statistical nature, it is true for every sample individually.

2. The critical linear overdensity δ_c is now a mass dependent quantity changing by roughly a percent with respect to the usual spherical collapse value. The overall effect is small at masses below $10^{15}\ M_\odot$ and completely negligible for masses above.

3. External tidal fields will always help objects to collapse into virialised structures even if a rotational term due to tidal torquing is considered. In terms of observations of cluster counts tidal fields can in principle always be confused with dynamical dark energy increasing the abundance of heavy clusters in a purely spherically symmetric case where no tidal fields are taken into account.

4. Comparing this work with a we find that the deviations of δ_c found there are mainly due to the rotational term, which can become rather large, thus the collapse is mostly slowed down. Our work finds an opposite result as the gravitational tidal fields always speed up the collapse and the rotational term is nearly negligible. This is, however, also a property of the model we used here. Our model is self-consistent in as long as we only consider external tidal effects on a spherically symmetric object where the deformation is negligible compared to the total extent of the collapsing object. In this work we assumed the halo to be non-spherical prior to collapse to allow it to spin up as long as the lever arms are large enough. As soon as collapse starts, the collapse is again treated as being spherical. We therefore have a situation in which a spherical overdensity is rotating at an angular speed ω^2 gained by tidal torquing as if it would have been an ellipsoidal object. These limitations make a direct comparison with a difficult. See point 5 for an explanation based on the way the invariant $\sigma^2 - \omega^2$ is evaluated.

5. In our self-consistent model, the shear and rotation term have little effect and their effect grows with time and mass as structures evolve. In the formalism outlined, the invariant $\sigma^2 - \omega^2$ is evaluated at early times when structures are in the linear regime. This explains why, for example, the virial overdensity Δ_V is barely affected. In previous works on the subject (a; b; Pace et al., 2014b) instead, the term $\sigma^2 - \omega^2$ assumes objects to be still spherical in average and that the rotation term matches the present-day rotational velocity of clusters as a function of their mass. This late time evaluation makes the rotation term ω^2 the dominant one.

6

PARAMETER INFERENCE AND MODIFIED GRAVITY WITH FUTURE COSMOLOGICAL SURVEYS

As discussed in Chapter 2, the ΛCDM model relies on the assumption that GR is the valid theory of gravity. The extensions to the standard model have been presented in Section 2.3 which can be divided into three classes: Dropping symmetry assumptions, including non-standard energy components or modifying the theory of gravity. In order to decide which model is preferred over another, theoretical predictions for different kinds of models have to be given and the parameters of the model have to be inferred. Thus one of the main goals of modern cosmology is parameter inference. More complicated cosmological models have a larger parameter space than the 6-dimensional ΛCDM space. If one keeps the FLRW symmetries but allows for varying DE and MG, the parameter space can increase substantially. Furthermore there are quite a few nuisance parameters, i.e. parameters which are not of direct physical interest. The inference process in cosmology is done by virtue of Bayes' theorem, that is, for data given a cosmological model and possibly some prior information one can construct the posterior distribution for the parameters and the best fit parameters are found using maximum likelihood methods. Since the amount of cosmological data is naturally limited, we can not expect to find an arbitrarily good estimator for each parameter. Nonetheless future surveys are expected to be dominated by systematic rather than by statistical errors. Therefore cosmology can now in principle serve as a test of gravity since there will be enough data to constrain the cosmological model and the theory of gravity at the same time.

In this chapter we will investigate the potential of future observations to pin down the theory of gravity for a very general class of scalar-tensor models, which mimic a DE component at the background level and whose perturbations can be parametrized at the linear level by four functions of time only. This class of theories describes a background model with a general time-varying DE component and an additional scalar field in the gravity sector. We will investigate the structure of the parameter space using MCMC and Fisher methods. Furthermore, we will briefly discuss the general structure of parameter spaces.

The contents of this chapter is prepared to be published in Reischke et al. (2018) (in preperation), while some ideas are also published in Spurio Mancini et al. (2018).

6.1 INTRODUCTION

GR is tested exquisitely on non-cosmological scales and in the weak field limit only (Berti et al., 2015) and more recently to be consistent with binary black hole merger (Abbott et al., 2016). Usually one assumes GR being valid also on cosmological scales, which might be a strong assumption and needs to be tested. Modifications of GR lead to very different phenomena (see Clifton et al., 2012, for a review, as well as Section 2.3) and influence the background expansion as well as the growth of structures. Furthermore, these models are highly degenerate with clustering dark energy models (Copeland et al., 2005), which can as well reproduce very different expansion histories and structure growth. This is already evident from the structure of the field equations of GR: modifications in the gravitational sector can be interpreted as a modification in the matter sector and can thus be treated as some kind of dark energy component (Battye and Pearson, 2012; 2013). Consequently, cosmological tests require exquisite data with high statistical significance in order to pin down the cosmological parameters well enough to be able to detect deviations from GR.

In the next decade we expect a huge step forward in large scale surveys dubbed stage IV experiments. These are in particular the EUCLID (Laureijs et al., 2011) mission for galaxy clustering and weak gravitational lensing, CMB experiments like ACTPOL (Thornton et al., 2016), the Square Kilometre Array (SKA) (Maartens et al., 2015) for intensity mapping, or the Large Synoptic Survey Telescope (LSST) as well as Wide-Field Infrared Survey Telescope (WFIRST). Operating at very different redshift and scales cross-correlation between those experiments will provide tons of information about the underlying gravity model. Additionally, these missions will also deliver tests of fundamental physics such as the mass scale of the neutrinos (Font-Ribera et al., 2014). This is of particular importance as the neutrino masses are highly degenerate with modifications of the gravity sector (Baldi et al., 2014; Baldi and Villaescusa-Navarro, 2016). Being very sensitive to the mass of the neutrinos, CMB experiments will yield complementary information to weak lensing surveys or galaxy clustering which are sensitive to the gravitational slip or the modified Poisson equation respectively.

Having a high dimensional parameter space, advanced sampling techniques are required even for forecasting to yield conservative errors on the cosmological parameters, since the Gaussian approximation of the posterior is valid only for the conditionalized case, but will certainly be wrong for the marginalised posterior distribution. We therefore study the structure of the posterior with MCMC methods as well as with a Fisher analysis. In particular, we investigate the constraining power of future experiments on modified gravity, including several other cosmological and nuisance parameters as well as neutrino masses. We focus on Horndeski theories of gravity first proposed by (Horndeski, 1974) and rediscovered by Nicolis et al. (2009) and Deffayet et al. (2011), which is the most general scalar-tensor theory of gravity in the sense that it has only one additional degree of freedom. The derivatives in the equation of motion are not higher than second order, which guarantees that the theory is ghost-free. There are theories which have higher order derivatives and no ghosts, these theories are called Beyond Horndeski (Langlois et al., 2017; Crisostomi and Koyama, 2017). To investigate these theories observationally, the observational probes need to cover a large range of spatial scales and should be sensitive on the

temporal evolution of the Universe. Here we will focus on CMB temperature and polarization anisotropies, weak gravitational lensing of the CMB, galaxy clustering and cosmic shear. The combination of these probes contains very powerful information on cosmological and gravitational parameters, especially when considering the cross-correlation between the different probes, since the evolution of the Universe is covered over a wide range.

The structure of this chapter is the following: In Section 6.2 we briefly review tensor-scalar theories of gravity and introduce the cosmological probes used in Section 6.3. Section 6.3 will introduce the necessary statistical tools which will be applied in Section 6.6. We end with general discussion on the structure of parameter spaces in Section 6.7 and a conclusion in Section 6.8.

6.2 TENSOR-SCALAR THEORIES OF GRAVITY

A general Lagrangian of a tensor-scalar theory was introduced in Eq. (2.50) in Section 2.3. The four functions G_j and K are in principle completely free and characterize the theory completely. Note that this theory is only minimally coupled to matter through the canonical volume form, extending this would go beyond Horndeski. In Bellini and Sawicki (2014) it was shown that the evolution of linear perturbations can be completely characterized by free functions depending on time only:

$$\begin{aligned}
M_*^2 =&\ 2\left(G_4 - 2XG_{4X} + XG_{5\phi} - \phi HXG_{5X}\right)\,,\\
HM_*^2\alpha_M \equiv&\ \frac{dM_*^2}{dt}\,,\\
H^2M_*^2\alpha_K \equiv&\ 2X\left(K_X + 2XK_{XX} - 2G_{3\phi} - 2XG_{3\phi}\right)\\
&+ 12\dot\phi XH\left(G_{3X} + XG_{3XX} - 3G_{4\phi X} - 2XG_{4\phi XX}\right)\\
&+ 12XH^2\left(G_{4X} + 8XG_{4XX} + 4X^2G_{4XXX}\right)\\
&- 12XH^2\left(G_{5X} + 5XG_{5\phi X} + 2X^2G_{5\phi XX}\right)\\
&+ 14\dot\phi H^3\left(3G_{5X} + 7XG_{5XX} + 2X^2G_{5XXX}\right)\,,\\
HM_*^2\alpha_B \equiv&\ 2\dot\phi\left(XG_{3X} - G_{4\phi} - 2XG_{4\phi X}\right)\\
&+ 8XH\left(G_{4X} + 2XG_{4XX} - G_{5\phi} - XG_{5\phi x}\right)\\
&+ 2\dot\phi XH^2\left(3G_{5X} + 2XG_{5XX}\right),\\
M_*^2\alpha_T \equiv&\ 2X\left(2G_{4X} - 2G_{5\phi} - (\ddot\phi - \dot\phi H)G_{5X}\right).
\end{aligned} \tag{6.1}$$

Here M_* is the Planck mass and α_M describes its time evolution, it has thus direct implications on the gravitational interaction via the Poisson equation. α_K describes the kinetic energy and is thus largely unconstrained by observations, since there is no direct influence on any observable. In contrast the braiding α_B describes how ϕ itself mixes with the scalar perturbations of the metric. Lastly α_T basically describes the propagation speed of tensorial modes and how it differs from normal null geodesics. Therefore both α_M and α_T affect the propagation of gravitational waves, they can be constrained rather well by non-cosmological experiments (e.g Lombriser and Taylor, 2015; Velten et al., 2017). Clearly, these functions restrict the evolution of perturba-

tions in scalar-tensor theories of gravity which can be parametrized by only a few numbers. The most obvious choice for a parametetrization would be

$$\alpha_i = \hat{\alpha}_i \Omega_{DE} + c_i \,, \tag{6.2}$$

since in such a way the modifications track the accelerated expansion of the Universe. Clearly this approach is idealized; however it gives us a good idea what can be learned from data in these very general models. For a more detailed discussion on these topics we refer to Linder et al. (2016) and Alonso et al. (2017). In Newtonian gauge, the linear perturbation equations in Fourier space are given by

$$k^2 \Phi_k = -\frac{3H_0^2 \Omega_m}{2a} \delta_k \mu(k, a) \tag{6.3}$$

and

$$\frac{\Phi_k}{\Psi_k} = \gamma(k, a) \,. \tag{6.4}$$

Many theories of MG are equipped with a screening mechanism which allow a scale dependence of the modifications so that at small scales or high density regions GR is recovered (Joyce et al., 2015). This mainly helps the theories to survive local tests of gravity in the solar system. Screening effects become important at small cosmological scales, such that the effect of modified gravity is suppressed (Barreira et al., 2013; Li et al., 2013; Winther et al., 2015). So far non-linear structure formation in MG scenarios has only been done for very specific models, but not for such a general class as the Horndeski theories. Even though a lot of the theories covered by the Horndeski class have an effective screening mechanism, it is only present at the linear level. Here we will use linear predictions and then apply the halo model correction to the predicted linear power spectrum. In particular, we use `Halofit` (Takahashi et al., 2012) which is only valid in cosmologies with GR. Therefore we have to choose a screening scale artificially to make sure that the modifications of GR are negligible on non-linear scales. We impose the following scale, k_s, on the alpha function (Alonso et al., 2017):

$$\alpha_i \to \alpha_i \exp\left[\left(-\frac{k}{2k_s}\right)^2\right] . \tag{6.5}$$

In Section 6.3.1 we will discuss the problem of structure growth in slightly more detail. It should also be noted that Eq. (6.5) is not a self-consistent way of describing the screening mechanism since also small modes can contribute to the non-linear power.s

6.3 COSMOLOGICAL PROBES

The cosmological data is structured in terms of spherical harmonic coefficients, $\{a^X_{\ell m}\}$, where X labels the considered data. Here we consider data from CMB primary anisotropies, i.e. temperature fluctuations and the fluctuation in the two polarization modes (see Section 3.1 for more details), furthermore we also consider weak gravitational lensing of the CMB as introduced in Section 3.2.2, we label them T, E, B and

D, respectively. These probes are then combined with tomographic galaxy clustering as well as cosmic shear labelled g_i and γ_i respectively. The statistics of the modes $a^X_{\ell m}$ is described by their angular power spectra. As modes of different data sets are not independent, the cross-spectra are non-zero and carry valuable cosmological information. In this section we will discuss all relevant spectra together with their respective noise properties. Throughout this section we will always use the Limber projection (Limber, 1953) which is valid for $\ell > 10$ (Kitching et al., 2017).

6.3.1 *Structure growth*

Ultimately all probes discussed here depend on the statistics of the cosmic density field and, as outlined in Section 2.3 MG, mainly influences the growth of structures, i.e. the metric perturbations. For evolving the linear perturbations we use the Boltzmann code `HiCLASS` (Zumalacarregui et al., 2016), which is an extension of `CLASS` (Lesgourgues, 2011) for tensor-scalar theories of gravity. The code evolves initial conditions set by inflation forward in time using linear equations only. At small scales and low redshifts the perturbations become non-linear. On these scales the treatment of the Boltzmann codes breaks down. For the CMB primary anisotropies this effect is small, since the only non-linear contributions come from the integrated Sachs-Wolfe (iSW) effect which has most of its power at large scales. On the contrary cosmic shear and galaxy clustering will get a lot of their signal from non-linear scales in future surveys. It is therefore necessary to model the non-linear scales carefully to exploit the full power of future surveys. A lot of effort has been put into understanding the non-linear evolution theoretically in standard cosmological models (e.g Zel'Dovich, 1970; Buchert, 1992; Bouchet et al., 1995; Bernardeau et al., 2002; Cooray and Sheth, 2002; Hilbert et al., 2011; Bartelmann et al., 2014; Bartelmann et al., 2017, for analytical modelling), (e.g. Smith et al., 2003; Heitmann et al., 2010, for simulations). In MGtheories, structure non-linear models are more difficult due to the modified Poisson equation and so far no common description of non-linear scales exists in general tensor-scalar theories (we refer e.g. to Hu and Sawicki, 2007; Zhao et al., 2011; Casas et al., 2017).

In this work we take care of non-linearities by using the Halofit model (Smith et al., 2003; Takahashi et al., 2012). It is thus assumed that the effect of MG is negligible on small scales and that GR yields an adequate description (Hu and Sawicki, 2007). For Horndeski theories this is not true in general, since there is no screening evolved. It is therefore necessary to include the screening by hand as in Eq. (6.5), this effectively amounts to

$$\begin{aligned} \mu(k,a) &\to \mu_{GR} + \mu_{MG}(a,k)W(k;k_s) \\ \gamma(k,a) &\to \gamma_{GR} + \gamma_{MG}(a,k)W(k;k_s) \\ D_+(k,a) &\to D_{+GR}(a) + D_{+MG}(a,k)W(k;k_s)\,. \end{aligned} \tag{6.6}$$

Here $W(k,k_s) \propto \exp(-(k/k_s)^2)$ is a low-pass filter to ensure that on scales $k > k_s$ GR is recovered. A usual value for the screening scale would be $k_s \approx 0.1h/\mathrm{Mpc}$. The GR limits of μ and γ are unity, while we recover the linear growth factor from

$$\frac{d^2}{da^2}D_+(a) + \frac{1}{a}\left(3 + \frac{d\ln H}{d\ln a}\right)\frac{d}{da}D_+(a) - \frac{3}{2a^2}\Omega_m(a)D_+(a) = 0. \tag{6.7}$$

Thus our procedure works like this: We obtain the linear power spectra for the perturbed variables, i.e. Ψ, Φ and δ, which are related via γ and μ, from `HiCLASS`:

$$P_{\rm lin}(k, a) = D_+(k, a) P_{\rm lin}(k, a = 1). \tag{6.8}$$

We then apply the non-linear transfer function obtained by `Halofit` to model the corresponding non-linear spectra $P(k, a)$. In the rest of this section we will discuss the cosmological probes used in our analysis. Note that Eq. (6.6) and (6.7) show the screening effect only illustratively and Eq. (6.5) describes the full treatment. Nonetheless, this screening is still purely phenomenological and is treated as a nuisance parameter in the analysis.

Additional uncertainties on non-linear scales are due to baryonic effects such as feedback processes. Even accurate emulators build from suites of numerical simulation depend strongly on baryonic physics models (Rudd et al., 2008; Daalen et al., 2011; 2014; Hellwing et al., 2016). A model to describe those uncertainties has been proposed in Schneider and Teyssier (2015) on the basis of different feedback models. A power spectrum from a DM only simulation, $P_{\rm DMO}$ is compared to a power spectrum including baryonic physics, $P_{\rm BCM}$ yielding a fitting function:

$$F(k, z) := \frac{P_{\rm BCM}}{P_{\rm DMO}} = G(k|M_c, \eta_b, z) S(k|k_s) \,, \tag{6.9}$$

where S describes the small-scale increase of the power due the central galaxy stars while G describes suppression due to gas. The effect of S stays sub-dominant up to $k \approx 10\ \mathrm{Mpc}\ h^{-1}$ and is therefore not considered here. We will marginalize over the free parameters η_b and M_c which describe the ejection radius of gas from halos as a function of their virial radius and the typical mass scale of a halo respectively.

6.3.2 *CMB*

Maps of the CMB temperature and polarization contain various kinds of primary anisotropies which are related to the potential landscape at the last scattering surface as shown in Section 3.1. Foregrounds induce secondary anisotropies, which can be removed very well as they destroy the thermal CMB spectrum. The cleansed maps of CMB data are given in spherical harmonics of $P = T, E, B$ with some instrumental noise n, with root mean square σ_P^2

$$a^P_{\ell m} = s^P_{\ell m} + n^P_{\ell m} \,. \tag{6.10}$$

The noise can be modelled by a Gaussian beam with width $\theta_{\rm beam}$ and white noise, yielding a noise power spectrum of the form

$$N^P(\ell) \equiv \langle n^{P*}_{\ell m} n^{P'}_{\ell m} \rangle = \theta^2_{\rm beam} \sigma^2_P \exp\left(\ell(\ell+1) \frac{\theta^2_{\rm beam}}{8 \ln 2} \right) \delta_{PP'} \,, \tag{6.11}$$

diagonal in P as the noise of different maps is uncorrelated. Effectively this describes the spectrum of a map containing instrumental noise and resolution. Consequently, the angular power spectrum is given by

$$\langle a^{P*}_{\ell m} a^{P'}_{\ell' m'} \rangle \equiv \hat{C}^{PP'}(\ell) = \left(C^{PP'}(\ell) + N^P(\ell) \right) \delta_{\ell\ell'} \delta_{mm'} \,. \tag{6.12}$$

Stage III CMB experiments such as Wilkinson Microwave Anisotropy Probe (WMAP) (Hinshaw et al., 2013) or Planck (Planck Collaboration XIII, 2015) will eventually be surpassed by Stage IV CMB experiments (Abazajian et al., 2016; Thornton et al., 2016) and will have a very small instrumental noise which allows for measurements up to $\ell \sim 3000$ especially for the polarization maps. The actual form of the angular power spectra $C^{PP'}(\ell)$ is only available numerically, but the basic features have been discussed in Section 3.1 and we refer to Figure 3.1. The strongest effect from MG is due to the iSW effect at low ℓ which is due to time-evolving potentials in the LSS.

The CMB signal is additionally lensed by the LSS as described in Section 3.2.2. Being released at a redshift of roughly 1100, the lensing signal of the CMB carries a lot of cosmological information. Having no access to the unlensed CMB one has to use the inhomogeneity of the lensed CMB, since the lensing effect shuffles the observed patches of the CMB and thus mixes different angular scales. This way lensing signal can be constructed in a minimal variance and unbiased way

$$\hat{C}_{\kappa_{CMB}\kappa_{CMB}} = C_{\kappa_{CMB}\kappa_{CMB}} + N_{\kappa_{CMB}}, \tag{6.13}$$

with the noise term from the quadratic estimator from Hu and Okamoto (2002); Okamoto and Hu (2003). Even with future experiments the noise will start dominating at multipoles well below 1000. Thus the main contribution to the lensing signal comes from linear structures which preserve the Gaussian structure.

6.3.3 *Cosmic shear*

We generalize the weak lensing of the LSS introduced in Section 3.2 by explicitly writing down the lensing potential in term of the two Bardeen potentials:

$$C_{\psi_i\psi_j} = \int_0^{\chi_H} \frac{d\chi}{\chi^2} W_i(\chi) W_j(\chi) P_{\Phi+\Psi}(\ell/\chi, \chi). \tag{6.14}$$

Here we defined the power spectrum of the the sum of the two Bardeen potentials Φ and Ψ. The convergence spectra is related to the lensing potential spectra via the Poisson equation $\Delta\psi = 2\kappa$, yielding

$$C_{\kappa_i\kappa_j} = \frac{\ell^4}{4} C_{\psi_i\psi_j}\,, \tag{6.15}$$

which in the case of GR reduces to the form in Eq. (3.30). If deviations from GR are present the differences in the two Bardeen potentials and the modified Poisson equation will yield a different lensing signal even if the background evolution is the same.

There is one aspect of cosmic shear we have not discussed so far, when calculating the two-point correlation function, one implicitly assumes that galaxy shapes are intrinsically uncorrelated and only the auto-correlation plays a major role (ignoring cosmic variance) which in turn yields the observational Poisson noise. This assumption is, however, not true since physically nearby galaxies feel correlated potentials and thus their shapes are correlated due to tidal interactions with the ambient LSS (e.g. Heavens et al., 2000; Croft and Metzler, 2000; Catelan et al., 2001; Mackey et al., 2002; Jing, 2002; Forero-Romero et al., 2014; Joachimi et al., 2015; Kiessling et al.,

2015; Kirk et al., 2015; Blazek et al., 2012; 2017; Tugendhat and Schaefer, 2017). There are two basic types of alignments, II and GI, namely the correlation of the intrinsic ellipticity with itself and the correlation of the lensing signal with the intrinsic ellipticity respectively. Both quantities are present in observed ellipticity spectra, which would ideally be interpreted as being proportional to the cosmic shear signal only. Intrinsic alignments are only a few percent of the lensing signal depending on the angular scale considered. But due to the high statistical significance with which cosmic shear is measured by stage IV surveys, the impact on the inference process is dramatically. In this chapter we will ignore the effect of intrinsic alignments and assume that we are given a clean cosmic shear signal. Including intrinsic alignments will increase the errors on cosmological parameters, since all models have at least one free amplitude which has to be determined by the data.

6.3.4 *Galaxy clustering*

Contrary to cosmic shear galaxy, clustering does not measure the statistics of the gravitational potential, but of the density contrast δ (see Section 3.3). Therefore, expression (3.35) does not need to be modified. The weight function is given by:

$$W_{g_i}(\ell/\chi, \chi) = \frac{H(\chi)}{c} b(\ell/\chi, \chi) p(\chi) \quad \text{if} \quad \chi \in [\chi_i, \chi_{i+1}) \, . \tag{6.16}$$

With this definition there is no cross correlation between different tomographic bins in a galaxy survey. This assumption is not completely true since there can be a non-vanishing cross-correlation for example due to low k perturbations which range over different redshift bins (Bailoni et al., 2017). This effect, however, is small compared to the actual spectrum, since the overlap of the weight functions is small for $i \neq j$. For the galaxy bias we assume a simple linear model with no scale dependence (Ferraro et al., 2015):

$$b(\chi) = b_0(1 + z(\chi)) \, . \tag{6.17}$$

This model has no physical motivation but reflects the fact that the bias increases with redshift, which stems from the fact that galaxy clustering stays approximately constant at low redshifts (Kauffmann et al., 1999a; b) while the dark matter evolves. More complicated models could be implemented easily and would increase the errors on the cosmological parameters. Finally, the observed spectra again suffers from Poissonian noise:

$$\hat{C}_{g_i g_j} = C_{g_i g_j} + \frac{n_{\text{bin}}}{\bar{n}} \delta_{ij} \, . \tag{6.18}$$

6.3.5 *Cross-correlation*

The probes presented so far could be used individually, i.e. one could for example constrain cosmological parameters using CMB and repeat the same exercise for a cosmic shear experiment and multiplying the two posterior distributions to find the joint posterior of both experiments. However, since all probes are linked to the statistics of the density contrast, δ, they are correlated, cross-correlations only vanish

if the correlation length of the two different probes do not overlap. The different spectra satisfy the Cauchy-Schwarz inequality, which we will discuss in more detail in Section 6.4.

Firstly, there exists an obvious cross-correlation between galaxy clustering and cosmic shear:

$$C_{g_i\psi_j}(\ell) = \int_0^{\chi_H} \frac{d\chi}{\chi^2} W_{g_i}(\ell/\chi, \chi) W_{\psi_j}(\ell/\chi) P_{\delta,\Phi+\Psi}(\ell/\chi, \chi). \tag{6.19}$$

Here we defined the cross correlation power spectrum of the density fluctuations with the sum over the two Bardeen potentials. As in the case of cosmic shear, we could also rewrite Eq. (6.19) so that it only contains P_δ by using the ratio between Ψ and Φ, as well as the modified Poisson equation. Since the same galaxies are used to measure g_i and ψ_j there exists also a noise term in this case:

$$\hat{C}_{g_i\psi_j}(\ell) = C_{g_i\psi_j}(\ell) + \frac{\sigma_\epsilon n_{bin}}{\bar{n}} \delta_{ij} \, . \tag{6.20}$$

Secondly, the lensing signal of the CMB is cross-correlated with cosmic shear and galaxy clustering. Let χ_* be the comoving distance to the last scattering surface, the lensing signal of the CMB is just

$$\psi_{CMB} = \int_0^{\chi_H} d\chi W_{CMB}(\Phi + \Psi) \, , \tag{6.21}$$

with the CMB lensing efficiency function

$$W_{CMB}(\chi) = \frac{\chi_* - \chi}{\chi_*} \frac{H(\chi)}{ca} \, . \tag{6.22}$$

Angular power spectra for the cross-correlation between galaxy clustering and CMB lensing are then given by

$$C_{g_i\psi_{CMB}}(\ell) = \int \frac{d\chi}{\chi^2} W_{g_i} W_{\psi_{CMB}} P_{\delta,\Phi+\Psi}(\ell/\chi, \chi) \, , \tag{6.23}$$

and similarly for

$$C_{\psi_i\psi_{CMB}}(\ell) = \int \frac{d\chi}{\chi^2} W_{\psi_i} W_{\psi_{CMB}} P_{\Phi+\Psi}(\ell/\chi, \chi) \, . \tag{6.24}$$

Lastly, cosmic shear and galaxy clustering are correlated with the temperature fluctuations of the CMB via the iSW effect as discussed in Section 3.1, which is of particular interest for MG. The weight function of the iSW effect is given by

$$W_{iSW}(k, a) = \frac{3}{2\chi_H^3} a^2 E(a) F'(k, a) \, , \tag{6.25}$$

where the prime denotes a derivative with respect to a and

$$F(k, a) = \mu(k, a) \frac{D_+(k, a)}{a} \left(1 + \frac{1}{\gamma(k, a)}\right) \, . \tag{6.26}$$

We obtain the cross spectra as

$$C_{g_iT}(\ell) = \int \frac{d\chi}{\chi^2} W_{g_i} W_{iSW} D_+(\ell/\chi, \chi) \frac{P_\delta(\ell/\chi)}{k^2} \, , \tag{6.27}$$

and with W_{g_i} replaced by W_{ψ_i} for C_{ψ_iT}. In Figure 6.1 we show all cross-correlations presented in this section.

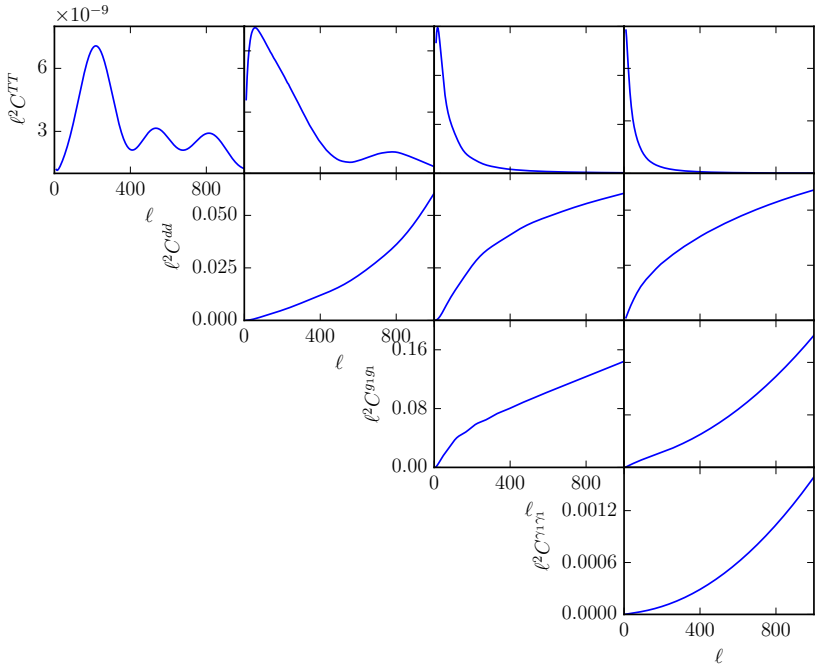

Figure 6.1: On the diagonal the auto-correlations of the temperature anisotropy, the CMB-lensing convergence, galaxy clustering and cosmic shear are shown. The off-diagonal plots show the corresponding cross-spectra, e.g. the second plot in the first row shows the Td cross-correlation. Six tomographic bins where used and the ones considered here are shown and the one used for g and γ is the first one, i.e. the one with the lowest redshift. Observational noise is added to the spectra. Note that the y-range for the off-diagonal plots is not the same as for the ones on the diagonal.

6.4 STATISTICS

Having introduced the different probes, we now bundle them in a random vector $\mathbf{a}_{\ell m}$.

$$\mathbf{a}^{\dagger}_{\ell m} \coloneqq \left(a^{*T}_{\ell m}, a^{*E}_{\ell m}, a^{*B}_{\ell m}, a^{*\kappa_{CMB}}_{\ell m}, a^{*g_1}_{\ell m}, ..., a^{*g_n}_{\ell m}, a^{*\kappa_1}_{\ell m}, ..., a^{*\kappa_n}_{\ell m}\right) , \tag{6.28}$$

where n is the number of tomographic bins. The statistics of the modes is described by the covariance matrix $\mathbf{C}_{\mathbf{a}}(\ell)$:

$$\mathbf{C}_{\mathbf{a}}(\ell) \coloneqq \langle \mathbf{a}_{\ell m} \mathbf{a}^{\dagger}_{\ell m} \rangle , \tag{6.29}$$

which does not depend on the polar multipole number m due to statistical isotropy, furthermore angular brackets denote an ensemble average over all possible realiza-

tions of the data. If the data is arranged as described in Eq. (6.28), we can give $\mathbf{C}_a(\ell)$ explicitly:

$$\mathbf{C}_a(\ell) = \begin{pmatrix} TT & TE & TB & Td & Tg_1 & \dots & Tg_n & T\gamma_1 & \dots & T\gamma_n \\ ET & EE & EB & Ed & Eg_1 & \dots & Eg_n & E\gamma_1 & \dots & ET\gamma_n \\ BT & BE & BB & Bd & Bg_1 & \dots & Bg_n & B\gamma_1 & \dots & B\gamma_n \\ BT & BE & BB & Bd & Bg_1 & \dots & Bg_n & B\gamma_1 & \dots & B\gamma_n \\ dT & dE & dB & dd & dg_1 & \dots & dg_n & d\gamma_1 & \dots & d\gamma_n \\ g_1T & g_1E & g_1B & g_1d & g_1g_1 & \dots & g_1g_n & g_1\gamma_1 & \dots & g_1\gamma_n \\ \vdots & \vdots & \vdots & \vdots & \vdots & \ddots & \dots & \vdots & \ddots & \vdots \\ g_nT & g_nE & g_nB & g_nd & g_ng_n & \dots & g_ng_1 & g_n\gamma_n & \dots & g_n\gamma_n \\ \gamma_1T & \gamma_1E & \gamma_1B & \gamma_1d & \gamma_1g_1 & \dots & \gamma_1g_n & \gamma_1\gamma_n & \dots & \gamma_1\gamma_n \\ \vdots & \vdots & \vdots & \vdots & \vdots & \ddots & \dots & \vdots & \ddots & \vdots \\ \gamma_nT & \gamma_nE & \gamma_nB & \gamma_nd & \gamma_ng_n & \dots & \gamma_ng_n & \gamma_n\gamma_1 & \dots & \gamma_n\gamma_n \end{pmatrix} \tag{6.30}$$

Here we used the following shorthand notation $TT \equiv \langle TT \rangle$ and similarly for all other correlations. If the modes belong to a certain model described by the covariance $\mathbf{C}_a(\ell)$, we define the likelihood

$$\mathcal{L}(\{\mathbf{a}_{\ell m}\}) = \prod_\ell p\left[\mathbf{a}_{\ell m}|\mathbf{C}_a(\ell)\right]^{2\ell+1}, \tag{6.31}$$

where we made use of statistical homogeneity and isotropy since the ℓ modes are mutually independent and $2\ell+1$ modes contribute to each ℓ respectively. For a single mode, ℓ the Gaussian probability is given by

$$p\left[\mathbf{a}_{\ell m}|\mathbf{C}_a(\ell)\right] = \frac{1}{\sqrt{(2\pi)^N \det \mathbf{C}_a(\ell)}} \exp\left[-\frac{1}{2}\mathbf{a}^\dagger_{\ell m}\mathbf{C}_a^{-1}(\ell)\mathbf{a}_{\ell m}\right], \tag{6.32}$$

here N is the dimension of the vector $\mathbf{a}_{\ell m}$, which, in our case, is $4+2n$. It is clear that the covariance, $\mathbf{C}_a$ must be a positive definite matrix in order to allow for a probabilistic interpretation of Eq. (6.32). This is ensured by the Cauchy-Schwarz inequality:

$$C_{XX}C_{YY} \geqslant C_{XY}^2 . \tag{6.33}$$

It should furthermore be noted that Eq. (6.32) is an assumption which will certainly break down for high multipoles, ℓ and low redshifts, z, due to non-linear clustering. When comparing the theoretical predictions to real data, this effect must incorporated to avoid under-estimation of errors or biases. The problem is of course that one does not know, other than Gaussian, how the distribution of the modes looks like. As described at the beginning of Chapter 5, one could expand Eq. (6.32) into an Edgeworth series. However, it would not be clear where to stop the expansion (Sellentin et al., 2017a). Thus in reality Eq. (6.32) is only valid for sufficiently low ℓ. The Gaussianity is, however, slightly restored by the broad integration kernels of the weight functions amounting for a superposition of different modes and therefore enhance the Gaussianity thanks to the central limit theorem.

A way out of this is to consider the power in different multipole bins as a random variable. Since one adds up $2\ell+1$ modes for each multipole, the distribution is very close to Gaussian for higher ℓ. This has the advantage that one can describe the data, i.e. the likelihood with a Gaussian distribution very well. At the same time the covariances are now products of power spectra and therefore four-point functions of the density field as described in Chapter 4. This increases the difficulty of the evaluation of the likelihood dramatically as non-linear clustering amounts for higher order cumulants. Nonetheless, this approach is way cleaner than the one in Eq. (6.32), since it does not have to rely on the one-point statistic, where the full distribution must be known. It was, however, also shown by Sellentin and Heavens (2016); Sellentin et al. (2017b) that problems at small multipoles arise with this procedure, since the power spectrum estimator is Γ distributed, which becomes Gaussian only for high ℓ. In this sense, the two approaches suffer from non-Gaussianities at opposite ends of the multipole range.

Another effect is the difference between adding to data sets and combining them properly (Kitching et al., 2015; Merkel and Schäfer, 2017). This effect is subtle: the non-vanishing correlations leads to a decreasing signal, compared to measurements which are independent. However, as said before, the model has to explain those correlations as well, possibly yielding a larger constraining power. It is thus necessary to include all correlations, since ignoring them would pretend that the measurements are independent or that a model is fitted in which the correlation is vanishing.

We now take the logarithmic likelihood $L = -2\ln\mathcal{L}$ and bring it into the following form

$$L = \sum_\ell (2\ell+1)\left[\ln\left(\det\mathbf{C}_a(\ell)\right) + \mathbf{a}^\dagger_{\ell m}\mathbf{C}_a^{-1}(\ell)\mathbf{a}_{\ell m}\right] , \tag{6.34}$$

up to an arbitrary additive constant. Averaging over the data yields omitting the dependence on cosmological parameters θ of covariance matrix:

$$\langle L\rangle(\theta) = \sum_\ell (2\ell+1)\left[\ln\left(\det\mathbf{C}_a\right) + \mathrm{tr}(\mathbf{C}_a^{-1}\hat{\mathbf{C}}_a)\right] , \tag{6.35}$$

where $\hat{\mathbf{C}}_a = \langle \mathbf{a}_{\ell m}\mathbf{a}^\dagger_{\ell m}\rangle$ is the covariance matrix of the data, i.e. it is evaluated at the fiducial cosmology in case of forecasting.

Bayes' theorem relates the likelihood to the posterior:

$$p(\theta|\mathbf{D}) = \frac{p(\mathbf{D}|\theta)p(\theta)}{p(\mathbf{D})} , \tag{6.36}$$

where θ are the parameters, $\mathbf{D}$ the data $p(\theta)$ the prior and $p(\mathbf{D})$ the evidence. The latter is in principle just a normalization constant since the posterior $p(\theta|\mathbf{D})$ is a probability density. Thus, the posterior equals the likelihood for a uniform prior up to a normalization constant. If the parameter space itself is constrained, for example due to physical requirements, a flat prior is not always the optimal choice (Hannestad and Tram, 2017).

The log-likelihood (6.35) can now be interpreted as the logarithm of the posterior and the value of θ, where $\langle L\rangle$ peaks marks the best fit point, i.e. the maximum likelihood estimator $\hat{\theta}$. Consequently, $\langle L\rangle(\theta)$ just needs to be evaluated across the parameter space to find $\hat{\theta}$. This, however, can be computationally very challenging

since the evaluation of $\langle L \rangle(\theta)$ will take a certain amount of time and the number of necessary evaluations increases strongly with the number of model parameters. To avoid this problem there are two possibilities: (i) if one is only interested in forecasting, $\hat{\theta}$ is known and one can expand $\langle L \rangle(\theta)$ around its maximum; (ii) for parameter inference one would use MCMC to find $\hat{\theta}$ and the corresponding errors.

Let us first approximate $\langle L \rangle(\theta)$:

$$\langle L \rangle(\theta) = \langle L \rangle(\hat{\theta}) + \frac{1}{2} \frac{\partial^2 \langle L \rangle}{\partial \theta_i \partial \theta_j} \bigg|_{\theta=\hat{\theta}} (\theta - \hat{\theta})_i (\theta - \hat{\theta})_j + \dots , \tag{6.37}$$

where the first term is an arbitrary constant. The first order term of the Taylor series

Table 3: Survey characteristics for a stage IV experiment described in Section 6.5. The sky coverage is assumed to be equal for all probes. Tomographic redshift bins are chosen to have same statistical weight, thus they are not equidistant in redshift.

$\Omega_{\rm survey}[{\rm deg}^2]$	$\ell_{\rm min}$	$\ell_{\rm max,LSS}$	$\ell_{\rm max,CMB}$	$\bar{n}[{\rm arcmin}^{-2}]$	$n_{\rm bin}$
15000	10	2000	5000	30	6

vanishes since it is evaluated at an extrema. If the expansion is stopped at the second order, the posterior resembles the shape of a Gaussian, since its log-likelihood is a quadratic form, using also additional terms was discussed in Sellentin (2015). The quantity

$$F^{ij} = \left\langle \frac{\partial^2 L}{\partial \theta_i \partial \theta_j} \right\rangle \bigg|_{\theta=\hat{\theta}} , \tag{6.38}$$

is called the Fisher matrix and for Gaussian data as in Eq. (6.32), it can be calculated to be (Tegmark et al., 1997):

$$F_{ij} = \frac{1}{2} \sum_{\ell=\ell_{\rm min}}^{\ell_{\rm max}} (2\ell+1) {\rm tr} \left(\partial_i {\rm ln}[\mathbf{C}_\alpha(\ell)] \partial_j {\rm ln}[\mathbf{C}_\alpha(\ell)] \right) . \tag{6.39}$$

The Fisher matrix satisfies the Cramér-Rao bound:

$$\mathbf{V} \geqslant \frac{1}{\mathcal{N}} \mathbf{F}^{-1} , \tag{6.40}$$

where $\mathcal{N}$ is the number of independent data and $\mathbf{V}$ is the error covariance matrix:

$$V_{ij} = \mathrm{E} \left[(\theta_i - \hat{\theta}_i)(\theta_j - \hat{\theta}_j) \right] . \tag{6.41}$$

Thus, the errors obtained from a Fisher matrix forecast are always lower bounds on the achievable errors. The equality holds if the posterior is indeed exactly Gaussian. Furthermore, the maximum likelihood estimator is Fisher efficient meaning that it asymptotically satisfies

$$\mathbf{V}_{\rm MLE} = \frac{1}{\mathcal{N}} \mathbf{F}^{-1} + \mathcal{O}(\mathcal{N}^{-2}) . \tag{6.42}$$

Here, the second term describes the higher order asymptotic behaviour. Note again that this last discussion is not of Bayesian nature, however, the asymptotic behaviour including any regular prior is the same.

The Fisher matrix in its form (6.39) can also be used to define the signal-to-noise for a measurement for which we assume the following model schematically:

$$C = AS + N \,, \tag{6.43}$$

where A is the amplitude which serves as a parameter. Using Eq. (6.39) one finds that cumulative signal-to-noise is given by

$$\Sigma^2(\leqslant \ell) = \sum_{\ell'=\ell_{\min}}^{\ell} \frac{2\ell'+1}{2} \mathrm{tr}\left[\mathbf{C}_{\ell'}^{-1}\mathbf{S}_{\ell'}\mathbf{C}_{\ell'}^{-1}\mathbf{S}_{\ell'}\right] \,, \tag{6.44}$$

where $\mathbf{S}_{\ell'}$ is the covariance without the noise.

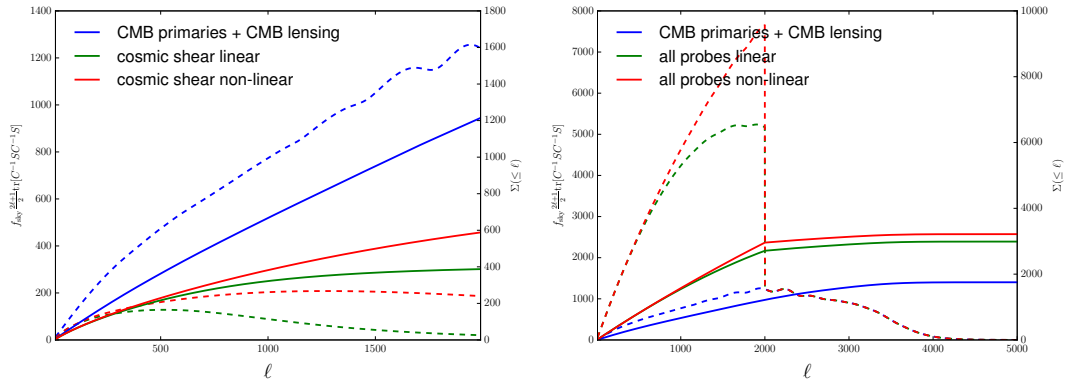

Figure 6.2: Differential (dashed lines) and cumulative (solid lines) signal-to-noise ratio for different probes for stage IV experiments. *Left*: Multipole range for cosmic shear. *Right*: full multipole range.

For what was done so far we always assumed that the modes $a_{\ell m}$ form a complete and orthogonal basis for the field, the sky, we observe. Since we will never have a complete sky coverage for any survey for example due to extinction by dust in the Milky Way, the spherical harmonics will no longer be orthogonal on parts of the sky. However, if the sky coverage is sufficiently large it suffices to multiply the log-likelihood with a factor

$$f_{\mathrm{sky}} \coloneqq \frac{\Omega_{\mathrm{survey}}}{\Omega_{\mathrm{sky}}} \,, \tag{6.45}$$

where Ω_{sky} is the solid angle of the full sky, i.e. 4π and Ω_{survey} is the solid angle covered by the survey. This additional factor captures the loss of information due to the partial sky coverage. If only small patches of the sky are observed, more evolved methods need to be used to mimic the effect of masking in Fourier space. This is the reason why one usually works in real space and evaluates correlation functions instead of power spectra if the sky coverage is small.

6.5 SURVEY CHARACTERISTICS

In this section we will explain the survey characteristics. The key parameters are tabulated in Table 3. We assume for simplicity that the surveys overlap and share the same survey area. The redshift distribution is the one from Eq. (3.28) with a mean redshift around unity and it is split up into six tomographic bins in such a way that each bin contains an equal number of galaxies.

Table 4: Parameters considered in the analysis together with their fiducial value for the ΛCDM reference models and a description of the parameter.

parameter	ΛCDM	Fisher σ	information
$\hat{\alpha}_B$	0.0	0.035	braiding
$\hat{\alpha}_M$	0.0	0.044	running of the Planck mass
w_0	-1.0	0.0091	equation of state today
w_a	0.0	0.029	linear time evolution of $w(a)$
$\sum m_\nu[eV]$	0.05	0.011	sum of neutrino masses
Ω_{mo}	0.314	0.0011	matter density
σ_8	0.834	0.0015	fluctuation amplitude
h	0.674	0.0010	Hubble constant
Ω_{bo}	0.0486	0.00016	baryon density
n_s	0.962	0.0013	spectral index
$k_s[Mpc/h]$	0.1	0.137	screening scale
b_0	0.68	0.0013	galaxy bias
M_c	0.26	0.0023	baryonic effects
η_b	0.5	0.0063	baryonic effects
z_{re}	11.357	0.265	recombination redshift

Figure 6.2 shows the cumulative and differential signal-to-noise for those survey characteristics. On the left one can see the CMB contribution together with cosmic shear from linear and non-linear structures. Clearly non-linear structure formation enhances the weak lensing signal significantly. The dashed lines show the different signal-to-noise, i.e. the individual contributions at each ℓ' in Eq. (6.44). For linear structure formation the curve peaks before $\ell' \approx 500$ since the shot noise starts dominating the cosmic shear signal. Non-linear clustering shifts the peak above $\ell' \approx 1000$. In the right column one can see the signal-to-noise over the whole multipole range, the sharp drop at $\ell = 2000$ is due to the cut-off used for galaxy clustering and cosmic shear. This cut-off was chosen to avoid the deeply non-linear regime, where baryonic physics become important and galaxy bias as well as intrinsic alignment becomes more complicated. Furthermore, the cumulative signal-to-noise stays nearly constant for $\ell > 2000$ since the instrumental noise dominates the spectrum.

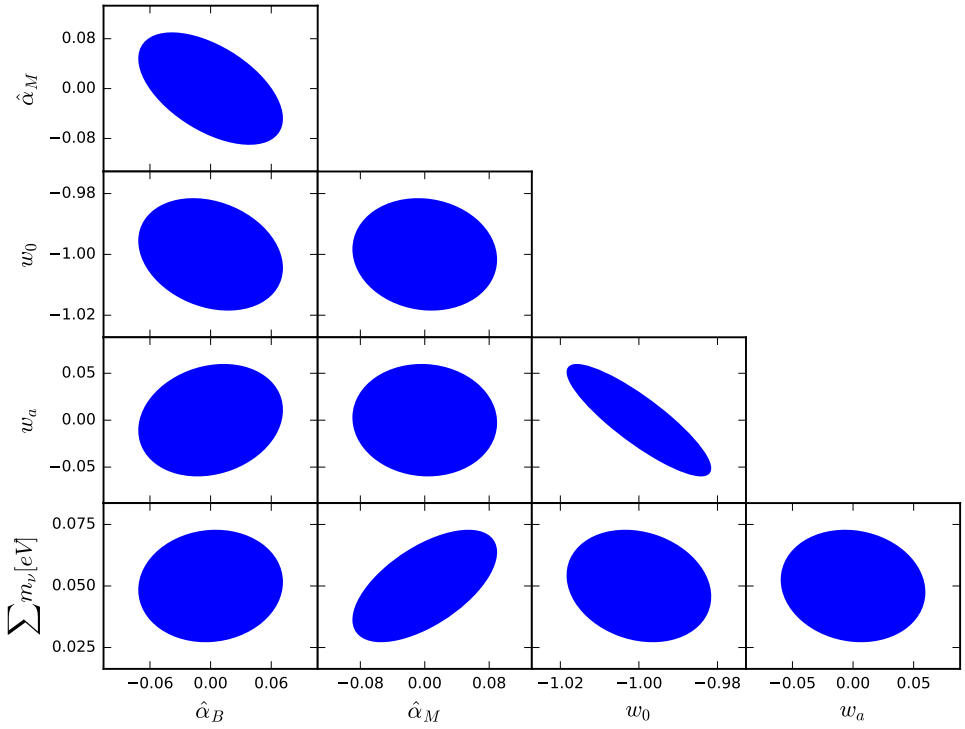

Figure 6.3: Fisher forecast for a survey with the settings as in Table 3. Shown are the 1σ contours from a Fisher matrix constructed around a ΛCDM reference cosmology. Since no prior information has been included in this analysis, constrains might allow for non-physical parameter values.

6.6 PARAMETER INFERENCE

6.6.1 *Fisher forecast*

We run a Fisher analysis varying all parameters described in Table 4 with the survey settings from Table 3 and show the resulting marginalized 1σ contours in Figure 6.3 for a few chosen parameters. In particular, we show constrains on the two DE parameters, the remaining two MG parameters and the sum of the neutrino masses. The constrains, $\sigma_i^2 = (\mathbf{F}^{-1})_{ii}$, for all other parameters are summarized in Table 4. We find that the two remaining degrees of freedom in this parametrization of Horndeski models can be constrained to $\lesssim 10\%$, while the two DE parameters are constrained at the percent level. Furthermore, there is a strong degeneracy between $\hat{\alpha}_B$ and $\hat{\alpha}_M$. The DE equation of state parameter show the usual degeneracy due to LSS measurements. Also a slight degeneracy between both MG parameters and the DE parameters is present which is also due to structure growth as can be seen from the equation for the growth factor where w_0 influences the expansion history. The neutrino mass is mainly degenerate with the running of the Planck mass since both influence structure growth directly. Of particular importance for the constraints on the MG parameters is the combination of galaxy clustering and cosmic shear and especially their cross-correlation since both probes carry complementary sensitivity on the underlying theory of gravity. Cosmic shear probes the potential landscape with massless

Table 5: Parameters used for the MCMC with prior and fiducial values. The absolute errors derived from MCMC and the Fisher analysis are shown.

parameter	fiducial	Fisher σ	flat prior	MCMC σ
$\hat{\alpha}_B$	0.1	0.037	$[0,\infty)$	0.061
$\hat{\alpha}_M$	0.2	0.035	$[0,\infty)$	0.46
w_0	-0.8	0.0062	$[-1,1]$	0.0136
w_a	0.2	0.017	$[0,\infty)$	0.030
$\sum m_\nu[eV]$	0.05	0.012	$[0,\infty)$	0.014
Ω_{mo}	0.314	0.00095	$[0,\infty)$	0.00111
σ_8	0.834	0.0017	$[0,\infty)$	0.0018
h	0.674	0.00082	$[0,\infty)$	0.00135
Ω_{bo}	0.0486	0.00014	$[0,\infty)$	0.00020
n_s	0.962	0.0014	$[0,\infty)$	0.0014
$k_s[Mpc/h]$	0.1	0.012	$[0,\infty)$	0.012
b_0	0.68	0.0013	$[0,\infty)$	0.0016
M_c	0.26	0.0022	$[0,\infty)$	0.0023
η_b	0.5	0.0066	$[0,\infty)$	0.0066
z_{re}	11.357	0.265	$[0,\infty)$	0.280

particles, while galaxy clustering probes the same landscape with massive particles, which therefore yields very tight constraints on the gravitational theory.

We now define the figure of merit

$$\mathrm{FOM}(i,j) = \sqrt{\det[\mathbf{F}_{(i,j)}]}\,, \tag{6.46}$$

where i and j label a pair of parameters and $\mathbf{F}_{ij}$ is the marginalized 2×2 Fisher matrix of the corresponding parameters, that is the inverse of the reduced covariance matrix, where only the entries of the two parameters have been picked out. The figure of merit describes the volume of the Fisher matrix and therefore the constraining power with respect to the parameters i and j.

In Figure 6.4 we show how the figure of merit varies across parameter space relative to the reference ΛCDM cosmology. In particular we show its dependence on the two MG parameters. It is evident that the figure of merit depends on the choice of the fiducial model since all model parameters are highly non-linear. If the fiducial cosmology moves further away from ΛCDM, constraints on the MG parameters become generally much tighter. Changing $\hat{\alpha}_B$ and $\hat{\alpha}_M$ from $(0,0)$ to $(0.1,01)$ amounts to a change of a factor of two. This effect is very similar to effects in clustering DE models, where the effects of clustering is larger if $w_0 \neq -1$. Another effect is of course due to the marginalization procedure in the highly non-linear parameter space.

It should be noted that we did not show the kineticity and the tensor speed excess since they are basically unconstrained by cosmological probes and are recently very

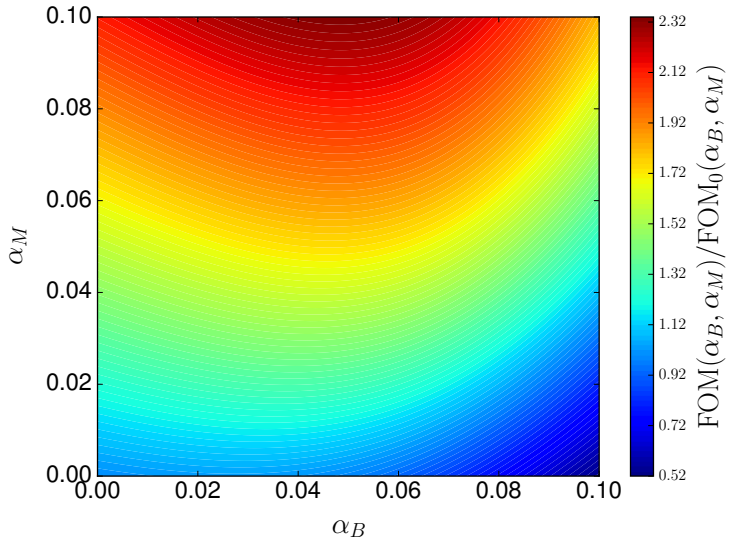

Figure 6.4: Relative difference of the figure of merit, Eq. (6.46). The reference model, i.e. where $\mathrm{FOM}_0(i,j)$ is calculated, is chosen to be the reference model from Table 4. We constructed a Lie basis for the Fisher matrix at this point as described in Chapter 4.

tightly constrained by gravitational wave experiments (Abbott et al., 2017; Abbott et al., 2017), respectively. Both parameters have been set close (for numerical stability) to ΛCDM reference values. Furthermore, $\hat{\alpha}_K$ is not degenerate with the other parameters, so it can be marginalized over without much loss of information. Since α_T is constrained so tightly, it effectively amounts to a delta function prior and therefore a marginalization does not yield any information loss either.

6.6.2 *MCMC constraints*

For the MCMC we use the sampling technique proposed by Goodman and Weare (2010). It uses techniques which are unaffected by affine transformations of the parameter space and turn out to be highly effective for skewed distributions. Furthermore, parallelization is straightforward so that the parameter space can be sampled efficiently. We choose a different fiducial cosmology than the ΛCDM one, to investigate the structure of the parameter space in all directions. This would not be possible for the ΛCDM fiducial, since $\alpha_i < 0$ or $w < -1$ leads to instabilities of the scalar field. We run a Fisher analysis simultaneously and summarize the results in Table 5. Clearly the Gaussian approximation yields tighter constraints on all parameters as expected from the Cramér-Rao bound. For more linear model parameters, such as σ_8, the differences between the Fisher analysis and the MCMC is smaller.

Figure 6.5 shows the results of the MCMC as joint plots for chosen parameters. We present the two-dimensional marginalized contours with one-dimensional ones. The degeneracy between $\hat{\alpha}_B$ and $\hat{\alpha}_M$ is clearly visible. Furthermore, the distribution of $\hat{\alpha}_B$ is very antisymmetric due to the prior, having a long tail to higher values. The same is true for $\hat{\alpha}_M$ but the situation is not as severe. Since $\hat{\alpha}_B$ is skewed through the prior information also $\hat{\alpha}_M$ will follow a more skewed distribution because of the

degeneracy. There is no strong degeneracy between the sum of the neutrino masses, m_ν and the modified so far in the MCMC. Furthermore, there is the usual degeneracy between w_0 and w_a with both individual distributions being very symmetric. For Ω_m and σ_8 the combination of CMB and LSS measurements breaks their degeneracy and both parameters can be constrained very well. In Figure 6.6 we show

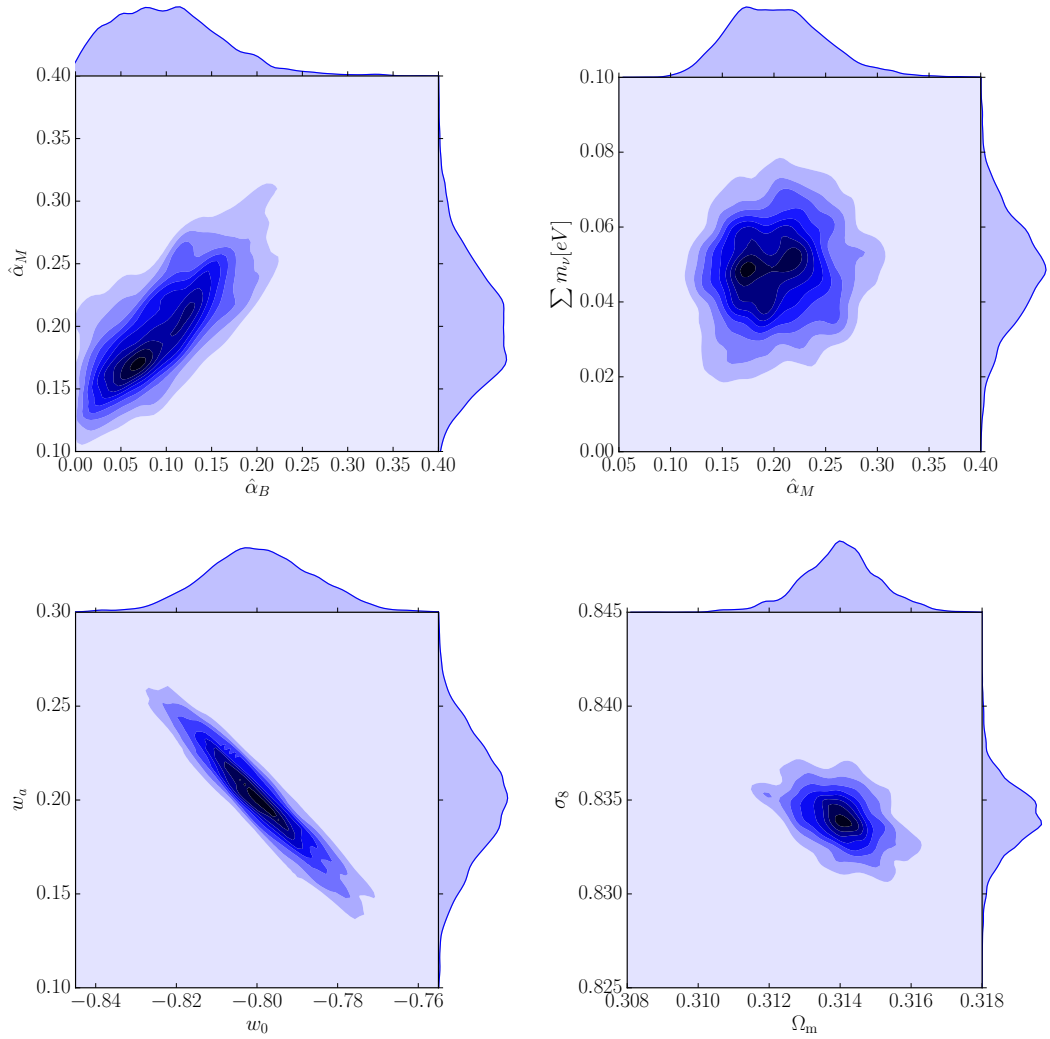

Figure 6.5: Joint plots for chosen parameters. We show the results of the MCMC for the two-dimensional and one-dimensional marginalized posterior for the MG parameters, the DE parameters, the neutrino masses, the matter density and fluctuation strength.

the the same parameters as in Figure 6.3 and compare the MCMC results with the Fisher forecast. The outermost contour depicts the 68% confidence interval with the corresponding Fisher ellipse in red. Clearly the 1σ contour for the Gaussian approximation is lies within the 68% contour of the MCMC. Furthermore, the degeneracy directions of both methods are the same for most parameters. It should, however, be noted that the MCMC have not completely converged yet in the sense that the tails of the distribution in the high dimensional parameter space have not been sampled sufficiently yet. The results presented here show that weakly constrained and degen-

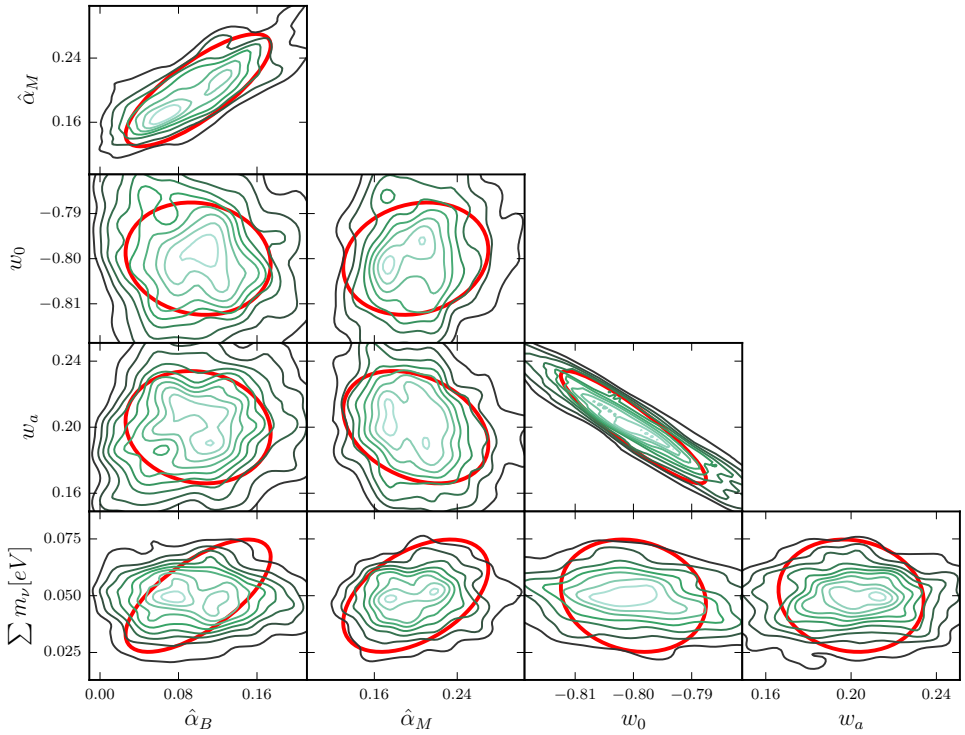

Figure 6.6: MCMC forecast for a survey with the settings given in Table 3. The outermost contour shows the 68% interval. Red ellipses show the corresponding interval for the Gaussian approximation of the posterior.

erate parameters show a substantial amount of non-Gaussianity. In contrast, for well constrained parameters the Gaussian approximation is sufficient since the deviation from the fiducial, thus allowing to cancel the Taylor expansion of the posterior after the second order.

6.7 GENERAL NOTES ON PARAMETER SPACES

In this section we will discuss some general properties of parameter spaces. We start with a Fisher matrix as the Gaussian approximation for the posterior. Since only probability differences between two models, i.e. points in the parameter space, are important, the absolute value of the posterior has now meaning as long as one is only comparing models within the same class. In other words models which live in the same parameter space. This arbitrary additive constant to the χ^2 corresponds to the evidence in Bayes' theorem and is just the normalization of the posterior. Thus the object of interest is a difference in χ^2:

$$\Delta\chi^2 = F_{ij}\Delta\theta^i\Delta\theta^j \,, \tag{6.47}$$

where θ^i is the i-th parameter of the set $\mathcal{T} := \{\theta_1, ..., \theta_n\}$ which we collect in a vector θ. Eq. (6.47) can as well be expressed differentially:

$$d\chi^2 = F_{ij}d\theta^i d\theta^j \,, \tag{6.48}$$

such that $F_{ij} = F_{ij}(\theta)$. The set of points $\mathcal{T}$ can be interpreted as a topological manifold, where topological refers to the topology with which the set $\mathcal{T}$ is equipped, which is needed to define continuous and differentiable function on the set. Additional structure can be introduced on the manifold. Let us interpret $\mathcal{T}$ as a manifold of probability distributions:

$$\forall t \in \mathcal{T} \; \exists \, p(t) \; : \; p(x,t) \text{ is a probability density in } x \; . \tag{6.49}$$

Then this manifold can be equipped with a metric, which is uniquely, up to a multiplicative constant, given by the Fisher matrix. Furthermore, we can introduce a connection ∇ on $\mathcal{T}$ which then allows for the identification of geodesics: Those are curves $\gamma(\lambda)$, where λ is some affine parameter, satisfying

$$\boldsymbol{\nabla}_{\dot{\gamma}} \dot{\boldsymbol{\gamma}} = 0 \; . \tag{6.50}$$

The geodesic length of a curve can now be related to the geodesic

$$L = \int d\lambda \sqrt{\mathbf{F}(\dot{\boldsymbol{\gamma}}, \dot{\boldsymbol{\gamma}})} \; , \tag{6.51}$$

with $\dot{\boldsymbol{\gamma}}$ subject to (6.50). Given a connection curvature can be defined in the following way

$$\mathbf{R}(\boldsymbol{u}, \boldsymbol{v})\boldsymbol{w} = \left[[\boldsymbol{\nabla}_{\boldsymbol{u}} \boldsymbol{\nabla}_{\boldsymbol{v}} - \boldsymbol{\nabla}_{\boldsymbol{v}} \boldsymbol{\nabla}_{\boldsymbol{u}} - \boldsymbol{\nabla}_{[\boldsymbol{u},\boldsymbol{v}]} \right] \boldsymbol{w} \; , \tag{6.52}$$

where $[.,.]$ is the commutator. R is a vector and can be turned into a tensor by applying a dual vector. The Riemann tensor describes the curvature of $\mathcal{T}$, in n dimensions it has

$$C_n \equiv \frac{n^2(n^2-1)}{12} \; , \tag{6.53}$$

independent components, which connects Gaussianization of a probability distribution with the curvature. This can be understood as follows: Given a set of parameters $\{p_i\}$ which act as coordinates of the manifold, the Riemann curvature tensor can be calculated from the metric and the connection. If one assumes a metric connection $\boldsymbol{\nabla}_{\boldsymbol{v}} \boldsymbol{g} = 0$ the connection coefficients Γ^i_{jk} are given by derivatives of the metric. The Riemann tensor thus depends on first and second derivatives of the metric.

Let us, for illustrative purposes, consider the case where the Fisher matrix is given by Eq. (6.39). If the model is linear in all parameters p_i the metric of the corresponding manifold will be constant, thus having a flat structure with the curvature vanishing identically. At the same time, the Fisher approximation is exact if the parameters are all linear, since all higher order terms of the expansion vanish. In this sense a flat parameter manifold corresponds to a posterior which is Gaussian. By a suitable rescaling of the parameters p_i the metric of this manifold can be brought into a Euclidean form.

In general the model is a non-linear function of the parameters p_i and therefore the connection coefficients as well as the curvature does not vanish. If one considers, however, a model with only one parameter, one finds $C_n = 0$ from Eq. (6.53), thus there is no independent component in the curvature. Clearly for any one-dimensional probability density, $p(x)$, where x is the model parameter, one can find another parameter $y = y(x)$ subject to

$$p(x)dx = p(y)dy \; . \tag{6.54}$$

The Jacobian can now be chosen such that $p(y)$ becomes a Gaussian distribution. Obviously the transformation has to be non-linear. If the parameter space has more than one dimension, it is not possible to find a general coordinate transformation which would lead to a Gaussian distribution. However, one can always find a local coordinate system such that the connection coefficients vanish by means of the exponential map.

As the components of the curvature tensor, $R^i{}_{jkl}$, are of course coordinate dependent, one has to build invariant quantities from it. The lowest order invariant is the Ricci scalar, R, which is the trace of the Ricci tensor, $R_{ij} = R^k{}_{ikj}$, which itself is the only non-vanishing trace of the Riemann tensor. Another invariant is the Kretschmann scalar, K, which includes the trace-full (Ricci) and the trace-less (Weyl) part of the curvature tensor:

$$K = R^i{}_{jkl} R_i{}^{jkl} \,. \tag{6.55}$$

Evaluating K gives an coordinate independent expression for the non-linearity or equivalently non-Gaussianity of a model from which the posterior is calculated.

6.8 CONCLUSION

In this chapter we investigated the possibility to constrain a certain class of MG models with future cosmological surveys. Particularly, we used CMB temperature and polarization anistropies together with CMB lensing, galaxy clustering and cosmic shear measurements. We constructed a Gaussian likelihood of spherical harmonic modes, $a_{\ell m}$, with a model dependent covariance. The likelihood was then analysed with Bayesian methods to forecast the expected statistical errors on the MG parameters as well as on cosmological and nuisance parameters and the sum off the neutrino masses. To explore the full shape of the likelihood we also used MCMC to fit mock data and compared it to a Fisher analysis. Finally, the geometrical structure of parameter spaces was discussed briefly. We summarize our main results as follows:

1. Theories of the Horndeski class can be constrained to the 10% level if external constraints from gravitational wave experiments are included. Otherwise the degeneracy with the tensor speed excess will increase the statistical errors significantly.

2. The inclusion of the cross-correlation between the different probes yields additional sensitivity to the experiment. They must, however, be included in the first place to build a consistent model and to not run into trouble with wrongly estimated errors.

3. The MCMC shows nearly no non-Gaussianities in well constrained parameters such as Ω_{mo} or σ_8, since the data only allows for a very narrows region in parameter space in which the posterior is well described by a Gaussian. In contrast, poorly constrained parameters show a significant amount of non-Gaussianity.

4. Parameter spaces in cosmology can be described as a manifold equipped with a metric given by the Fisher matrix. Curvature invariants can be constructed

on the manifold assuming a Levi-Civita connection which describe the non-linearity of a model in a coordinate, or parameter, independent way.

Future work will deal with additional systematic effects in the inference process such as intrinsic alignments. Furthermore, the geometrical structure of parameter spaces in cosmology requires more investigation.

7

SUMMARY AND OUTLOOK

In this work we covered different aspects of the non-linear growth of the LSS as well as the interaction of clusters and galaxies with it and how it can be used to study MG theories with future surveys and the problems one has to deal with. The first part discussed the problem of covariance matrices in high dimensional parameter spaces which are only accessible through numerical N-body simulations. This poses a tough computational problem for future surveys where the covariance matrix needs to be known very accurately across parameter space.

The main result of this first part was to provide a formalism to extrapolate a matrix-valued function, $\mathcal{F}$, with the parameter space being the set, M, on which the function is acting. More precisely, M is a vector space or, depending on the interpretation, a manifold, yielding the necessary structure for the construction of the generators generators which capture the transformation behaviour of $\mathcal{F}$ across M. These generators then amount to an infinitesimal transformation between neighbouring points M. By taking the limit of successive infinitesimal transformation, we arrived at the usual exponential expression. The commutation relations between the generators provide the necessary structure to carry out finite transformations by virtue of the Baker-Campbell-Hausdorff formula, where the structure of the transformation is given by $\mathcal{F}' = \mathbf{U}\mathcal{F}\mathbf{U}^{\mathsf{T}}$, where $\mathbf{U}$ is the usual matrix exponential of the generator acting on a shift vector in M. By again Taylor-expanding $\mathbf{U}$, we calculated the variation of covariance matrices, $\mathbf{C}$, of the matter density and cosmic shear power spectrum estimator. The generators and thus $\mathbf{U}$ where computed using SPT at tree-level. $\mathbf{U}$ was then approximated by the first two terms of its Taylor series, that is the identity and a term linear in the generators and the applied shift on M. We found that this approximation is sufficient to capture the basic behaviour of $\mathbf{C}$ across parameter space in comparison to numerical N-body simulations for the two dominant parameters Ω_{mo} and σ_8. Furthermore, the expected behaviour of the covariance as a function of other cosmological parameters like w_0 or n_s is captured as well. The linear approximation of $\mathbf{U}$ suffices to capture the behaviour over a wide range of parameters. Furthermore, a spectral analysis of $\mathbf{U}$ allows for an efficient sampling of parameter space, since the directions of largest change in $\mathbf{C}$ can be identified. In these directions, numerical simulations have to be placed more densely, while only a coarse spacing in other directions is needed. This is especially true for the degeneracy directions of the parameters with respect to the covariance. As an illustrative example we used a *Euclid*-like experiment with a CMB prior and found that the necessary amount of simulations can be reduced dramatically by rotating the coordinate system of the $\Omega_{\mathrm{mo}} - \sigma_8$ plane. Also the directions of largest change of the covariance can be used to check by how much the covariance changes depending on the step size in parameter space. Furthermore, the formalism can be applied to every matrix-valued function provided it is positive-definite. This condition is necessary since the inverse of $\mathcal{F}$ needs to be calculated in the process of constructing the generators. Additionally, it is not restricted to applications in cosmology and can be easily used for other situations where the covariance matrix needs to be known at a many different points

in parameter space, but is only accessible by expensive numerical calculations. Another object which is positive-definite is the Fisher matrix. In a companion paper we investigated its behaviour across parameter space and how constraints in cosmology change depending on the best fit value of the parameters.

In the second part we discussed the influence of tidal interactions on the gravitational collapse of dark matter halos in the SPC model. The latter is a primal ingredient to cluster counts and is usually treated as an isolated collapse, i.e. the evolution of a spherical over-density in a homogeneous expanding background. We investigate the effect of tidal forces exerted by the ambient LSS on test particles. Tidal fields are generated by large-scale inhomogeneities whose statistics have been described by first order LPT. Due to this first order approximation, the Gaussianity of the density field is conserved and the statistics are still fully described by its power spectra. Furthermore, our approximation did not allow to include vorticity generation in the density field directly, since it decays at first order due to the expansion. Using the symmetry of the problem, we constructed a basis in Fourier space to sample the values of the tidal field tensor, $\mathbf{\Psi}$, which in turn can be related to the shear tensor, $\boldsymbol{\sigma}$. In particular it is described by the traceless symmetric part of $\mathbf{\Psi}$. Since the components of $\boldsymbol{\sigma}$ are coordinate dependent, the lowest order non-vanishing invariant is the trace of its square, σ^2. The scalar shear, σ^2, is proportional to square in the velocity and is thus a second order effect entering in the evolution equation of the SPC. Consequently, we consistently found that the effect of shear is only of the order of a percent when calculating the critical over-density δ_c as it is derived from the linear evolution equation for which only the initial conditions are derived from the fully non-linear equation. Since $\mathbf{\Psi}$ is a random variable, its statistic is inherited by δ_c turning it into a random variable as well. This will introduce an additional scatter of the mass function and cluster counts, although the main uncertainty will still be the large errors on mass estimates of galaxy clusters and groups. We also established a mass dependence of δ_c by applying a low-pass filter to the density field filtering out all modes with a smaller wavelength than the scale of the considered object. These modes will thus have negligible contribution to $\mathbf{\Psi}$. For this reason high mass objects will be less affected by tidal forces than low mass objects. We investigated the scaling of $\langle\sigma^2\rangle$ and $\langle\delta_c\rangle$ with the halo mass and used them to study an average mass function and cluster counts including tidal shear. By carrying out a forecast, we found that the additional tidal interaction will induce a 1σ bias on Ω_{mo} and σ_8 if not accounted for. We then also investigated the influence of rotation on the collapse dynamic since the important term in the equation is $\sigma^2 - \omega^2$. Complementary to $\boldsymbol{\sigma}$, $\boldsymbol{\omega}$ is the anti-symmetric part of $\mathbf{\Psi}$. The generation of rotation was described by tidal torquing and calculated by splitting the product of $\mathbf{\Psi}$ and the inertial tensor $\mathbf{I}$ into a symmetric and anti-symmetric part and identifying terms. $\mathbf{I}$ is related to the curvature of the density field at a position of a peak allowing a description in the same framework as before, but now with a larger set of correlated random variables. When considering peaks of the density field, we found that $\sigma^2 - \omega^2 > 0$, implying that the collapse of a spherical object in a tidal field proceeds always faster than the collapse in a homogeneous background. We again calculated the resulting distribution of δ_c and found it to be very similar to the one with shear only. The term $\sigma^2 - \omega^2$ was already discussed in previous works using phenomenological methods who found an opposite behaviour. The model presented here instead is fully consistent across the scales we considered,

i.e. as long as first order LPT is valid, and if angular momentum and shearing effects are only exerted by the ambient LSS. In reality, other effects can also play an important role for the angular momentum of a galaxy such as baryonic physics or mergers of different object which both are not incorporated in the model outlined in this thesis.

The last part of this work studied the opportunities to test the cosmological model and the underlying theory of gravity with future surveys of the LSS and the CMB. In particular, we took cosmic shear, galaxy clustering, CMB primaries and CMB lensing into account with all cross-correlations between the different probes. An advantage of this combination is that complement mechanisms are tested, while cosmic shear tests the sum of the two Bardeen potentials, galaxy clustering only probes the one entering in the time-time component of the perturbed metric. Even more so the CMB itself serves as a cosmological probe with very high sensitivity on the cosmological parameters at a very different epoch as the LSS measurements. In particular, we investigated a very general class of MG theories with one additional degree of freedom, the Horndeski class. At linear order in perturbation theory, this class is described by four free functions of time. By assuming a simple form for those functions we fitted the remaining free parameters to mock data. We did this with a Fisher analysis as well as with a MCMC to fully investigate the non-linear degeneracies of the parameter space and giving conservative forecasting error estimates. We assumed that the data follows a Gaussian distribution, which is an assumption and needs to be revised when facing real data. By interfacing the Boltzmann code `HiCLASS` with our code, we calculated all the spectra not produced by the `HiCLASS`. We then carried out a maximum likelihood analysis to forecast constraints on a high dimensional parameter space including cosmological, gravitational and nuisance parameters describing for example baryonic effects to the power spectrum. If including other constraints from gravitational wave experiments which set the propagation speed of the waves to c, one is able to constrain the remaining parameters of the Horndeski class to the 10 percent level. It should be noted that there is still one free parameter in these type of models which is the kineticity, describing the kinetic term of the additional scalar degree of freedom. This parameter has basically no observational signature if it is not changed by many orders of magnitude. Since it is not degenerate with the other parameters it can be safely ignored in the analysis. We furthermore found that the distribution of well constrained parameters, such as Ω_{m0} is very well described by a Gaussian, while for example the MG parameters show a substantial amount of non-Gaussianity. This is of course expected since the vast amount of data present due to future surveys shrinks the confidence intervals such that the Gaussian approximation done in the Fisher matrix forecast is valid for those parameters and the marginalization procedure over non-Gaussian parameters does not significantly influence the distribution as it is very narrow in one direction. We also investigated how the figure of merit of the MG parameters change across parameter space and found that models further away from ΛCDM are generally constrained more tightly. We closed this last part with a general discussion of the geometric structure of parameter spaces, which relates to the Lie basis presented in Chapter 4. Here we interpreted the parameter space as a manifold equipped with a metric which is given by the Fisher information matrix. The manifold of a Gaussian distribution where the model has only linear parameters is then described by a flat manifold since its Fisher matrix

is constant. However, more complicated models have non-linear parameters which in turn yield a parameter dependent Fisher matrix and can thus be interpreted as a curved manifold.

In the future we plan to further investigate the geometrical structure of parameter spaces to identify and interpret invariant quantities of the parameter space and to study the inference process and MCMC in cosmology in this framework. Furthermore, another important topic in this context is the flow of information between the different probes considered. Additional goals are a further exploration of the tidal interaction of objects in the LSS with the LSS itself, especially in terms of intrinsic alignment and providing a fast and accurate framework. Especially for the discussion in Chapter 6 we ignored intrinsic alignments altogether. However, they are one of the main uncertainties in weak gravitational lensing measurements and even more importantly carry complementary information compared to the cosmic shear signal. Finally, the inclusion of non-linear scales in the MG sector has to be investigated more since they make up a lot of the signal for future surveys, but cannot be used in a reliable way even in a ΛCDM model.

BIBLIOGRAPHY

Abazajian, Kevork N. et al. (2016). 'CMB-S4 Science Book, First Edition.' In: *ArXiv e-prints*. arXiv: 1610.02743v1 [astro-ph.CO].

Abbott, B. P. et al. (2016). 'Observation of Gravitational Waves from a Binary Black Hole Merger.' In: *Physical Review Letters* 116.6, 061102, p. 061102. DOI: 10.1103/PhysRevLett.116.061102. arXiv: 1602.03837 [gr-qc].

Abbott, B. P. et al. (2017). 'A gravitational-wave standard siren measurement of the Hubble constant.' In: *Nature* 551.7678, pp. 85–88. DOI: 10.1038/nature24471.

Abbott, B. P. et al. (2017). 'GW170817: Observation of Gravitational Waves from a Binary Neutron Star Inspiral.' In: *Physical Review Letters* 119.16, 161101, p. 161101. DOI: 10.1103/PhysRevLett.119.161101. arXiv: 1710.05832 [gr-qc].

Abramo, L. R. et al. (2007). 'Structure formation in the presence of dark energy perturbations.' In: *Journal of Cosmology and Astro-Particle Physics* 11, pp. 12–+. DOI: 10.1088/1475-7516/2007/11/012. arXiv: 0707.2882.

Abramo, L. R. et al. (2009). 'The signature of dark energy perturbations in galaxy cluster surveys.' In: *Journal of Cosmology and Astro-Particle Physics* 7, pp. 40–+. DOI: 10.1088/1475-7516/2009/07/040. arXiv: 0902.3226.

Alonso, D. et al. (2017). 'Observational future of cosmological scalar-tensor theories.' In: *Phys. Rev. D* 95.6, 063502, p. 063502. DOI: 10.1103/PhysRevD.95.063502. arXiv: 1610.09290.

Angrick, Christian and Matthias Bartelmann (2009). 'Statistics of gravitational potential perturbations: A novel approach to deriving the X-ray temperature function.' In: *Astronomy & Astrophysics* 494.2, pp. 461–470. URL: http://www.aanda.org/articles/aa/full_html/2009/05/aa09562-08/aa09562-08.html.

— (2010). 'Triaxial collapse and virialisation of dark-matter haloes.' In: *Astronomy & Astrophysics* 518, A38. URL: http://www.aanda.org/articles/aa/full_html/2010/10/aa14147-10/aa14147-10.html.

Avila-Reese, V. et al. (1998). 'On the Formation and Evolution of Disk Galaxies: Cosmological Initial Conditions and the Gravitational Collapse.' In: *ApJ* 505, pp. 37–49. DOI: 10.1086/306136. eprint: astro-ph/9710201.

Bacon, David et al. (2000). 'Detection of cosmic shear with the william herschel telescope.' In: *arXiv preprint astro-ph/0008248*. URL: http://arxiv.org/abs/astro-ph/0008248;http://arxiv.org/pdf/astro-ph/0008248.

Bailoni, Alberto et al. (2017). 'Improving Fisher matrix forecasts for galaxy surveys: window function, bin cross-correlation and bin redshift uncertainty.' In: *Monthly Notices of the Royal Astronomical Society* 470.1, pp. 688–705. DOI: 10.1093/mnras/stx1209.

Baldi, M. and F. Villaescusa-Navarro (2016). 'Cosmic Degeneracies II: Structure formation in joint simulations of Warm Dark Matter and f(R) gravity.' In: *ArXiv e-prints*. arXiv: 1608.08057.

Baldi, M. et al. (2014). 'Cosmic degeneracies - I. Joint N-body simulations of modified gravity and massive neutrinos.' In: *MNRAS* 440, pp. 75–88. DOI: 10.1093/mnras/stu259. arXiv: 1311.2588.

Ballinger, W. E. et al. (1995). 'The real-space power spectrum of IRAS galaxies on large scales and the redshift distortion.' In: *MNRAS* 276, pp. L59–L63. DOI: 10.1093/mnras/276.1.L59.

Bardeen, J. M. et al. (1986). 'The statistics of peaks of Gaussian random fields.' In: *ApJ* 304, pp. 15–61. DOI: 10.1086/164143.

Barreira, A. et al. (2013). 'Nonlinear structure formation in the cubic Galileon gravity model.' In: *JCAP* 10, 027, p. 027. DOI: 10.1088/1475-7516/2013/10/027. arXiv: 1306.3219.

Barreiro, T. et al. (2000). 'Quintessence arising from exponential potentials.' In: *Phys. Rev. D* 61.12, pp. 127301–+. DOI: 10.1103/PhysRevD.61.127301. eprint: arXiv:astro-ph/9910214.

Bartelmann, M. and P. Schneider (2001). 'Weak gravitational lensing.' In: *Phys. Rep.* 340, pp. 291–472. DOI: 10.1016/S0370-1573(00)00082-X. eprint: arXiv:astro-ph/9912508.

Bartelmann, M. et al. (2014). 'A microscopic, non-equilibrium, statistical field theory for cosmic structure formation.' In: *ArXiv e-prints*. arXiv: 1411.0806.

Bartelmann, M. et al. (2017). 'Kinetic field theory: effects of momentum correlations on the cosmic density-fluctuation power spectrum.' In: *New Journal of Physics* 19.8, 083001, p. 083001. DOI: 10.1088/1367-2630/aa7e6f. arXiv: 1611.09503. URL: http://adsabs.harvard.edu/abs/2017NJPh...19h3001B.

Battye, R. A. and J. A. Pearson (2012). 'Effective action approach to cosmological perturbations in dark energy and modified gravity.' In: *JCAP* 7, 019, p. 019. DOI: 10.1088/1475-7516/2012/07/019. arXiv: 1203.0398 [hep-th].

— (2013). 'Parametrizing dark sector perturbations via equations of state.' In: *Phys. Rev. D* 88.6, 061301, p. 061301. DOI: 10.1103/PhysRevD.88.061301. arXiv: 1306.1175.

Baumgart, D. J. and J. N. Fry (1991). 'Fourier spectra of three-dimensional data.' In: *ApJ* 375, pp. 25–34. DOI: 10.1086/170166.

Bekenstein, J. D. (1993). 'Relation between physical and gravitational geometry.' In: *Phys. Rev. D* 48, pp. 3641–3647. DOI: 10.1103/PhysRevD.48.3641. eprint: gr-qc/9211017.

Bellini, E. and I. Sawicki (2014). 'Maximal freedom at minimum cost: linear large-scale structure in general modifications of gravity.' In: *JCAP* 7, 050, p. 050. DOI: 10.1088/1475-7516/2014/07/050. arXiv: 1404.3713.

Benjamin, J. et al. (2007). 'Cosmological constraints from the 100-deg^2 weak-lensing survey.' In: *MNRAS* 381, pp. 702–712. DOI: 10.1111/j.1365-2966.2007.12202.x. eprint: arXiv:astro-ph/0703570.

Bernardeau, F. (1994). 'Skewness and kurtosis in large-scale cosmic fields.' In: *ApJ* 433, pp. 1–18. DOI: 10.1086/174620. eprint: arXiv:astro-ph/9312026.

Bernardeau, Francis and Lev Kofman (1994). 'Properties of the cosmological density distribution function.' In: *arXiv preprint astro-ph/9403028*. URL: http://arxiv.org/abs/astro-ph/9403028;http://arxiv.org/pdf/astro-ph/9403028.

Bernardeau, Francis et al. (2002). 'Large-scale structure of the Universe and cosmological perturbation theory.' In: *Physics Reports* 367.1, pp. 1–248. URL: http://www.sciencedirect.com/science/article/pii/S0370157302001357;http://arxiv.org/pdf/astro-ph/0112551.

Berti, E. et al. (2015). 'Testing general relativity with present and future astrophysical observations.' In: *Classical and Quantum Gravity* 32.24, 243001, p. 243001. DOI: 10.1088/0264-9381/32/24/243001. arXiv: 1501.07274 [gr-qc].

Bertschinger, E. (1985). 'Self-similar secondary infall and accretion in an Einstein-de Sitter universe.' In: *ApJS* 58, pp. 39–65. DOI: 10.1086/191028.

Bertschinger, E. and B. Jain (1994). 'Gravitational instability of cold matter.' In: *ApJ* 431, pp. 486–494. DOI: 10.1086/174501. eprint: astro-ph/9307033. URL: http://adsabs.harvard.edu/abs/1994ApJ...431..486B.

Bertschinger, E. and B. Jain (1994). 'Gravitational instability of cold matter.' In: *ApJ* 431, pp. 486–494. DOI: 10.1086/174501. eprint: arXiv:astro-ph/9307033.

Blazek, Jonathan et al. (2012). 'Separating intrinsic alignment and galaxy-galaxy lensing.' In: *Journal of Cosmology and Astroparticle Physics* 2012.5, p. 041. URL: http://iopscience.iop.org/1475-7516/2012/05/041 (visited on 09/25/2015).

Blazek, Jonathan et al. (2017). 'Beyond linear galaxy alignments.' In: *arXiv:1708.09247 [astro-ph]*. arXiv: 1708.09247. URL: http://arxiv.org/abs/1708.09247.

Bloomfield, J. (2013). 'A simplified approach to general scalar-tensor theories.' In: *JCAP* 12, 044, p. 044. DOI: 10.1088/1475-7516/2013/12/044. arXiv: 1304.6712 [astro-ph.CO].

Bond, J. R. and S. T. Myers (1996). 'The Peak-Patch Picture of Cosmic Catalogs. I. Algorithms.' In: *ApJS* 103, p. 1. DOI: 10.1086/192267.

Bondi, H. (1947). 'Spherically symmetrical models in general relativity.' In: *MNRAS* 107, p. 410. DOI: 10.1093/mnras/107.5-6.410.

Bouchet, F. R. et al. (1995). 'Perturbative Lagrangian approach to gravitational instability.' In: *AAP* 296, p. 575. eprint: astro-ph/9406013.

Buchert, T. (1989). 'A class of solutions in Newtonian cosmology and the pancake theory.' In: *AAP* 223, pp. 9–24.

— (1992). 'Lagrangian theory of gravitational instability of Friedman-Lemaitre cosmologies and the 'Zel'dovich approximation'.' In: *MNRAS* 254, pp. 729–737.

Camera, S. et al. (2015). 'Cosmology on the Largest Scales with the SKA.' In: *Advancing Astrophysics with the Square Kilometre Array (AASKA14)*, 25, p. 25. arXiv: 1501.03851.

Casas, S. et al. (2017). 'Linear and non-linear Modified Gravity forecasts with future surveys.' In: *ArXiv e-prints*. arXiv: 1703.01271.

Catelan, P. and L. Moscardini (1995). 'Kurtosis of Cosmological Density and Velocity Fields.' In: *Birth of the Universe and Fundamental Physics*. Ed. by F. Occhionero. Vol. 455. Lecture Notes in Physics, Berlin Springer Verlag, pp. 269–+. DOI: 10.1007/3-540-60024-8_112.

Catelan, P. and T. Theuns (1996). 'Evolution of the angular momentum of protogalaxies from tidal torques: Zel'dovich approximation.' In: *MNRAS* 282, pp. 436–454. eprint: arXiv:astro-ph/9604077. URL: http://articles.adsabs.harvard.edu/cgi-bin/nph-iarticle_query?1996MNRAS.282..436C&data_type=PDF_HIGH&whole_paper=YES&type=PRINTER&filetype=.pdf.

Catelan, P. et al. (2001). 'Intrinsic and extrinsic galaxy alignment.' In: *mnras* 320, pp. L7–L13.

Chen, X. (2010). 'Primordial Non-Gaussianities from Inflation Models.' In: *Advances in Astronomy* 2010, 638979, p. 638979. DOI: 10.1155/2010/638979. arXiv: 1002.1416 [astro-ph.CO].

Chevallier, M. and D. Polarski (2001). 'Accelerating Universes with Scaling Dark Matter.' In: *International Journal of Modern Physics D* 10, pp. 213–223. DOI: 10.1142/S0218271801000822. eprint: arXiv:gr-qc/0009008.

Clarkson, C. (2012). 'Establishing homogeneity of the universe in the shadow of dark energy.' In: *Comptes Rendus Physique* 13, pp. 682–718. DOI: 10.1016/j.crhy.2012.04.005. arXiv: 1204.5505.

Clifton, T. et al. (2012). 'Modified gravity and cosmology.' In: *Phys. Rep.* 513, pp. 1–189. DOI: 10.1016/j.physrep.2012.01.001. arXiv: 1106.2476.

Cole, S. and G. Efstathiou (1989). 'Gravitational lensing of fluctuations in the microwave background radiation.' In: *MNRAS* 239, pp. 195–200. DOI: 10.1093/mnras/239.1.195.

Collaboration, Planck et al. (2016). 'Planck 2015 results. XIII. Cosmological parameters.' In: *AAP* 594, A13, A13. DOI: 10.1051/0004-6361/201525830. arXiv: 1502.01589.

Cooray, A. and W. Hu (2001). 'Weak Gravitational Lensing Bispectrum.' In: *ApJ* 548, pp. 7–18. DOI: 10.1086/318660. eprint: arXiv:astro-ph/0004151.

Cooray, A. and M. Kesden (2003). 'Weak lensing of the CMB: extraction of lensing information from the trispectrum.' In: *NA* 8, pp. 231–253. DOI: 10.1016/S1384-1076(02)00225-7. eprint: astro-ph/0204068.

Cooray, A. and R. Sheth (2002). 'Halo models of large scale structure.' In: *Phys. Rep.* 372, pp. 1–129. DOI: 10.1016/S0370-1573(02)00276-4. eprint: arXiv:astro-ph/0206508.

Cooray, Asantha and Wayne Hu (2001). 'Power spectrum covariance of weak gravitational lensing.' In: *The Astrophysical Journal* 554.1, p. 56. URL: http://iopscience.iop.org/article/10.1086/321376/meta;http://arxiv.org/pdf/astro-ph/0012087.

Copeland, E. J. et al. (1998). 'Exponential potentials and cosmological scaling solutions.' In: *Phys. Rev. D* 57, pp. 4686–4690. DOI: 10.1103/PhysRevD.57.4686. eprint: gr-qc/9711068.

Copeland, E. J. et al. (2000). 'Quintessence models in supergravity.' In: *Phys. Rev. D* 62.12, pp. 123503–+. DOI: 10.1103/PhysRevD.62.123503. eprint: arXiv:hep-ph/0005222.

Copeland, E. J. et al. (2005). 'What is needed of a tachyon if it is to be the dark energy?' In: *Phys. Rev. D* 71.4, 043003, p. 043003. DOI: 10.1103/PhysRevD.71.043003. eprint: hep-th/0411192.

Copeland, E. J. et al. (2006). 'Dynamics of Dark Energy.' In: *International Journal of Modern Physics D* 15, pp. 1753–1935. DOI: 10.1142/S021827180600942X. eprint: arXiv:hep-th/0603057.

Corasaniti, P. S. (2004). 'Phenomenological aspects of dark energy dominated cosmologies.' PhD thesis. University of Sussex. URL: http://de.arxiv.org/pdf/astro-ph/0401517.

Corasaniti, P. S. and E. J. Copeland (2003). 'Model independent approach to the dark energy equation of state.' In: *Phys. Rev. D* 67.6, pp. 063521–+. DOI: 10.1103/PhysRevD.67.063521. eprint: arXiv:astro-ph/0205544.

Couchman, H. M. P. (1997). 'Simulating Cosmic Structure at High Resolution: Towards A Billion Particles?' In: *Computational Astrophysics; 12th Kingston Meeting*

on Theoretical Astrophysics. Ed. by D. A. Clarke and M. J. West. Vol. 123. Astronomical Society of the Pacific Conference Series, p. 340. eprint: astro-ph/9709299.

Crisostomi, M. and K. Koyama (2017). 'Self-accelerating universe in scalar-tensor theories after GW170817.' In: *ArXiv e-prints*. arXiv: 1712.06556.

Crittenden, R. G. et al. (2001). 'Spin-induced Galaxy Alignments and Their Implications for Weak-Lensing Measurements.' In: *ApJ* 559, pp. 552–571. DOI: 10.1086/322370. eprint: astro-ph/0009052.

Croft, Rupert AC and Christopher A. Metzler (2000). 'Weak-lensing surveys and the intrinsic correlation of galaxy ellipticities.' In: *The Astrophysical Journal* 545.2, p. 561. URL: http://iopscience.iop.org/0004-637X/545/2/561 (visited on 09/28/2015).

Daalen, Marcel P. van et al. (2011). 'The effects of galaxy formation on the matter power spectrum: a challenge for precision cosmology.' In: *Monthly Notices of the Royal Astronomical Society* 415.4, pp. 3649–3665. DOI: 10.1111/j.1365-2966.2011.18981.x.

Daalen, Marcel P. van et al. (2014). 'The impact of baryonic processes on the two-point correlation functions of galaxies, subhaloes and matter.' In: *Monthly Notices of the Royal Astronomical Society* 440.4, pp. 2997–3010. DOI: 10.1093/mnras/stu482.

Deffayet, C. et al. (2011). 'From k-essence to generalized Galileons.' In: *Phys. Rev. D* 84 (6), p. 064039. DOI: 10.1103/PhysRevD.84.064039. URL: http://link.aps.org/doi/10.1103/PhysRevD.84.064039.

Del Popolo, A. et al. (2013a). 'Extended Spherical Collapse and the Accelerating Universe.' In: *International Journal of Modern Physics D* 22, 1350038, p. 50038. DOI: 10.1142/S0218271813500387. arXiv: 1207.5789 [astro-ph.CO].

— (2013b). 'Spherical collapse model with shear and angular momentum in dark energy cosmologies.' In: *MNRAS* 430, pp. 628–637. DOI: 10.1093/mnras/sts669. arXiv: 1212.5092 [astro-ph.CO].

Di Dio, E. et al. (2016). 'The bispectrum of relativistic galaxy number counts.' In: *JCAP* 1, 016, p. 016. DOI: 10.1088/1475-7516/2016/01/016. arXiv: 1510.04202.

Diego, J. M. and S. Majumdar (2004). 'The hybrid SZ power spectrum: combining cluster counts and SZ fluctuations to probe gas physics.' In: *MNRAS* 352, pp. 993–1004. DOI: 10.1111/j.1365-2966.2004.07989.x. eprint: arXiv:astro-ph/0402449.

Doran, M. (2005). 'CMBEASY: an object oriented code for the cosmic microwave background.' In: *Journal of Cosmology and Astro-Particle Physics* 10, pp. 11–+. DOI: 10.1088/1475-7516/2005/10/011. eprint: arXiv:astro-ph/0302138.

Doran, M. and G. Robbers (2006). 'Early dark energy cosmologies.' In: *Journal of Cosmology and Astro-Particle Physics* 6, pp. 26–+. DOI: 10.1088/1475-7516/2006/06/026. eprint: arXiv:astro-ph/0601544.

Doroshkevich, A. G. (1970). 'The space structure of perturbations and the origin of rotation of galaxies in the theory of fluctuation.' In: *Astrofizika* 6, pp. 581–600.

Eifler, Tim et al. (2009). 'Dependence of cosmic shear covariances on cosmology-Impact on parameter estimation.' In: *Astronomy & Astrophysics* 502.3, pp. 721–731. URL: http://www.aanda.org/articles/aa/full_html/2009/30/aa11276-08/aa11276-08.html.

Einstein, A. (1915). 'Die Feldgleichungen der Gravitation.' In: *Sitzungsberichte der Königlich Preußischen Akademie der Wissenschaften (Berlin), Seite 844-847.*

Eisenstein, D. J. and A. Loeb (1995). 'An analytical model for the triaxial collapse of cosmological perturbations.' In: *ApJ* 439, pp. 520–541. DOI: 10.1086/175193. eprint: arXiv:astro-ph/9405012.

Eke, V. R. et al. (1996). 'Cluster correlation functions in N-body simulations.' In: *MNRAS* 281, p. 703. DOI: 10.1093/mnras/281.2.703. eprint: astro-ph/9602091.

Fang, W. and Z. Haiman (2007). 'Constraining dark energy by combining cluster counts and shear-shear correlations in a weak lensing survey.' In: *Phys. Rev. D* 75.4, pp. 043010–+. DOI: 10.1103/PhysRevD.75.043010. eprint: arXiv:astro-ph/0612187.

Feldman, H. A. et al. (1994). 'Power-spectrum analysis of three-dimensional redshift surveys.' In: *ApJ* 426, pp. 23–37. DOI: 10.1086/174036. eprint: astro-ph/9304022.

Ferraro, S. et al. (2015). 'WISE measurement of the integrated Sachs-Wolfe effect.' In: *Phys. Rev. D* 91.8, 083533, p. 083533. DOI: 10.1103/PhysRevD.91.083533. arXiv: 1401.1193.

Fillmore, J. A. and P. Goldreich (1984). 'Self-similar gravitational collapse in an expanding universe.' In: *ApJ* 281, pp. 1–8. DOI: 10.1086/162070.

Fixsen, D. J. et al. (1996). 'The Cosmic Microwave Background Spectrum from the Full COBE FIRAS Data Set.' In: *ApJ* 473, p. 576. DOI: 10.1086/178173. eprint: astro-ph/9605054.

Font-Ribera, A. et al. (2014). 'DESI and other Dark Energy experiments in the era of neutrino mass measurements.' In: *JCAP* 5, 023, p. 023. DOI: 10.1088/1475-7516/2014/05/023. arXiv: 1308.4164.

Forero-Romero, J. E. et al. (2014). 'Cosmic web alignments with the shape, angular momentum and peculiar velocities of dark matter haloes.' In: *mnras* 443, pp. 1090–1102. DOI: 10.1093/mnras/stu1150.

Fosalba, P. et al. (2008). 'The onion universe: all sky lightcone simulations in spherical shells.' In: *MNRAS* 391, pp. 435–446. DOI: 10.1111/j.1365-2966.2008.13910.x. arXiv: 0711.1540.

Fry, James N (1984). 'The Galaxy correlation hierarchy in perturbation theory.' In: *The Astrophysical Journal* 279, pp. 499–510. URL: http://adsabs.harvard.edu/full/1984ApJ...279..499F.

Gamow, G. (1948). 'The Origin of Elements and the Separation of Galaxies.' In: *Physical Review* 74, pp. 505–506. DOI: 10.1103/PhysRev.74.505.2.

Gleyzes, J. et al. (2014). 'A unifying description of dark energy.' In: *International Journal of Modern Physics D* 23, 1443010, p. 1443010. DOI: 10.1142/S021827181443010X. arXiv: 1411.3712 [hep-th].

Goodman, J. and J. Weare (2010). 'Ensemble samplers with affine invariance.' In: *Communications in Applied Mathematics and Computational Science, Vol. 5, No. 1, p. 65-80, 2010* 5, pp. 65–80. DOI: 10.2140/camcos.2010.5.65.

Groth, E. J. and P. J. E. Peebles (1977). 'Statistical analysis of catalogs of extragalactic objects. VII - Two- and three-point correlation functions for the high-resolution Shane-Wirtanen catalog of galaxies.' In: *ApJ* 217, pp. 385–405. DOI: 10.1086/155588.

Gunn, J. E. and J. R. Gott III (1972). 'On the Infall of Matter Into Clusters of Galaxies and Some Effects on Their Evolution.' In: *ApJ* 176, p. 1. DOI: 10.1086/151605.

Guth, A. H. (1981). 'Inflationary universe: A possible solution to the horizon and flatness problems.' In: *Phys. Rev. D* 23, pp. 347–356. DOI: 10.1103/PhysRevD.23.347.

Hannestad, Steen and Thomas Tram (2017). 'Optimal prior for Bayesian inference in a constrained parameter space.' In: arXiv: 1710.08899v1 [astro-ph.CO].

Heavens, A. F. and A. N. Taylor (1995). 'A spherical harmonic analysis of redshift space.' In: *MNRAS* 275, pp. 483–497. DOI: 10.1093/mnras/275.2.483. eprint: astro-ph/9409027.

Heavens, A. et al. (2000). 'Intrinsic correlation of galaxy shapes: implications for weak lensing measurements.' In: *mnras* 319, pp. 649–656.

Heavens, Alan F and Ravi K Sheth (1999). 'The correlation of peaks in the microwave background.' In: *Monthly Notices of the Royal Astronomical Society* 310.4, pp. 1062–1070. URL: http://mnras.oxfordjournals.org/content/310/4/1062.short.

Heitmann, K. et al. (2010). 'The Coyote Universe. I. Precision Determination of the Nonlinear Matter Power Spectrum.' In: *ApJ* 715, pp. 104–121. DOI: 10.1088/0004-637X/715/1/104. arXiv: 0812.1052.

Hellwing, Wojciech A. et al. (2016). 'The effect of baryons on redshift space distortions and cosmic density and velocity fields in the EAGLE simulation.' In: *Monthly Notices of the Royal Astronomical Society: Letters* 461.1, pp. L11–L15. DOI: 10.1093/mnrasl/slw081.

Hilbert, S. et al. (2009). 'Ray-tracing through the Millennium Simulation: Born corrections and lens-lens coupling in cosmic shear and galaxy-galaxy lensing.' In: *AAP* 499, pp. 31–43. DOI: 10.1051/0004-6361/200811054. arXiv: 0809.5035.

Hilbert, S. et al. (2011). 'Cosmic shear covariance: the log-normal approximation.' In: *AAP* 536, A85, A85. DOI: 10.1051/0004-6361/201117294. arXiv: 1105.3980 [astro-ph.CO].

Hinshaw, G. et al. (2013). 'Nine-year Wilkinson Microwave Anisotropy Probe (WMAP) Observations: Cosmological Parameter Results.' In: *ApJS* 208, 19, p. 19. DOI: 10.1088/0067-0049/208/2/19. arXiv: 1212.5226 [astro-ph.CO].

Hoffman, Y. (1986). 'The dynamics of superclusters - The effect of shear.' In: *ApJ* 308, pp. 493–498. DOI: 10.1086/164520.

Horndeski, G. W. (1974). 'Second-Order Scalar-Tensor Field Equations in a Four-Dimensional Space.' In: *International Journal of Theoretical Physics* 10, pp. 363–384. DOI: 10.1007/BF01807638.

Hu, B. et al. (2014). 'Effective field theory of cosmic acceleration: An implementation in CAMB.' In: *Phys. Rev. D* 89.10, 103530, p. 103530. DOI: 10.1103/PhysRevD.89.103530. arXiv: 1312.5742.

Hu, W. (1999). 'Power Spectrum Tomography with Weak Lensing.' In: *ApJ Letters* 522, pp. L21–L24. DOI: 10.1086/312210. eprint: arXiv:astro-ph/9904153.

— (2000). 'Weak lensing of the CMB: A harmonic approach.' In: *Phys. Rev. D* 62.4, 043007, p. 043007. DOI: 10.1103/PhysRevD.62.043007. eprint: astro-ph/0001303.

— (2001). 'Mapping the Dark Matter through the Cosmic Microwave Background Damping Tail.' In: *ApJ Letters* 557, pp. L79–L83. DOI: 10.1086/323253. eprint: astro-ph/0105424.

Hu, W. and T. Okamoto (2002). 'Mass Reconstruction with Cosmic Microwave Background Polarization.' In: *ApJ* 574, pp. 566–574. DOI: 10.1086/341110. eprint: astro-ph/0111606.

Hu, W. and I. Sawicki (2007). 'Models of f(R) cosmic acceleration that evade solar system tests.' In: *Phys. Rev. D* 76.6, 064004, p. 064004. DOI: 10.1103/PhysRevD.76.064004. arXiv: 0705.1158.

Hu, Wayne and Andrey V Kravtsov (2003). 'Sample variance considerations for cluster surveys.' In: *The Astrophysical Journal* 584.2, p. 702. URL: http://iopscience.iop.org/article/10.1086/345846/meta;http://arxiv.org/pdf/astro-ph/0203169.

Jenkins, A. et al. (1997). 'The Virgo consortium: simulations of dark matter and galaxy clustering.' In: *Dark and Visible Matter in Galaxies and Cosmological Implications*. Ed. by M. Persic and P. Salucci. Vol. 117. Astronomical Society of the Pacific Conference Series, p. 348.

Jenkins, A. et al. (2001). 'The mass function of dark matter haloes.' In: *MNRAS* 321, pp. 372–384. DOI: 10.1046/j.1365-8711.2001.04029.x. eprint: arXiv:astro-ph/0005260.

Jing, Y. P. (2002). 'Intrinsic correlation of halo ellipticity and its implications for large-scale weak lensing surveys.' In: *mnras* 335, pp. L89–L93. DOI: 10.1046/j.1365-8711.2002.05899.x.

Joachimi, Benjamin et al. (2015). 'Galaxy Alignments: An Overview.' In: *Space Science Reviews* 193, pp. 1–65. ISSN: 0038-6308. DOI: 10.1007/s11214-015-0177-4. URL: http://adsabs.harvard.edu/abs/2015SSRv..193....1J (visited on 05/09/2017).

Joyce, A. et al. (2015). 'Beyond the cosmological standard model.' In: *Phys. Rep.* 568, pp. 1–98. DOI: 10.1016/j.physrep.2014.12.002. arXiv: 1407.0059.

Juszkiewicz, Roman et al. (1995). 'Weakly nonlinear Gaussian fluctuations and the edgeworth expansion.' In: *The Astrophysical Journal* 442, p. 39. DOI: 10.1086/175420.

Kaiser, N. (1998). 'Weak Lensing and Cosmology.' In: *ApJ* 498, pp. 26–+. DOI: 10.1086/305515. eprint: arXiv:astro-ph/9610120.

Kaiser, Nick et al. (2000). 'Large-scale cosmic shear measurements.' In: *arXiv preprint astro-ph/0003338*. URL: http://arxiv.org/abs/astro-ph/0003338;http://arxiv.org/pdf/astro-ph/0003338.

Kauffmann, G. and S. D. M. White (1993). 'The merging history of dark matter haloes in a hierarchical universe.' In: *MNRAS* 261. DOI: 10.1093/mnras/261.4.921. URL: http://adsabs.harvard.edu/abs/1993MNRAS.261..921K.

Kauffmann, G. et al. (1999a). 'Clustering of galaxies in a hierarchical universe - I. Methods and results at z=0.' In: *MNRAS* 303, pp. 188–206. DOI: 10.1046/j.1365-8711.1999.02202.x. eprint: astro-ph/9805283.

— (1999b). 'Clustering of galaxies in a hierarchical universe - II. Evolution to high redshift.' In: *MNRAS* 307, pp. 529–536. DOI: 10.1046/j.1365-8711.1999.02711.x. eprint: astro-ph/9809168.

Kayo, Issha et al. (2001). 'Probability Distribution Function of Cosmological Density Fluctuations from a Gaussian Initial Condition: Comparison of One-Point and Two-Point Lognormal Model Predictions withN-Body Simulations.' In: *The Astrophysical Journal* 561.1, pp. 22–34. DOI: 10.1086/323227.

Kayo, Issha et al. (2012). 'Information content of weak lensing power spectrum and bispectrum: including the non-Gaussian error covariance matrix.' In: *Monthly No-*

tices of the Royal Astronomical Society, sts340. URL: https://mnras.oxfordjournals.org/content/early/2012/11/30/mnras.sts340.full.

Khoury, J. and A. Weltman (2004a). 'Chameleon Fields: Awaiting Surprises for Tests of Gravity in Space.' In: *Physical Review Letters* 93.17, 171104, p. 171104. DOI: 10.1103/PhysRevLett.93.171104. eprint: astro-ph/0309300.

— (2004b). 'Chameleon cosmology.' In: *Phys. Rev. D* 69.4, 044026, p. 044026. DOI: 10.1103/PhysRevD.69.044026. eprint: arXiv:astro-ph/0309411.

Kiessling, A. et al. (2011). 'SUNGLASS: a new weak-lensing simulation pipeline.' In: *MNRAS* 414, pp. 2235–2245. DOI: 10.1111/j.1365-2966.2011.18540.x. arXiv: 1011.1476.

Kiessling, Alina et al. (2015). 'Galaxy alignments: Theory, modelling and simulations.' In: *Space Science Reviews* 193.1, pp. 67–136. ISSN: 0038-6308, 1572-9672. DOI: 10.1007/s11214-015-0203-6. arXiv: 1504.05546. URL: http://arxiv.org/abs/1504.05546 (visited on 05/09/2017).

Kilbinger, Martin (2003). 'Cosmological parameters from cosmic shear.' In: *arXiv preprint astro-ph/0309482*. URL: http://arxiv.org/abs/astro-ph/0309482;http://arxiv.org/pdf/astro-ph/0309482.

Kirk, Donnacha et al. (2015). 'Galaxy alignments: Observations and impact on cosmology.' In: *Space Science Reviews* 193.1, pp. 139–211. ISSN: 0038-6308, 1572-9672. DOI: 10.1007/s11214-015-0213-4. arXiv: 1504.05465. URL: http://arxiv.org/abs/1504.05465 (visited on 05/09/2017).

Kitching, T. D. et al. (2014). '3D cosmic shear: cosmology from CFHTLenS.' In: *MNRAS* 442, pp. 1326–1349. DOI: 10.1093/mnras/stu934. arXiv: 1401.6842 [astro-ph.CO].

Kitching, T. D. et al. (2015). '3D weak gravitational lensing of the CMB and galaxies.' In: *Monthly Notices of the Royal Astronomical Society* 449.2, pp. 2205–2214. DOI: 10.1093/mnras/stv193.

Kitching, T. D. et al. (2017). 'The limits of cosmic shear.' In: *MNRAS* 469, pp. 2737–2749. DOI: 10.1093/mnras/stx1039. arXiv: 1611.04954.

Klypin, A. A. et al. (2011). 'Dark Matter Halos in the Standard Cosmological Model: Results from the Bolshoi Simulation.' In: *ApJ* 740, 102, p. 102. DOI: 10.1088/0004-637X/740/2/102. arXiv: 1002.3660.

Komatsu, E. et al. (2011). 'Seven-year Wilkinson Microwave Anisotropy Probe (WMAP) Observations: Cosmological Interpretation.' In: *ApJS* 192, pp. 18–+. DOI: 10.1088/0067-0049/192/2/18. arXiv: 1001.4538 [astro-ph.CO].

Kovac, J. M. et al. (2002). 'Detection of polarization in the cosmic microwave background using DASI.' In: *Nature* 420, pp. 772–787. DOI: 10.1038/nature01269. eprint: astro-ph/0209478.

LSST Dark Energy Science Collaboration (2012). 'Large Synoptic Survey Telescope: Dark Energy Science Collaboration.' In: *ArXiv e-prints*. arXiv: 1211.0310 [astro-ph.CO].

Lacasa, F. and R. Rosenfeld (2016). 'Combining cluster number counts and galaxy clustering.' In: *JCAP* 8, 005, p. 005. DOI: 10.1088/1475-7516/2016/08/005. arXiv: 1603.00918.

Langlois, D. et al. (2017). 'Effective description of higher-order scalar-tensor theories.' In: *JCAP* 5, 033, p. 033. DOI: 10.1088/1475-7516/2017/05/033. arXiv: 1703.03797 [hep-th].

Laureijs, R. et al. (2011). 'Euclid Definition Study Report.' In: *ArXiv e-prints, 1110.3193*. arXiv: 1110.3193 [astro-ph.CO].

Lesgourgues, Julien (2011). 'The Cosmic Linear Anisotropy Solving System (CLASS) I: Overview.' In: arXiv: 1104.2932v2 [astro-ph.IM].

Lewis, A. and A. Challinor (2006). 'Weak gravitational lensing of the CMB.' In: *Phys. Rep.* 429, pp. 1–65. DOI: 10.1016/j.physrep.2006.03.002. eprint: astro-ph/0601594.

Lewis, A. et al. (2000). 'Efficient Computation of Cosmic Microwave Background Anisotropies in Closed Friedmann-Robertson-Walker Models.' In: *ApJ* 538, pp. 473–476. DOI: 10.1086/309179. eprint: arXiv:astro-ph/9911177.

Li, B. et al. (2013). 'Simulating the quartic Galileon gravity model on adaptively refined meshes.' In: *JCAP* 11, 012, p. 012. DOI: 10.1088/1475-7516/2013/11/012. arXiv: 1308.3491 [astro-ph.CO].

Limber, D. N. (1953). 'The Analysis of Counts of the Extragalactic Nebulae in Terms of a Fluctuating Density Field.' In: *ApJ* 117, pp. 134–+. DOI: 10.1086/145672.

Lin, Chieh-An and Martin Kilbinger (2014). 'A new model to predict weak lensing peak counts.' In: *Proceedings of the International Astronomical Union* 10.S306, pp. 107–109. URL: http://journals.cambridge.org/abstract_S1743921314013477.

Linder, E. V. (2003). 'Exploring the Expansion History of the Universe.' In: *Physical Review Letters* 90.9, pp. 091301–+. DOI: 10.1103/PhysRevLett.90.091301. eprint: arXiv:astro-ph/0208512.

— (2006). 'On oscillating dark energy.' In: *Astroparticle Physics* 25, pp. 167–171. DOI: 10.1016/j.astropartphys.2005.12.003. eprint: arXiv:astro-ph/0511415.

Linder, E. V. et al. (2016). 'Is the effective field theory of dark energy effective?' In: *JCAP* 5, 053, p. 053. DOI: 10.1088/1475-7516/2016/05/053. arXiv: 1512.06180.

Lombriser, L. and A. Taylor (2015). 'Classifying Linearly Shielded Modified Gravity Models in Effective Field Theory.' In: *Physical Review Letters* 114.3, 031101, p. 031101. DOI: 10.1103/PhysRevLett.114.031101. arXiv: 1405.2896.

Lovelock, D. (1974). 'The uniqueness of the Einstein-Maxwell field equations.' In: *General Relativity and Gravitation* 5, pp. 399–408. DOI: 10.1007/BF00763035.

Ma, C.-P. and E. Bertschinger (1995). 'Cosmological Perturbation Theory in the Synchronous and Conformal Newtonian Gauges.' In: *ApJ* 455, p. 7. DOI: 10.1086/176550. eprint: astro-ph/9506072.

Maartens, R. et al. (2015). 'Cosmology with the SKA – overview.' In: *ArXiv e-prints*. arXiv: 1501.04076.

Mackey, J. et al. (2002). 'Theoretical estimates of intrinsic galaxy alignment.' In: *mnras* 332, pp. 788–798. DOI: 10.1046/j.1365-8711.2002.05337.x.

Majumdar, S. (2004). 'Cosmology with cluster surveys.' In: *Pramana* 63, p. 871. DOI: 10.1007/BF02705209.

Makino, N. et al. (1992). 'Analytic approach to the perturbative expansion of nonlinear gravitational fluctuations in cosmological density and velocity fields.' In: *Phys. Rev. D* 46, pp. 585–602. DOI: 10.1103/PhysRevD.46.585. URL: http://adsabs.harvard.edu/abs/1992PhRvD..46..585M.

Maoli, R et al. (2000). 'Cosmic Shear with the VLT.' In: *arXiv preprint astro-ph/0008179*. URL: http://arxiv.org/abs/astro-ph/0008179;http://arxiv.org/pdf/astro-ph/0008179.

Martin, J. (2012). 'Everything you always wanted to know about the cosmological constant problem (but were afraid to ask).' In: *Comptes Rendus Physique* 13, pp. 566–665. DOI: 10.1016/j.crhy.2012.04.008. arXiv: 1205.3365.

Mather, J. C. et al. (1990). 'A preliminary measurement of the cosmic microwave background spectrum by the Cosmic Background Explorer (COBE) satellite.' In: *ApJ Letters* 354, pp. L37–L40. DOI: 10.1086/185717.

Maturi, M. et al. (2010). 'An analytic approach to number counts of weak-lensing peak detections.' In: *AAP* 519, A23, A23. DOI: 10.1051/0004-6361/200912866. arXiv: 0907.1849 [astro-ph.CO].

Maturi, M et al. (2011). 'Imprints of primordial non-Gaussianity on the number counts of cosmic shear peaks.' In: *Monthly Notices of the Royal Astronomical Society* 416.4, pp. 2527–2538. URL: http://mnras.oxfordjournals.org/content/416/4/2527.short.

Mellier, Yannick et al. (2000). 'Cosmic shear and clusters of galaxies.' In: *arXiv preprint astro-ph/0010008*. URL: http://arxiv.org/abs/astro-ph/0010008;http://arxiv.org/pdf/astro-ph/0010008.

Merkel, Philipp M. and Björn Malte Schäfer (2017). 'Parameter constraints from weak-lensing tomography of galaxy shapes and cosmic microwave background fluctuations.' In: *Monthly Notices of the Royal Astronomical Society* 469.3, pp. 2760–2770. DOI: 10.1093/mnras/stx1044.

Metcalf, R. B. and J. Silk (1997). 'Gravitational Magnification of the Cosmic Microwave Background.' In: *ApJ* 489, pp. 1–6. DOI: 10.1086/304756. eprint: astro-ph/9708059.

Meyer, S. et al. (2012). 'Relativistic virialization in the spherical collapse model for Einstein-de Sitter and ΛCDM cosmologies.' In: *Phys. Rev. D* 86.10, 103002, p. 103002. DOI: 10.1103/PhysRevD.86.103002. arXiv: 1206.0618 [astro-ph.CO].

Meyer, S. et al. (2015). 'Evolution of linear perturbations in Lemaítre-Tolman-Bondi void models.' In: *JCAP* 3, 053, p. 053. DOI: 10.1088/1475-7516/2015/03/053. arXiv: 1412.3012.

Mota, D. F. and C. van de Bruck (2004). 'On the spherical collapse model in dark energy cosmologies.' In: *AAP* 421, pp. 71–81. DOI: 10.1051/0004-6361:20041090. eprint: arXiv:astro-ph/0401504.

Nicolis, A. et al. (2009). 'Galileon as a local modification of gravity.' In: *Phys. Rev. D* 79.6, 064036, p. 064036. DOI: 10.1103/PhysRevD.79.064036. arXiv: 0811.2197 [hep-th].

Noonan, T. W. (1974). 'Cosmological implications of available counts in clusters of galaxies.' In: *AJ* 79, p. 775. DOI: 10.1086/111607.

Ohta, Y. et al. (2003). 'Evolution of the Cosmological Density Distribution Function from the Local Collapse Model.' In: *ApJ* 589, pp. 1–16. DOI: 10.1086/374375. eprint: arXiv:astro-ph/0301567.

— (2004). 'Cosmological Density Distribution Function from the Ellipsoidal Collapse Model in Real Space.' In: *ApJ* 608, pp. 647–662. DOI: 10.1086/420762. eprint: arXiv:astro-ph/0402618.

Okamoto, T. and W. Hu (2003). 'Cosmic microwave background lensing reconstruction on the full sky.' In: *Phys. Rev. D* 67.8, 083002, p. 083002. DOI: 10.1103/PhysRevD.67.083002. eprint: astro-ph/0301031.

Pace, F. et al. (2010). 'Spherical collapse model in dark-energy cosmologies.' In: *MNRAS* 406, pp. 1865–1874. DOI: 10.1111/j.1365-2966.2010.16841.x. arXiv: 1005.0233 [astro-ph.CO].

Pace, F. et al. (2012). 'Structure formation in cosmologies with oscillating dark energy.' In: *MNRAS* 422, pp. 1186–1202. DOI: 10.1111/j.1365-2966.2012.20692.x. arXiv: 1111.1556 [astro-ph.CO].

Pace, F. et al. (2014a). 'A comparison of structure formation in minimally and non-minimally coupled quintessence models.' In: *MNRAS* 437, pp. 547–561. DOI: 10.1093/mnras/stt1907. arXiv: 1307.7026 [astro-ph.CO].

Pace, F. et al. (2014b). 'Effects of shear and rotation on the spherical collapse model for clustering dark energy.' In: *MNRAS* 445, pp. 648–659. DOI: 10.1093/mnras/stu1782. arXiv: 1406.1448.

Pace, F. et al. (2017). 'Effects of tidal gravitational fields in clustering dark energy models.' In: *MNRAS* 466, pp. 1839–1847. DOI: 10.1093/mnras/stw3244. arXiv: 1612.03018.

Padmanabhan, T. (1996). *Cosmology and Astrophysics through Problems*.

Penzias, A. A. and R. W. Wilson (1965). 'A Measurement of Excess Antenna Temperature at 4080 Mc/s.' In: *ApJ* 142, pp. 419–421. DOI: 10.1086/148307.

Perlmutter, S. et al. (1998). 'Discovery of a supernova explosion at half the age of the universe.' In: *Nature* 391, p. 51. DOI: 10.1038/34124. eprint: astro-ph/9712212.

Perlmutter, S. et al. (1999). 'Measurements of Omega and Lambda from 42 High-Redshift Supernovae.' In: *ApJ* 517, pp. 565–586. DOI: 10.1086/307221. eprint: arXiv:astro-ph/9812133.

Petri, Andrea et al. (2016). 'Sample variance in weak lensing: How many simulations are required?' In: *Physical Review D* 93.6, p. 063524. URL: http://journals.aps.org/prd/abstract/10.1103/PhysRevD.93.063524;http://link.aps.org/pdf/10.1103/PhysRevD.93.063524.

Planck Collaboration XIII (2015). 'Planck 2015 results. XIII. Cosmological parameters.' In: *ArXiv e-prints, 1502.01589*. arXiv: 1502.01589.

Press, W. H. and P. Schechter (1974). 'Formation of Galaxies and Clusters of Galaxies by Self-Similar Gravitational Condensation.' In: *ApJ* 187, pp. 425–438. DOI: 10.1086/152650.

Raccanelli, A. et al. (2016). 'Cosmological measurements with general relativistic galaxy correlations.' In: *JCAP* 5, 009, p. 009. DOI: 10.1088/1475-7516/2016/05/009. arXiv: 1505.06179.

Redlich, M. et al. (2014). 'Probing spatial homogeneity with LTB models: a detailed discussion.' In: *AAP* 570, A63, A63. DOI: 10.1051/0004-6361/201424553. arXiv: 1408.1872.

Regős, Enikős and Alexander S Szalay (1995). 'Density and velocity correlations of peaks from random Gaussian fluctuations.' In: *Monthly Notices of the Royal Astronomical Society* 272.2, pp. 447–461. URL: http://mnras.oxfordjournals.org/content/272/2/447.short.

Reischke, R. et al. (2017). 'Variations of cosmic large-scale structure covariance matrices across parameter space.' In: *MNRAS* 465, pp. 4016–4025. DOI: 10.1093/mnras/stw2976. arXiv: 1607.03136.

Reischke, R. et al. (2018). 'MCMC forecasts of modified gravity with future CMB and LSS observations.' In: *in prep.*

Reischke, Robert et al. (2016a). 'Extreme value statistics of weak lensing shear peak counts.' In: *Monthly Notices of the Royal Astronomical Society* 456.1, pp. 641–653. URL: https://mnras.oxfordjournals.org/content/456/1/641.full.

Reischke, Robert et al. (2016b). 'Spherical collapse of dark matter haloes in tidal gravitational fields.' In: *Monthly Notices of the Royal Astronomical Society* 463.1, pp. 429–440. DOI: 10.1093/mnras/stw1989.

— (2017). 'Shear and vorticity in the spherical collapse of dark matter haloes.' In: *Monthly Notices of the Royal Astronomical Society* 473.4, pp. 4558–4565. DOI: 10.1093/mnras/stx2610.

Riess, A. G. et al. (1998). 'Observational Evidence from Supernovae for an Accelerating Universe and a Cosmological Constant.' In: *AJ* 116, pp. 1009–1038. DOI: 10.1086/300499. eprint: arXiv:astro-ph/9805201.

Rudd, Douglas H. et al. (2008). 'Effects of Baryons and Dissipation on the Matter Power Spectrum.' In: *The Astrophysical Journal* 672.1, pp. 19–32. DOI: 10.1086/523836.

Ryden, B. S. (1995). 'Cosmological Distortions in Redshift Space.' In: *American Astronomical Society Meeting Abstracts #186*. Vol. 27. Bulletin of the American Astronomical Society, p. 849.

Ryden, B. S. and J. E. Gunn (1987). 'Galaxy formation by gravitational collapse.' In: *ApJ* 318, pp. 15–31. DOI: 10.1086/165349.

Sachs, R. K. and A. M. Wolfe (1967). 'Perturbations of a Cosmological Model and Angular Variations of the Microwave Background.' In: *ApJ* 147, pp. 73–+. DOI: 10.1086/148982.

Sánchez, A. G. et al. (2009). 'Cosmological parameter constraints from SDSS luminous red galaxies: a new treatment of large-scale clustering.' In: *MNRAS* 400, pp. 1643–1664. DOI: 10.1111/j.1365-2966.2009.15572.x. arXiv: 0901.2570.

Sato, M. et al. (2011). 'Simulations of Wide-field Weak-lensing Surveys. II. Covariance Matrix of Real-space Correlation Functions.' In: *ApJ* 734, 76, p. 76. DOI: 10.1088/0004-637X/734/2/76. arXiv: 1009.2558 [astro-ph.CO].

Sato, Masanori et al. (2009). 'Simulations of wide-field weak lensing surveys. I. Basic statistics and non-gaussian effects.' In: *The Astrophysical Journal* 701.2, p. 945. URL: http://iopscience.iop.org/article/10.1088/0004-637X/701/2/945/meta;http://arxiv.org/pdf/0906.2237.

Schäfer, B. M. (2009). 'Galactic Angular Momenta and Angular Momentum Correlations in the Cosmological Large-Scale Structure.' In: *International Journal of Modern Physics D* 18, pp. 173–222. DOI: 10.1142/S0218271809014388. arXiv: 0808.0203.

Schäfer, B. M. and R. Reischke (2016). 'Describing variations of the Fisher-matrix across parameter space.' In: *MNRAS* 460, pp. 3398–3406. DOI: 10.1093/mnras/stw1221. arXiv: 1603.03626.

Schäfer, Björn Malte and Kazuya Koyama (2008). 'Spherical collapse in modified gravity with the Birkhoff theorem.' In: *Monthly Notices of the Royal Astronomical Society* 385.1, pp. 411–422. URL: https://mnras.oxfordjournals.org/content/385/1/411.full.

Schäfer, Björn Malte and Philipp M Merkel (2012). 'Galactic angular momenta and angular momentum couplings in the large-scale structure.' In: *Monthly Notices of the Royal Astronomical Society* 421.4, pp. 2751–2762. URL: http://mnras.oxfordjournals.org/content/421/4/2751.short.

Schneider, A. and R. Teyssier (2015). 'A new method to quantify the effects of baryons on the matter power spectrum.' In: *JCAP* 12, 049, p. 049. DOI: 10.1088/1475-7516/2015/12/049. arXiv: 1510.06034.

Schneider, P. et al. (1992). *Gravitational Lenses*.

Scoccimarro, Roman et al. (1999). 'Power spectrum correlations induced by nonlinear clustering.' In: *The Astrophysical Journal* 527.1, p. 1. URL: http://iopscience.iop.org/article/10.1086/308059/meta;http://arxiv.org/pdf/astro-ph/9901099.

Seager, S. et al. (2000). 'How Exactly Did the Universe Become Neutral?' In: *ApJS* 128, pp. 407–430. DOI: 10.1086/313388. eprint: astro-ph/9912182.

Seljak, U. (1996). 'Gravitational Lensing Effect on Cosmic Microwave Background Anisotropies: A Power Spectrum Approach.' In: *ApJ* 463, p. 1. DOI: 10.1086/177218. eprint: astro-ph/9505109.

Seljak, U. and M. Zaldarriaga (1996). 'A Line-of-Sight Integration Approach to Cosmic Microwave Background Anisotropies.' In: *ApJ* 469, p. 437. DOI: 10.1086/177793. eprint: astro-ph/9603033.

Sellentin, E. (2015). 'A fast, always positive definite and normalizable approximation of non-Gaussian likelihoods.' In: *MNRAS* 453, pp. 893–898. DOI: 10.1093/mnras/stv1671. arXiv: 1506.04866.

Sellentin, Elena and Alan F Heavens (2016). 'Parameter inference with estimated covariance matrices.' In: *Monthly Notices of the Royal Astronomical Society: Letters* 456.1, pp. L132–L136. URL: https://mnrasl.oxfordjournals.org/content/456/1/L132.full.

Sellentin, Elena et al. (2017a). 'On the use of the Edgeworth expansion in cosmology I: how to foresee and evade its pitfalls.' In: arXiv: 1709.03452v1 [astro-ph.CO].

Sellentin, Elena et al. (2017b). 'The skewed weak lensing likelihood: why biases arise, despite data and theory being sound.' In: eprint: 1712.04923.

Sheth, R. K. and G. Tormen (1999). 'Large-scale bias and the peak background split.' In: *MNRAS* 308, pp. 119–126. DOI: 10.1046/j.1365-8711.1999.02692.x. eprint: arXiv:astro-ph/9901122.

Sheth, R. K. et al. (2001). 'Ellipsoidal collapse and an improved model for the number and spatial distribution of dark matter haloes.' In: *MNRAS* 323, pp. 1–12. DOI: 10.1046/j.1365-8711.2001.04006.x. eprint: arXiv:astro-ph/9907024.

Silk, J. (1967). 'Fluctuations in the Primordial Fireball.' In: *Nature* 215, pp. 1155–1156. DOI: 10.1038/2151155a0.

Skordis, C. et al. (2006). 'Large Scale Structure in Bekenstein's Theory of Relativistic Modified Newtonian Dynamics.' In: *Physical Review Letters* 96.1, pp. 011301–+. DOI: 10.1103/PhysRevLett.96.011301. eprint: arXiv:astro-ph/0505519.

Smith, R. E. et al. (2003). 'Stable clustering, the halo model and non-linear cosmological power spectra.' In: *MNRAS* 341, pp. 1311–1332. DOI: 10.1046/j.1365-8711.2003.06503.x. eprint: arXiv:astro-ph/0207664.

Springel, V. (2005). 'The cosmological simulation code GADGET-2.' In: *MNRAS* 364, pp. 1105–1134. DOI: 10.1111/j.1365-2966.2005.09655.x. eprint: arXiv:astro-ph/0505010.

Spurio Mancini, A. et al. (2018). 'Testing (modified) gravity with 3D and tomographic cosmic shear.' In: eprint: 1801.04251.

Straumann, N. (1991). *General Relativity and Relativistic Astrophysics*, p. 81.

Sunyaev, R. A. and I. B. Zeldovich (1980). 'Microwave background radiation as a probe of the contemporary structure and history of the universe.' In: *ARA& A* 18, pp. 537–560. DOI: 10.1146/annurev.aa.18.090180.002541.

Tadros, H. (1993). 'Redshift space distortions in the power spectrum of CDM simulations.' In: *Cosmic Velocity Fields*. Ed. by F. Bouchet and M. Lachieze-Rey, p. 583.

Takada, M. and S. Bridle (2007). 'Probing dark energy with cluster counts and cosmic shear power spectra: including the full covariance.' In: *New Journal of Physics* 9, pp. 446–+. DOI: 10.1088/1367-2630/9/12/446. arXiv: 0705.0163.

Takada, M. and W. Hu (2013). 'Power spectrum super-sample covariance.' In: *Phys. Rev. D* 87.12, 123504, p. 123504. DOI: 10.1103/PhysRevD.87.123504. arXiv: 1302.6994 [astro-ph.CO].

Takada, M. and B. Jain (2004). 'Cosmological parameters from lensing power spectrum and bispectrum tomography.' In: *MNRAS* 348, pp. 897–915. DOI: 10.1111/j.1365-2966.2004.07410.x. eprint: arXiv:astro-ph/0310125.

— (2009). 'The impact of non-Gaussian errors on weak lensing surveys.' In: *MNRAS* 395, pp. 2065–2086. DOI: 10.1111/j.1365-2966.2009.14504.x. arXiv: 0810.4170.

Takahashi, R. et al. (2012). 'Revising the Halofit Model for the Nonlinear Matter Power Spectrum.' In: *ApJ* 761, 152, p. 152. DOI: 10.1088/0004-637X/761/2/152. arXiv: 1208.2701.

Taruya, A. et al. (2002). 'Lognormal Property of Weak-Lensing Fields.' In: *ApJ* 571, pp. 638–653. DOI: 10.1086/340048. eprint: astro-ph/0202090.

Tegmark, M. et al. (1997). 'Karhunen-Loève Eigenvalue Problems in Cosmology: How Should We Tackle Large Data Sets?' In: *ApJ* 480, pp. 22–35. DOI: 10.1086/303939. eprint: astro-ph/9603021.

Thornton, R. J. et al. (2016). 'The Atacama Cosmology Telescope: The Polarization-sensitive ACTPol Instrument.' In: *ApJS* 227, 21, p. 21. DOI: 10.3847/1538-4365/227/2/21. arXiv: 1605.06569 [astro-ph.IM].

Tolman, R. C. (1934). 'Effect of Inhomogeneity on Cosmological Models.' In: *Proceedings of the National Academy of Science* 20, pp. 169–176. DOI: 10.1073/pnas.20.3.169.

Tonry, J. L. et al. (2003). 'Cosmological Results from High-z Supernovae.' In: *ApJ* 594, pp. 1–24. DOI: 10.1086/376865. eprint: arXiv:astro-ph/0305008.

Tsujikawa, S. (2010). 'Dark energy: investigation and modeling.' In: *ArXiv e-prints, 1004.1493*. arXiv: 1004.1493 [astro-ph.CO].

Tucker, W. et al. (1998). '1E 0657-56: A Contender for the Hottest Known Cluster of Galaxies.' In: *ApJ Letters* 496, pp. L5–L8. DOI: 10.1086/311234. eprint: astro-ph/9801120. URL: http://adsabs.harvard.edu/abs/1998ApJ...496L...5T.

Tugendhat, Tim M. and Bjoern Malte Schaefer (2017). 'Angular ellipticity correlations in a composite alignment model for elliptical and spiral galaxies and inference from weak lensing.' In: eprint: 1709.02630.

Vainshtein, A. I. (1972). 'To the problem of nonvanishing gravitation mass.' In: *Physics Letters B* 39, pp. 393–394. DOI: 10.1016/0370-2693(72)90147-5.

Van Waerbeke, L. et al. (2013). 'CFHTLenS: mapping the large-scale structure with gravitational lensing.' In: *MNRAS* 433, pp. 3373–3388. DOI: 10.1093/mnras/stt971. arXiv: 1303.1806 [astro-ph.CO].

Velten, H. et al. (2017). 'Limits on the Anomalous Speed of Gravitational Waves From Binary Pulsars.' In: *International Journal of Modern Physics Conference Series*.

Vol. 45. International Journal of Modern Physics Conference Series, p. 1760016. DOI: 10.1142/S2010194517600163. arXiv: 1703.00307 [gr-qc].

Vogelsberger, M. et al. (2014). 'Introducing the Illustris Project: simulating the coevolution of dark and visible matter in the Universe.' In: *MNRAS* 444, pp. 1518–1547. DOI: 10.1093/mnras/stu1536. arXiv: 1405.2921.

Weinberg, David H. et al. (2013). 'Observational probes of cosmic acceleration.' In: *Physics Reports* 530.2, pp. 87–255. DOI: 10.1016/j.physrep.2013.05.001.

White, S. D. M. (1984). 'Angular momentum growth in protogalaxies.' In: *ApJ* 286, pp. 38–41. DOI: 10.1086/162573.

Winther, H. A. et al. (2015). 'Modified gravity N-body code comparison project.' In: *MNRAS* 454, pp. 4208–4234. DOI: 10.1093/mnras/stv2253. arXiv: 1506.06384.

Wright, E. L. et al. (1992). 'Interpretation of the cosmic microwave background radiation anisotropy detected by the COBE Differential Microwave Radiometer.' In: *ApJ Letters* 396, pp. L13–L18. DOI: 10.1086/186506.

Zaroubi, S. and Y. Hoffman (1993). 'Gravitational Collapse in an Expanding Universe: Asymptotic Self-similar Solutions.' In: *ApJ* 416, p. 410. DOI: 10.1086/173246.

Zel'Dovich, Y. B. (1970). 'Gravitational instability: An approximate theory for large density perturbations.' In: *AAP* 5, pp. 84–89. URL: http://adsabs.harvard.edu/abs/1970A%26A.....5...84Z.

Zhao, G.-B. et al. (2011). 'N-body simulations for f(R) gravity using a self-adaptive particle-mesh code.' In: *Phys. Rev. D* 83.4, 044007, p. 044007. DOI: 10.1103/PhysRevD.83.044007. arXiv: 1011.1257 [astro-ph.CO].

Zumalacarregui, Miguel et al. (2016). 'hiclass: Horndeski in the Cosmic Linear Anisotropy Solving System.' In: *ArXiv e-prints*. eprint: 1605.06102.

de Felice, A. et al. (2011). 'Effective gravitational couplings for cosmological perturbations in the most general scalar-tensor theories with second-order field equations.' In: *Physics Letters B* 706, pp. 123–133. DOI: 10.1016/j.physletb.2011.11.028. arXiv: 1108.4242 [gr-qc].

ACKNOWLEDGEMENTS

Finally, it is a pleasure to thank several people who made contributions to this thesis in many different ways.

First and foremost, I would like to thank my advisor Björn Malte Schäfer for his endless enthusiasm, support as well as discussing physics, piano play and basically everything else. Björn is an excellent teacher and and great scientist. His excitement when it comes to physics is marvelous.

I would like to thank Matthias Bartelmann and Matteo Maturi, you make the cosmology groups at ITA to a very special place in so many different ways.

My gratitude also belongs to Alan Heavens for to great months in London and for the hospitality at the ICIC.

I would also like to thank Luca Amendola for being the second referee for this thesis. Francesco Pace and Sven Meyer deserve a big thanks for an inspiring and fun collaboration. Furthermore I would like to thank Alessio Spurio Mancini whom I worked with a lot over the year.

A very special thanks belongs to my long-time office mates in the ITA-KITA, Robert Lilow and Felix Fabis, for insightful discussions about physics and programming as well as for just fooling around. Of course also Elena Kozlikin belongs in this list, even though she decided to move to a warmer office.

The whole ITA cosmology group: Johannes Schwinn, Mauricio Carrasco, Iva Karovicova, Céline Tchernin, Sara Konrad, Jonas Frings, Shahede Ghafourizade (and Celia Viermann, I hope you are happy now!) deserves a big thanks for creating such a lovely academical environment. In this context I would especially like to thank Christian Angrick who kept the coffee running and explained to me how the warp drive worked really nicely, Carsten Littek for his great displaces of Ruhrpottian culture and Tim Tugendhat for his fantastic jokes and the drinks at the Christmas parties.

The dedicated work of Anna Zacheus made sure that administrative matters never poses an obstacle to the science at ITA, thank you for this.

Now, I would like to thank my and Isabel's family. Especially my parents for always supporting me in so many ways and allowing me to go my own way.

Lastly my gratitude belongs to my girlfriend Isabel who always cheered me up during my studies, listened to my monologues over physics or programming when something did not work. Thank you for the last three years and the ones still to come.

DECLARATION OF AUTHORSHIP

The thesis I have submitted entitled "Cosmology as a probe of gravity with future surveys" is my own work. I have only used the sources indicated and have not made unauthorised use of services of a third party. Where the work of others has been quoted or reproduced, the source is always given.

Heidelberg, ...